

ABSTRACT

Title of dissertation: Measurements of Coronal Rotation
and Small Coronal Ejections
Using the STEREO COR1 Coronagraphs

Shaela I. Jones, Doctor of Philosophy, 2011

Dissertation directed by: Dr. Joseph M. Davila
Professor Douglas C. Hamilton
Department of Physics

I present results of two studies conducted using the STEREO COR1 coronagraph: single- and dual-spacecraft measurements of white-light coronal rotation rates in 2007 and 2008 as a function of latitude and altitude, and trajectory characteristics of small, upward-moving coronal density enhancements.

Single-spacecraft coronal rotation measurements indicate that the rotation rate of the corona in the COR1 field of view is independent of latitude and altitude, consistent with previous studies that showed rotation in the corona is very rigid compared with rotation in the photosphere. The equatorial rotation rate for this study was found to be 27.06 ± 0.08 days in 2007 and 26.97 ± 0.10 days in 2008. Using the measured rotation periods, I extract the average coronal intensity as a function of longitude at each latitude at 1.8 solar radii, and compare them to reconstructions of the coronal electron density by Kramar et al. [46]. The longitudinal structure derived from the rotation measurements is very similar to the electron density measurements, indicating that the observed rigidity of the coronal rotation

does not seem to be due to projection of low-latitude features onto higher latitudes as some authors have speculated.

It has been suggested that the relative rigidity of the coronal rotation may be at least in part a measurement effect, due to the selective measurement of large and/or long-lived features in coronagraph rotation studies. Following the measurements of coronal rotation in the STEREO COR1 field of view using standard coronagraph rotation measurement techniques, I present for the first time short time lag coronagraph rotation measurements, using the unique capabilities of the STEREO dual-spacecraft mission.

Finally, I present results of a systematic search of nineteen days' worth of COR1 data for small, faint, outward-moving density enhancements, sometimes referred to in the literature as plasma blobs. In the past these plasma blobs have been studied in the Large Angle Spectroscopic Coronagraph (LASCO) C2 and C3 fields of view, which extend only as low as $2 - 2.5R_{\odot}$, and it was believed that their origin was in pointed cusps at the top of the streamer belt. Using the COR1 coronagraph I was able to observe many such features between $1.5 - 2.0R_{\odot}$, a height below what would normally be expected if these features originate at the top of the streamer belt as suggested by the earlier observations.

Measurements of Coronal Rotation and Small Coronal
Ejections Using the STEREO COR1 Coronagraph

by

Shaela I. Jones

Dissertation submitted to the Faculty of the Graduate School of the
University of Maryland, College Park in partial fulfillment
of the requirements for the degree of
Doctor of Philosophy
2011

Advisory Committee:

Dr. Joseph Davila, Co-Chair/Advisor

Professor Douglas Hamilton, Co-Chair/Advisor

Dr. O. Chris St. Cyr

Professor Daniel Lathrop

Professor Eun-Suk Seo

Professor Michael Coplan

© Copyright by
Shaela I. Jones
2011

To Nick and Roman

Acknowledgments

Many thanks are owed to many people for helping to make this document possible. First, I must thank all the great people from Code 670 at NASA Goddard Space Flight Center, for their support and collegiality during my studies there. In particular, Joe Davila, Chris St. Cyr, and Bill Thompson have been great sources of information and many helpful suggestions throughout my time at Goddard. Second, thank you to the many wonderful friends I have met while studying at the University of Maryland; Renee Michelle and Andy, Tracy and Tommy, Matty and Jonathan, Rolando and Beatriz, Ellie and Kevin, Matt and Namrata, Brad, Ray, and others: thanks to all of you for being such great companions and study partners. Third, thank you to all the excellent teachers who have believed in and encouraged me over the years - without whom I would not be here - especially Mr. Wiendenheft, Mr. Baker, and Mr. Sawyer.

I would also like to acknowledge those individuals who were kind enough to allow me to include some of their own work in this thesis: especially Maxim Kramar and Bill Thompson. Thanks as well to Guillermo Stenborg, who provided timely suggestions and references during my coronal rotation study, and whose work greatly influenced mine. I also owe a debt of gratitude to the anonymous referee of my paper regarding the material of chapter 5, whose comments on the paper were courteous, thorough, and insightful. Additional thanks are due to Joe Davila, Chris St. Cyr, Nicholas Mecholsky, and Maxim Kramar for their help editing this thesis. Acknowledgements are also due to Nicholas Chant and Steve Ritz for their support

of my assistantship at Goddard.

Finally, I owe an extreme debt of gratitude to my family: my parents John and Karen, my sisters Melissa and Michelle, my husband Nicholas, and my son Roman. You mean more to me than I can say.

Contents

| | |
|---|-----|
| List of Figures | vii |
| List of Abbreviations | xv |
| 1 Introduction to Solar Physics | 1 |
| 1.1 Introduction | 1 |
| 1.2 The Solar Interior | 1 |
| 1.3 The Solar Atmosphere | 3 |
| 1.4 The Coronal Magnetic Field | 4 |
| 1.4.1 Magnetic Structures in the Corona | 5 |
| 1.4.2 Magnetic Reconnection | 6 |
| 1.4.3 The Solar Cycle | 10 |
| 1.5 Mass Loss from the Corona | 12 |
| 1.5.1 Solar Wind | 12 |
| 1.5.2 Coronal Mass Ejections | 13 |
| 1.5.3 Everything in Between | 14 |
| 1.6 Impact of Solar Processes on Humanity | 15 |
| 1.7 Summary | 15 |
| 1.8 Outline of the Thesis | 16 |
| 2 The STEREO Mission and the COR1 Coronagraph | 17 |
| 2.1 Introduction | 17 |
| 2.2 Observing the Corona | 17 |
| 2.2.1 Coronal Emission | 19 |
| 2.2.2 Scattering of Photospheric Light by Coronal Electrons | 19 |
| 2.3 The STEREO Mission Concept | 23 |
| 2.4 The COR1 Coronagraph | 25 |
| 2.4.1 Instrument Design | 25 |
| 2.4.2 COR1 Data Processing | 28 |
| 2.5 Summary | 31 |
| 3 COR1 Coronal Rotation Rate Measurements | 32 |
| 3.1 Introduction | 32 |
| 3.1.1 Rotation of the Solar Photosphere | 32 |
| 3.1.2 Rotation in the Corona | 35 |
| 3.2 Data Preparation | 39 |
| 3.3 Period Measurement Methods | 40 |
| 3.3.1 Autocorrelation | 42 |
| 3.3.2 Phase Dispersion Minimization | 43 |
| 3.4 Evaluating Spectral Significance | 44 |
| 3.5 Period Search Results and Discussion | 46 |
| 3.6 Projection Effects and Secondary Periods | 58 |
| 3.7 Conclusions | 62 |

| | | |
|-------|---|-----|
| 4 | Rotation Rates from Multi-Spacecraft Observations | 64 |
| 4.1 | Introduction: Opportunities from Multi-Spacecraft Observations . . . | 64 |
| 4.2 | Data | 67 |
| 4.3 | Dual-Spacecraft Method | 69 |
| 4.4 | Simulated Results | 71 |
| 4.5 | Results | 74 |
| 4.6 | Feature Scale-Size Analysis | 77 |
| 4.6.1 | Boxcar Smoothing | 80 |
| 4.6.2 | Convolution | 81 |
| 4.6.3 | Wavelet Filtering | 86 |
| 4.6.4 | Discussion of Scale-Size Analyses | 92 |
| 4.7 | Discussion | 94 |
| 4.8 | Conclusions | 99 |
| 5 | Localized Plasma Density Enhancements Observed in STEREO COR1 | 101 |
| 5.1 | Introduction | 101 |
| 5.2 | Method | 104 |
| 5.3 | Results | 110 |
| 5.4 | Discussion and Conclusions | 116 |
| 6 | Conclusions and Future Work | 120 |
| 6.1 | Summary of Questions Addressed | 120 |
| 6.2 | Summary of Rotation Results | 122 |
| 6.3 | Summary of Plasma Density Enhancement Results | 126 |
| 6.4 | Future Work | 127 |
| A | An Overview of Solar Rotational Tomography | 130 |
| A.1 | Electron Density from Coronagraph Images | 130 |
| A.2 | Solution By Functional Minimization | 132 |
| B | Cross-Correlation of STEREO Ahead and Behind Time Series | 136 |
| C | Contamination of Cross-Correlation Periodogram by Simultaneous Events | 139 |

List of Figures

| | | |
|-----|--|----|
| 1.1 | Left: A cutaway view of the solar interior, showing the four inner layers. Right: A Hinode Solar Optical Telescope (SOT) close-up view of the solar surface, showing solar granulation. Images courtesy of NASA. | 2 |
| 1.2 | Electron temperature and density as a function of height above the photosphere. Values below 2500km are taken from [97], while values above are taken from [25]. | 5 |
| 1.3 | Some images highlighting coronal features: Transition Region and Coronal Explorer (TRACE) image of an active region (top left), Extreme Ultraviolet Imaging Telescope (EIT) image of a prominence (top right), X-Ray Telescope (XRT) image of a coronal hole with a plume (bottom left) and a LASCO C2 coronagraph image of the streamer belt (bottom right). Images courtesy of NASA. | 7 |
| 1.4 | A simple 2-dimensional magnetic reconnection model. Plasma flow forces magnetic fields of opposite polarity together. Where the two fields come together the magnetic topology is abruptly altered, leading to the conversion of magnetic energy into kinetic and thermal energy. | 8 |
| 1.5 | A TRACE spectroscopic image of the solar corona at 171 Å (an Fe IX emission line), showing an apparent magnetic null point in the corona. This wavelength channel highlights material at approximately one million kelvin. | 9 |
| 1.6 | A magnetogram showing the emergence of the first mid-latitude sunspot of solar cycle 24. A large, older sunspot from solar cycle 23 is seen in the equatorial region. Image courtesy of NOAA. | 11 |
| 1.7 | A composite of 284 Å spectroscopic images of the corona, produced by the EIT instrument on the Solar and Heliospheric Observatory (SOHO) spacecraft. The bright material in this image is approximately two million kelvin. Image courtesy of SOHO (ESA & NASA). | 12 |
| 1.8 | A Coronal Mass Ejection (CME) seen in several SOHO instruments. The left (spectroscopic) image shows the CME in 195 Å (about one million kelvin), the middle shows it some time later in the C2 white-light coronagraph (the white circle represents the edge of the solar disk) and the right shows it even later in the C3 coronagraph. Image courtesy of SOHO (ESA & NASA). | 14 |
| 1.9 | An artist's rendition of a CME headed toward Earth. Image courtesy of NASA/Steele Hill. | 16 |

| | | |
|-----|--|----|
| 2.1 | Plot showing the brightness of the three components of the corona, relative to the brightness of the solar disk. The intensity of the K-corona varies slightly with phase of the solar cycle; it is shown at solar maximum. Dashed lines indicate the brightness of the sky for several observing conditions on Earth. Figure courtesy of S. St. Cyr, private communication. | 18 |
| 2.2 | Diagram illustrating the geometry of Thomson scattering. Light traveling from the source towards the scattering volume can be divided into two polarization components, one in and one out of the plane of the paper. The component in the plane of the paper, when scattered, is reduced according to the cosine of the angle χ | 20 |
| 2.3 | Diagram showing scattering of photospheric light from a point S in the photosphere by electrons at a point P in the corona. The point O is the nearest point on the solar surface to the point P. (Reproduced with permission [10].) | 21 |
| 2.4 | The positions of the two Solar TERrestrial RELations Observatory (STEREO) spacecraft with respect to the Earth and the Sun on August first of 2007 (a) and 2008 (b). ‘A’ indicates the position of the Ahead spacecraft, while ‘B’ indicates the Behind spacecraft. | 24 |
| 2.5 | A schematic showing the optical layout of the COR1 coronagraph. (Reproduced with permission [92].) | 27 |
| 2.6 | Top: An unprocessed STEREO COR1-B image. Bottom: a processed STEREO COR1-B pB image. The arrows indicate a small CME in progress. The white circles drawn over the occulter in both images indicate the approximate location of the solar limb. | 29 |
| 3.1 | The distribution of polar superpixels over a COR1 Ahead image from 2008. | 41 |
| 3.2 | Top: Polarized brightness signal observed in 2008 from COR1-B at $1.8R_{\odot}$ and 1.5° S plane of the sky (POS) latitude. Bottom: The autocorrelation and phase dispersion minimization (PDM) results obtained from the data series in the top panel. The PDM result has been subtracted from one so that for both methods likely periods are indicated by peaks. A perfectly periodic time series would produce an autocorrelation/PDM value of 1.0 at the appropriate period. . . . | 44 |
| 3.3 | Coronal rotation measurements from 2007 at altitudes 1.8 and $2.2R_{\odot}$. The image intensity shows the PDM result as a function of latitude and rotation period. The contours show the intensity of the corresponding autocorrelation curves. The dashed line shows the photospheric rotation period as a function of latitude given by [47]. The asterisks show the positions of the autocorrelation maxima, averaged between spacecraft and limbs. | 48 |

| | | |
|------|--|----|
| 3.4 | Coronal rotation measurements from 2007 at altitudes 2.8 and $3.2R_{\odot}$. The image intensity shows the PDM result as a function of latitude and rotation period. The contours show the intensity of the corresponding autocorrelation curves. The dashed line shows the photospheric rotation period as a function of latitude given by [47]. The asterisks show the positions of the autocorrelation maxima, averaged between spacecraft and limbs. | 49 |
| 3.5 | Coronal rotation measurements from 2008 at altitudes 1.8 and $2.2R_{\odot}$. The image intensity shows the PDM result as a function of latitude and rotation period. The contours show the intensity of the corresponding autocorrelation curves. The dashed line shows the photospheric rotation period as a function of latitude given by [47]. The asterisks show the positions of the autocorrelation maxima, averaged between spacecraft and limbs. | 50 |
| 3.6 | Coronal rotation measurements from 2008 at altitudes 2.8 and $3.2R_{\odot}$. The image intensity shows the PDM result as a function of latitude and rotation period. The contours show the intensity of the corresponding autocorrelation curves. The dashed line shows the photospheric rotation period as a function of latitude given by [47]. The asterisks show the positions of the autocorrelation maxima, averaged between spacecraft and limbs. | 51 |
| 3.7 | Results of fitting autocorrelation peaks to equation 3.1. Asterisks denote synodic rotation periods measured in the northern hemisphere while triangles denote measurements from the southern hemisphere. The red lines show the results of the fits to the individual hemisphere data, while the orange lines show the results of fitting data from both hemispheres simultaneously. | 53 |
| 3.8 | Detailed PDM spectra for several southern latitudes at $1.8R_{\odot}$ in 2008. The black curve shows the Ahead spacecraft results and the orange curve shows the Behind. | 55 |
| 3.9 | Detailed PDM spectra for several southern latitudes at $1.8R_{\odot}$ in 2007. The black curve shows the Ahead spacecraft results and the orange curve shows the Behind. | 56 |
| 3.10 | Autocorrelation results for several southern latitudes at $1.8R_{\odot}$ in 2007 and 2008. The black curve shows the Ahead spacecraft results and the orange curve shows the Behind. | 57 |
| 3.11 | An example showing how the main periodic component is removed from a time series. The top panel shows the original data series, divided into segments containing one rotation each. These segments are then plotted on top of one another in panel two. The orange curve in panel two shows the average rotating signal, $C_{main}(\Delta)$. This curve has been interpolated at the value δ_i for each point in the original time series in panel three. Panel four shows the difference between the original time series and the interpolated values of C_{main} | 60 |

| | | |
|------|--|----|
| 3.12 | The coronal signal derived from calculating the main periodic component from every time series at $1.8R_{\odot}$ in 2008. Image brightness corresponds to the intensity of the pB signal scattered from the corresponding latitude and longitude in the corona towards the behind spacecraft. This quantity is expected to be approximately proportional to the coronal electron density shown in figure 3.6. | 61 |
| 3.13 | The average 2008 coronal electron density at $1.8R_{\odot}$ as estimated using solar rotational tomography (SRT). | 62 |
| 4.1 | The angular separation between the Ahead and Behind spacecraft during the time period studied. The solid line shows the longitudinal separation, while the dashed line shows the total angular separation. The max transit time is the time required for a corona rotating once every 27 days to traverse the angular separation of the satellites at the end of the time series. | 68 |
| 4.2 | Intensity time series from $1.8 R_{sun}$, 1.5 S POS latitude. | 69 |
| 4.3 | The top panel shows an artificial Ahead/Behind time series pair. The bottom panel shows the cross-correlation functions for these two artificial time series. The two cross-correlation curves that peak near 1.0 result from the two dual-spacecraft analyses, while the narrower peaks below result from the single-spacecraft autocorrelation analysis used in the previous chapter. | 72 |
| 4.4 | Top: An artificial Ahead/Behind time series pair. Bottom: The average correlation functions for a set of 20 time series pair like those in the top panel. The correlations near 1 result from the dual-spacecraft method, while the correlation peaks near 0.8 are found from the individual spacecraft methods used in the previous chapter. See text for details on the creation of the artificial time series pair in the top panel. | 75 |
| 4.5 | The dual-spacecraft results for several time series in the southeastern quadrant. The black (red) curves are determined with the first (second) method described in appendix B. The peaks of the individual curves are marked with asterisks. The time series for the 55.5 S and 49.5 S latitude bands showed streamer belt material sporadically over the course of the time series, which likely degraded the cross-correlation results. The results for all latitude bands peak at unexpectedly low values. | 76 |
| 4.6 | Top: A portion of the two time series from a superpixel at $1.8 R_{sun}$ and 1.5 S POS latitude, showing several impulsive events that happen nearly simultaneously in the two spacecraft despite the 14.5° longitudinal separation during the time period shown. The second spike, indicated by the arrow, occurs at 06:35, just after the passage of the CME front shown in the bottom panel. | 78 |

| | | |
|------|--|----|
| 4.7 | Results of pre-processing the cross-correlated time series by smoothing with a boxcar average. The top panel shows the cross-correlation functions for smoothing windows between 8 hours (most sharply peaked curve) and about 16 days (bottom curve). The cross-correlation maximum evolves towards longer periods as the width of the smoothing window is increased. The curve highlighted in red achieves the greatest maximum cross-correlation value, and is referred to in the text as the optimal curve. The bottom panel shows the smoothed time series corresponding to this cross-correlation curve. | 82 |
| 4.8 | Cross-correlation results after pre-processing the input time series by subtracting a smoothed time series. The top panel shows the cross-correlation curves for smoothing windows between about 8 hours (bottom curve) and about 8.5 days (top curve). For reference, a representative curve has been highlighted in red and the pre-processed intensity time series corresponding to this red curve are shown in the bottom panel. | 83 |
| 4.9 | Results of pre-processing the cross-correlated time series by convolution with the kernel K described in the text for a range of m values. The top panel shows the cross-correlation curves for m values between about 1.5 days (bottom curve) and about 6.6 days (flattest curve). The optimal cross-correlation curve is again highlighted in red. The pre-processed time series corresponding to this curve are shown in the bottom panel. | 85 |
| 4.10 | Results of pre-processing the cross-correlated time series by convolution with the kernel K for a range of m values between about 19 minutes and 47 minutes. The pre-processed time series corresponding to the red highlighted curve are shown in the bottom panel for reference. | 87 |
| 4.11 | The “Mexican hat” mother wavelet. | 88 |
| 4.12 | Cross-correlation of Ahead and Behind time series after reconstruction from the largest wavelet components. The minimum wavelet scale included in the reconstruction increases from about 2.4 hours for the bottom curve to about 3.4 days for the flattest curve. The cross-correlation curve with the highest maximum is again highlighted in red and referred to as the optimal curve. The bottom panel shows the pre-processed time series corresponding to this optimal cross-correlation curve. | 89 |

| | | |
|------|--|----|
| 4.13 | Cross-correlation of Ahead and Behind time series reconstructed from their smallest wavelet components. Here the minimum wavelet scale is set at about 41 minutes by the resolution of the time series, and the maximum wavelet scale included in the reconstruction is progressively decreased from about 20 hours to just the minimum scale to isolate progressively smaller-scale features in the time series. The top panel shows the cross-correlation curves, where the red curve at the bottom includes just the minimum wavelet scale and as the size of the maximum wavelet scale is increased the curve flattens and rises. The bottom panel shows the pre-processed time series corresponding to the red curve. | 90 |
| 4.14 | Cross-correlation of the wavelet-processed time series from the bottom panel of figure 4.12 (black) and the cross-correlation functions measured after scrambling the Ahead time series into random order (red). | 91 |
| 4.15 | Top: A comparison of the “optimal” large-scale results of the three scale separation techniques for time series at $1.8R_{\odot}$ and $1.5 S$ POS latitude. Bottom: A comparison of the cross-correlation functions for the same time series pre-processed at the smallest wavelet scale, smallest smoothing scale, and at the reference kernel size from figure 4.10. | 93 |
| 4.16 | Cross-correlation of time series pairs from several latitudes in the southeastern quadrant after pre-processing using the optimal smoothing (diamonds), convolution(asterisks), and wavelet scales (triangles) as explained in the text. | 94 |
| 4.17 | The results of cross-correlating time series pairs from several latitudes in the southeastern quadrant after pre-processing using the smallest wavelet and roughening scales and the reference convolution scale as described in the text. | 95 |
| 4.18 | The rotation periods measured from complex artificial time series pairs generated by introducing random changes to the longitudinal structure and interpolating over 500 points. For each percentage value 100 realizations of the artificial time series were created. Asterisks and triangles represent the mean of the 100 period measurements, using cross-correlation calculation methods 1 and 2, respectively, as described in appendix B. Squares and X’s show the location of the peaks when the 100 cross-correlation curves are averaged. The measured rotation period using all methods varies systematically with the percentage of the longitudinal points that are changed. | 97 |
| 4.19 | Cross-correlation of several four-month data sets from 2007 and 2008, showing a decrease in correlation bias as the STEREO mission progressed. The first data set is the one analyzed above, during which the longitudinal separation angle of the spacecraft increased from 1° to 16° . During the second data set the separation angle went from 38° to 46° , and during the third it increased from 58° to 81° | 98 |

| | | |
|-----|--|-----|
| 5.1 | A plasma blob seen in COR1-B running difference images. Arrows in the bottom three frames point to the approximate location of a Y-shaped tail at the back end of the feature. The front of the feature seems to be much fainter and is obscured during its emergence from beneath the occulter by an apparent twisting motion. | 106 |
| 5.2 | Blobs seen in COR1-B height-time images at 345° and 172.5° . These images were enhanced using the Radon transform. | 107 |
| 5.3 | A blob seen in COR2 and its counterpart in COR1. The top image shows the feature in a COR2 image sequence (with some of the lower corona occluded). Bottom left shows a Radon-enhanced COR1 height-time image at 345° , and the bottom right a combined sequence of height measurements from both instruments. COR1 error bars represent an uncertainty of ± 6 radial pixels ($\sim 0.1 R_\odot$). COR2 error bars were estimated by repeated measurement. Both are comparable to or smaller than the symbol size. All images are from the Behind spacecraft. | 109 |
| 5.4 | Distribution of event speeds from linear height-time fits. | 111 |
| 5.5 | Top: Distribution of acceleration from parabolic fits with acceleration greater than the fit error. Bottom: Value of r_1 from equation 5.1 from events with positive acceleration greater than the fit error. | 112 |
| 5.6 | Latitudinal distribution of events. | 113 |
| 5.7 | Average POS speed as a function of height for COR1 events with positive acceleration greater than the fit error, with error bars based on the standard deviation of events at that height. The solid black line shows a fit to equation 5.1 and the dashed black line shows a fit to equation 5.2. The red lines show fits to the same equations from Sheeley <i>et al.</i> [74]. | 115 |
| 6.1 | Comparison of coronal rotation measurements using COR1 coronagraphs in 2007 and 2008 with seminal studies of coronal and photospheric rotation. COR1 measurements from 2007 are shown as a solid line with asterisks, while the 2008 measurements are shown as a dashed line with triangles. The error bars shown represent the standard deviation of measurements from east and west limbs in the northern and southern hemispheres. The dash-dot line shows rotation rates from Doppler velocity measurements of photospheric plasma [34] and the dash-dot-dot line shows rates from cross-correlation of magnetograms [77]. The large X's (squares) show the results of northern hemisphere, FeXIV coronal measurements in 1985 (1977) [75]. The large triangles show ground based white-light coronal rotation measurements from Fisher and Sime [20]. | 124 |
| A.1 | Illustration showing the coronal white-light scattering geometry. | 131 |

| | | |
|-----|--|-----|
| A.2 | A two-dimensional analog of SRT. Three one-dimensional pixel arrays view a two dimensional sun and corona from different perspectives. The combined information from the three images can be used to estimate the electron density within the area of overlap. | 133 |
| B.1 | The difference between $\bar{\tau}_n$ and the nominal period values T_n (see text). The first and last points fall outside plot range, but are between -0.003 and 0.003 , less than 0.043% error. | 138 |

List of Abbreviations

| | |
|--------|---|
| AIA | Atmospheric Imaging Assembly |
| CCD | charge-coupled device |
| CME | coronal mass ejection |
| DOG | derivative of Gaussian |
| EIT | Extreme Ultraviolet Imaging Telescope |
| EUVI | Extreme Ultraviolet Imager |
| FOV | field of view |
| GPS | global positioning system |
| HCI | Heliocentric Intertial |
| IDL | Interactive Data Language |
| IHG | Inertial Heliographic |
| LASCO | Large Angle Spectroscopic Coronagraph |
| LOS | line of sight |
| pB | polarized brightness |
| PDM | phase dispersion minimization |
| POS | plane of the sky |
| SDO | Solar Dynamics Observatory |
| SOHO | Solar and Heliospheric Observatory |
| SOT | Solar Optical Telescope |
| SRT | solar rotational tomography |
| STEREO | Solar and TERrestrial RELations Observatory |
| TRACE | Transition Region and Coronal Explorer |
| UV | ultraviolet |
| XRT | X-Ray Telescope |

Chapter 1

Introduction to Solar Physics

1.1 Introduction

In this chapter I familiarize the reader with those basic aspects of solar physics that will be helpful in understanding the rest of the work, including brief descriptions of the solar interior and atmosphere, and some terminology used to describe solar coronal features. I also describe some of the important physical processes that are studied in the corona and their importance to humanity.

1.2 The Solar Interior

A thorough discussion of the inner workings of our Sun is beyond the scope of this thesis, which is focused on activity in the solar atmosphere; however, some familiarity with the generally accepted structure of the solar interior will be helpful for the discussion to follow. Figure 1.1(a) shows a cutaway model of the solar interior.

There are four distinct regions in the solar interior [39]. The region inside about one quarter solar radius ($0.25R_{\odot}$) is referred to as the core, and is the region where nuclear fusion of protons to form helium nuclei takes place. Outside the core is a region called the radiative zone, characterized by radiative transfer of heat

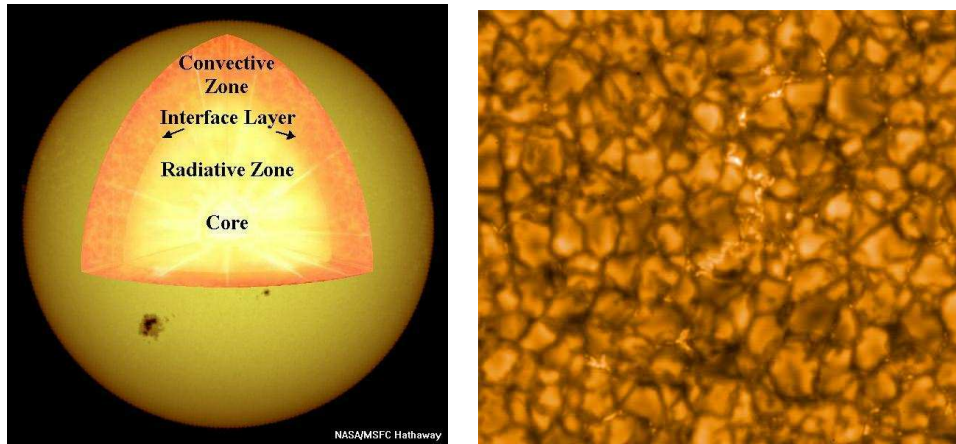


Figure 1.1: Left: A cutaway view of the solar interior, showing the four inner layers. Right: A Hinode SOT close-up view of the solar surface, showing solar granulation. Images courtesy of NASA.

generated in the solar core out to about $0.7R_{\odot}$. The core and radiative zone are believed to rotate nearly rigidly. Outside the radiative zone is a thin layer called the interface layer, or tachocline, where complex fluid motions begin to appear. The tachocline is important in solar physics because it is believed by many researchers to be the location of the solar dynamo [39]. At the top edge of the tachocline the local temperature and density have decreased enough that radiative transfer slows and the solar material begins to rapidly convect; this layer of the Sun is called the convection zone.

At the very top of the convection zone is a thin layer (about 400km deep) called the photosphere. The photosphere is the visible surface of the Sun; it is where the photons are produced that subsequently leave the Sun and travel into the solar system rather than being reabsorbed. When examined closely ($\sim 1Mm$) the photosphere appears to be covered by a web of dark cracks (see figure 1.1(b)). This effect is referred to as solar granulation and is caused by convection of the solar

material, which is bright where it rises up from the solar interior and dark where cooler material is sinking back down. The dark spots in the left panel of figure 1.1(a) are examples of another, much larger photospheric feature – a sunspot. Sunspots are regions of intense magnetic concentration, which inhibits convection in the solar material below them. This causes the photospheric material in a sunspot to be cooler than the surrounding material and thus, darker. Sunspots usually appear in groups and typically have lifetimes on the order of days to weeks, though some may persist for several months.

1.3 The Solar Atmosphere

Above the photosphere is the extremely complex solar atmosphere. Scientists refer to three layers in the solar atmosphere: the chromosphere, the transition region, and the corona. Generally, however, these layers are not gravitationally stratified because in most of the solar atmosphere the magnetic pressure dominates over the gas pressure.

The relative dominance of the thermal to magnetic pressure is described by the plasma- β parameter, $\beta = \frac{8\pi p}{B^2}$. A plasma- β less than one means the magnetic field is dominant and plasma flows primarily parallel to the magnetic field lines. (Another way of looking at this is that the plasma particles are tied to individual magnetic field lines.) This is known as the frozen-in condition. The plasma- β is less than one throughout most of the corona, which prevents material from settling into gravitationally stratified layers. The solar atmosphere is highly dynamic and inhomogeneous, with local regions of chromospheric and transition region material

scattered in the lower atmosphere and long loops of thermally isolated magnetic flux tubes in the corona, the upper atmosphere.

Coronal and chromospheric plasmas are not gravitationally stratified; however, the distinction between them is marked. Typical electron temperatures in the chromosphere are around $5 - 6 \times 10^3 K$, while in the corona they are of order $10^6 K$, which makes the emission spectrum of the corona very distinctive. Densities are much higher in the chromosphere than in the corona, and while the coronal plasma is fully ionized, the chromospheric plasma is not [5]. Figure 1.2 shows the electron temperature and density as a function of height about the photosphere. The mechanism by which the corona is heated to a temperature so much higher than that of the photosphere and chromosphere is one of the outstanding problems in solar physics. Plasma that is somewhere between coronal and chromospheric conditions is referred to as the transition region.

1.4 The Coronal Magnetic Field

The topics studied in this thesis are primarily related to the solar corona. The magnetic field in the corona is highly complex and dynamic. It is also very difficult to measure. Spectroscopic observations allow us to measure the line-of-sight (LOS) magnetic field strength at the photosphere, but the faintness of coronal emission lines (discussed in section 2.2) often makes this too difficult to do for coronal plasma. Here the frozen-in condition is helpful because it allows us to make inferences about the configuration of the local magnetic field from observations of plasma emission; emission tends to trace out the local magnetic field. In the following section I discuss

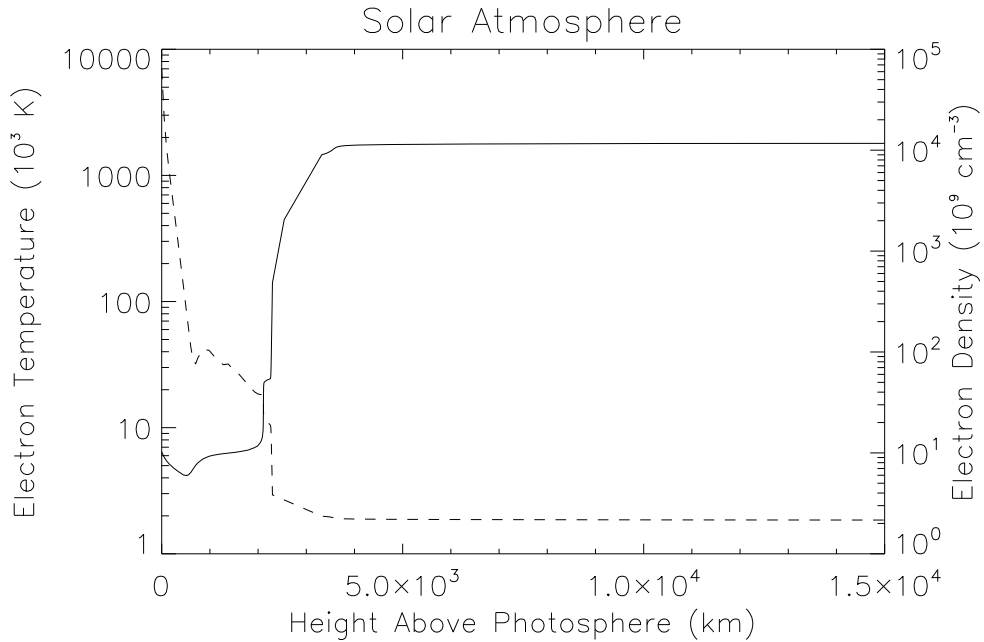


Figure 1.2: Electron temperature and density as a function of height above the photosphere. Values below 2500km are taken from [97], while values above are taken from [25].

some of the coronal structures commonly seen in emission intensity measurements.

1.4.1 Magnetic Structures in the Corona

Solar physicists recognize a number of features commonly seen in the corona (see figure 1.3 for some images of the features described here, and section 2.2 for a description of the various methods by which they are observed.) Observations of the solar corona reveal a multitude of bright arches stretching over the photosphere, referred to as coronal loops. These loops are often gathered together in complicated systems of interconnected loops called active regions. Stretching over the active regions are even larger rounded structures called streamers. Streamers have tops that appear to be pinched up into a cusp that typically points away from the Sun,

and often form long arcades of similarly oriented arches, such that the streamer tips form a long sheet extending into interplanetary space. When the coronal magnetic field is relatively quiescent, streamers are seen in a long chain girdling the solar magnetic equator, called the streamer belt.

Another interesting coronal feature is a filament, a long line of cooler material stretched between two or more photospheric footpoints. Filaments appear as absorption features in $H\alpha$ radiation when seen against the solar disk, or as emission features (referred to as prominences) when seen off the solar limb.

Also seen in the corona are large regions where there is little emission, and what is seen is roughly radially oriented. These areas are called coronal holes, and the magnetic field lines there are referred to as “open”, though of course they are assumed to connect with another open field line of opposite polarity at some point far away from the Sun. Intermittent, bright, radial features that appear and disappear in polar coronal holes are referred to as polar plumes.

1.4.2 Magnetic Reconnection

Magnetic reconnection is a process by which the magnetic field topology is rapidly reorganized. Figure 1.4 shows a simple model of a 2-dimensional reconnection scenario. The process is started when magnetic field lines of opposite polarity are brought close together by fluid flows. In accordance with Ampère’s law, a current sheet develops between the two magnetic regions. In the vicinity of the current sheet – an area called the diffusion region – the plasma- β parameter is much greater than elsewhere in the corona, allowing cross-field motion of the plasma. This allows

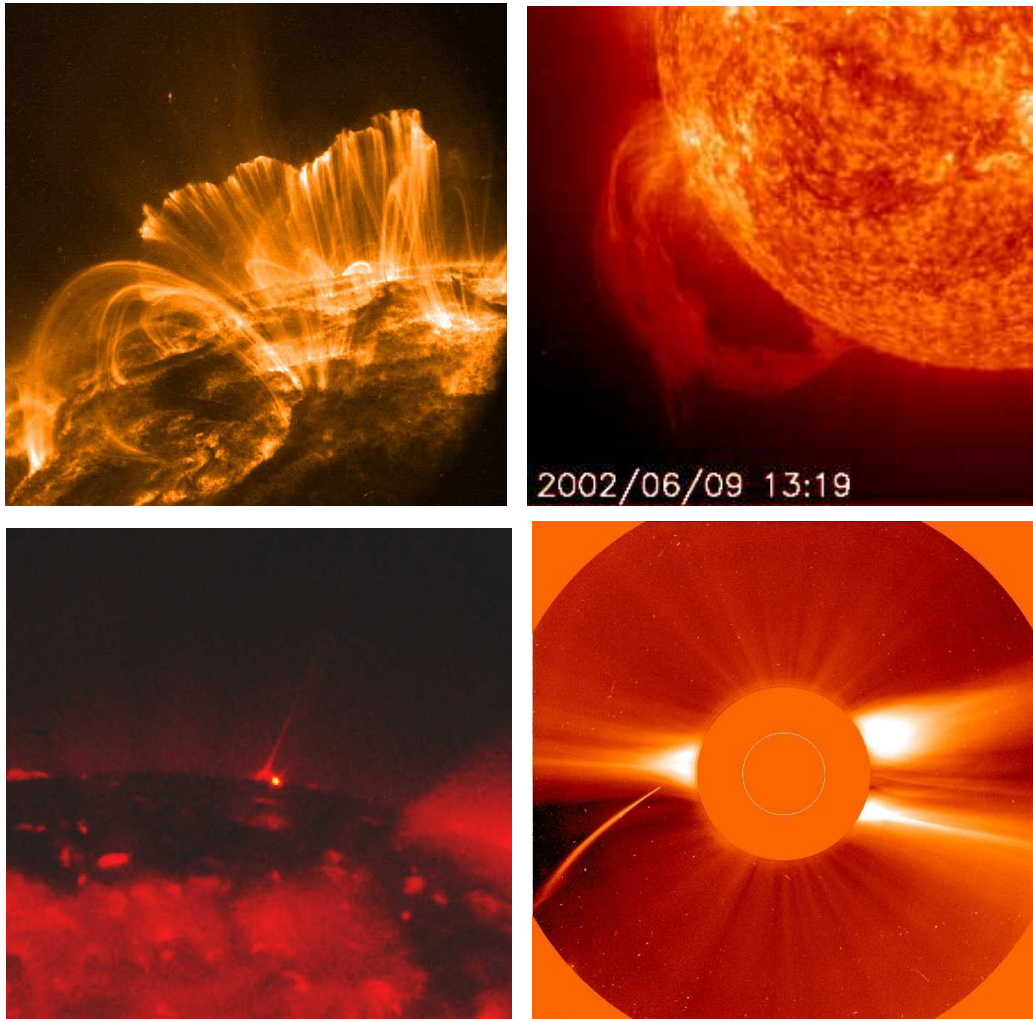


Figure 1.3: Some images highlighting coronal features: TRACE image of an active region (top left), EIT image of a prominence (top right), XRT image of a coronal hole with a plume (bottom left) and a LASCO C2 coronagraph image of the streamer belt (bottom right). Images courtesy of NASA.

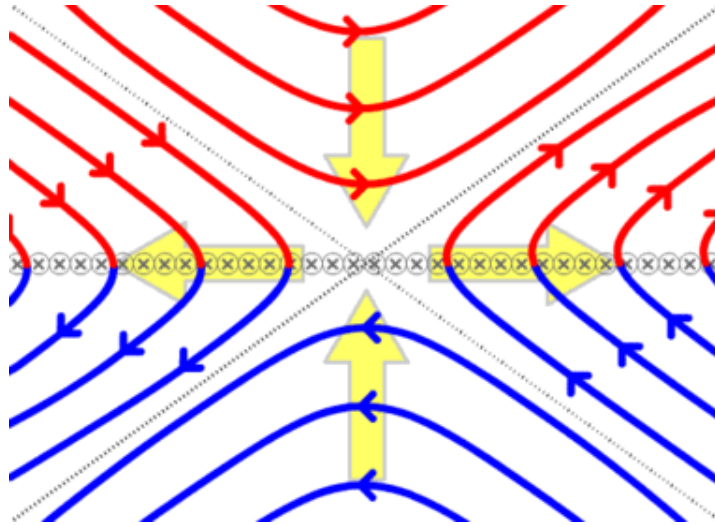


Figure 1.4: A simple 2-dimensional magnetic reconnection model. Plasma flow forces magnetic fields of opposite polarity together. Where the two fields come together the magnetic topology is abruptly altered, leading to the conversion of magnetic energy into kinetic and thermal energy.

the magnetic field lines to reorganize, forming two new, highly curved field lines as shown in figure 1.4. The high curvature of the new field lines induces a strong magnetic restoration force which pulls plasma rapidly away from the diffusion region. The resulting vacuum pulls more nearby field lines into the diffusion region, perpetuating the reconnection process. See [11] and references therein for a thorough description of efforts to model magnetic reconnection.

The simple picture shown in figure 1.4 is considerably more complicated in three dimensions, and there are still discrepancies between theory and observation. However, magnetic reconnection is widely believed to be responsible for a staggering number of observed phenomena in space physics. (See [5] and references therein.) Figure 1.5 shows an image of an apparent magnetic null point in the corona.

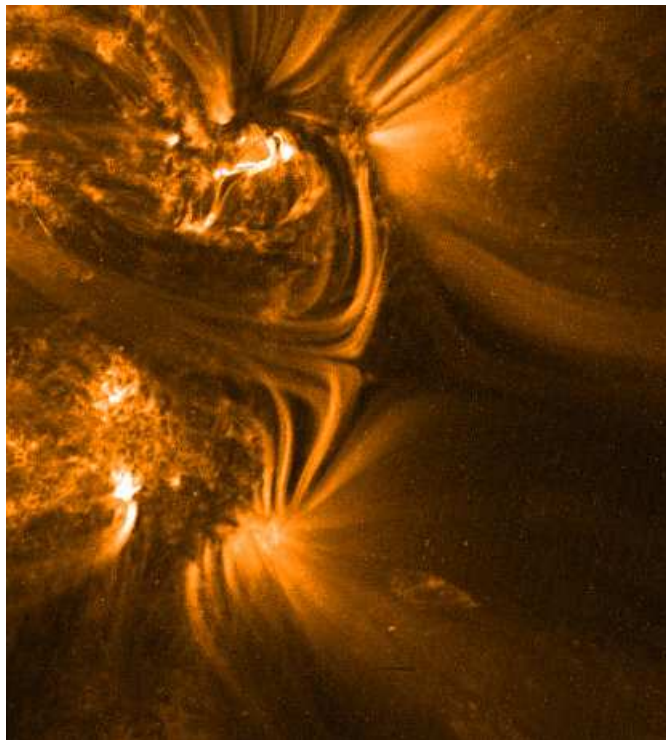


Figure 1.5: A TRACE spectroscopic image of the solar corona at 171 Å (an Fe IX emission line), showing an apparent magnetic null point in the corona. This wavelength channel highlights material at approximately one million kelvin.

1.4.3 The Solar Cycle

One of the many fascinating mysteries of the Sun is its magnetic cycle. The dipole component of the solar magnetic field reverses itself every 11 years, with much magnetic evolution taking place between reversals. Many of the features discussed in the previous sections are affected by this cycle. The start of a new magnetic cycle follows a period of very low numbers of sunspots and very simple solar magnetic field, and is marked by the sudden emergence of new sunspots at middle latitudes. (See figure 1.6.) These sunspots are believed to be the result of magnetic flux ropes whose field is strengthened in the tachocline, causing them to rise buoyantly and break through the photosphere to protrude into the corona; sunspots are seen where the flux ropes emerge [6]. Bipolar sunspot groups in the northern hemisphere generally have identical east-west polarity that reverses with each reversal of the overlying magnetic field; the same behavior is observed in the southern hemisphere, except that the polarity is generally opposite to that of the northern hemisphere.

As the magnetic cycle progresses individual sunspots come and go, but the mean latitude at which sunspots appear steadily decreases in both hemispheres, while the number of sunspots increases and the coronal magnetic field gradually becomes more complicated, with more active regions and a more distorted streamer belt (see figure 1.7). Coronal holes, primarily found at high latitudes at the beginning of the solar cycle, begin to appear across the solar disk. The activity level of the Sun begins to increase as well, with more CMEs and solar flares observed. (See section 1.5.2). This gradual buildup of magnetic complexity and activity is called

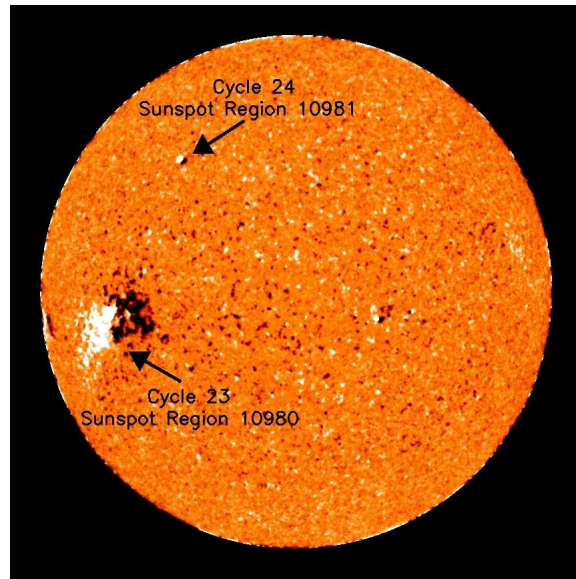


Figure 1.6: A magnetogram showing the emergence of the first mid-latitude sunspot of solar cycle 24. A large, older sunspot from solar cycle 23 is seen in the equatorial region. Image courtesy of NOAA.

the rising phase of the solar cycle, and the activity peak is referred to as solar maximum. It is during solar maximum that the solar magnetic field reverses, flipping the north and south magnetic poles.

Once maximum has passed the number of sunspots gradually decreases and the streamer belt moves toward the solar equator, flattening. Coronal holes once again begin appearing more often in the polar regions until finally the solar magnetic field is mostly composed of large open regions at each pole and a few decaying active regions. This is referred to as solar minimum, and is terminated by the appearance of new sunspot pairs at middle latitudes marking the start of the next solar cycle.

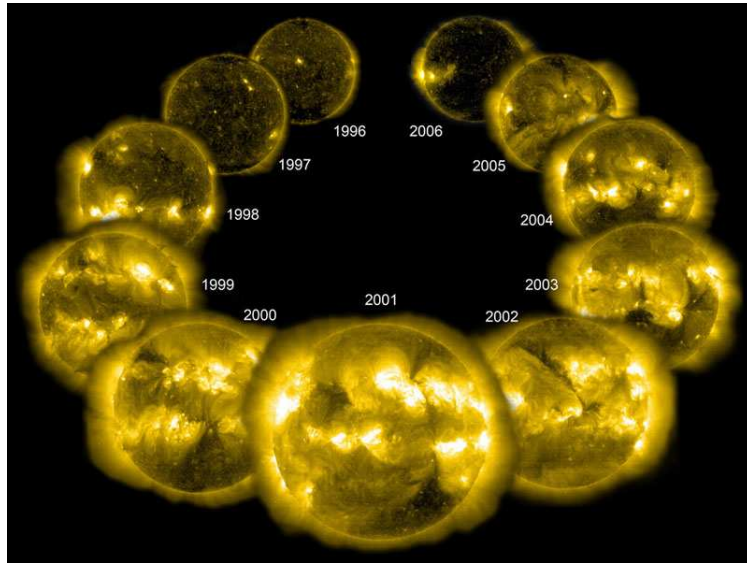


Figure 1.7: A composite of 284 Å spectroscopic images of the corona, produced by the EIT instrument on the SOHO spacecraft. The bright material in this image is approximately two million kelvin. Image courtesy of SOHO (ESA & NASA).

1.5 Mass Loss from the Corona

Mass is constantly lost from the solar corona, on the order of 10^{16} kg per year. Material escapes the Sun through the solar wind, CMEs, and other impulsive events. This mass loss is a tiny fraction of the mass of the Sun, but it has important consequences for humanity.

1.5.1 Solar Wind

The solar wind is the steady outflow of hot, low-density, magnetized plasma from the solar corona. It fills the region of interstellar space around the Sun, flowing supersonically to a distance of around 75 – 100 AU, where a shock called the termination shock is formed by the interaction of the solar wind with the local interstellar medium [88]. The solar wind is usually divided into two categories, slow wind

and fast wind, with the dividing speed usually about 400 km/s. Slow solar wind originates from regions of the corona with closed magnetic fields, such as streamers, while the fast wind comes from open field regions like coronal holes [67, 99]. The fast wind has a density of about $3\text{ions}/\text{cm}^3$ and about 4% of the ions are helium, while the slow solar wind has a density of about $8\text{ions}/\text{cm}^3$ at $1AU$ and has a more variable helium content that averages around 2% at $1AU$ [42].

Despite the attention paid to it over the last several decades, there are still many open questions about the solar wind. Of particular importance are questions about the source material and the acceleration mechanism for the solar wind, which is inconsistent with simple expansion due to plasma pressure.

1.5.2 Coronal Mass Ejections

The solar wind, while variable, represents a constant outflow of solar material. Figure 1.8 shows another, more impulsive mechanism by which particles leave the corona: a CME. CMEs are massive collections of coronal plasma and embedded magnetic fields that break away from the Sun and accelerate into interplanetary space. Each CME carries on the order of $10^{13} - 10^{17}$ g of material into interplanetary space [29]. The mechanism by which CMEs are impulsively ejected from the Sun is still hotly debated, and understanding it is an important goal of solar physics.

CMEs sometimes occur in conjunction with solar flares, sudden increases in electromagnetic radiation from localized sources in the low solar atmosphere (see [33] and references therein.) Solar flares were once thought to cause CMEs, but it is now known that many CMEs occur with no apparent observed solar flare, and the

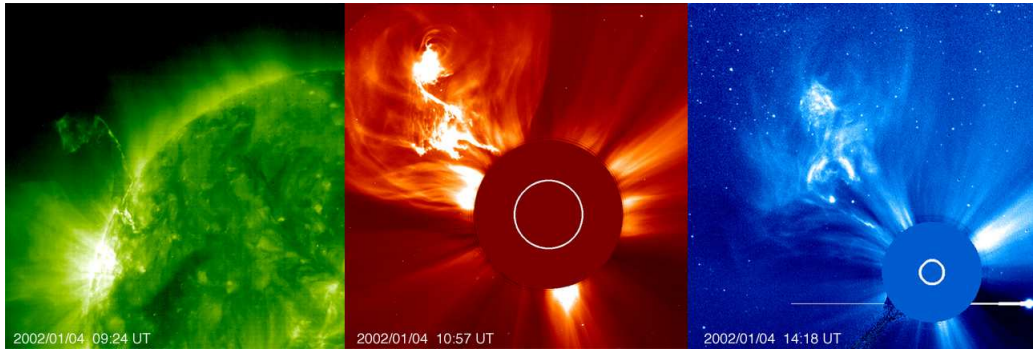


Figure 1.8: A CME seen in several SOHO instruments. The left (spectroscopic) image shows the CME in 195 \AA (about one million kelvin), the middle shows it some time later in the C2 white-light coronagraph (the white circle represents the edge of the solar disk) and the right shows it even later in the C3 coronagraph. Image courtesy of SOHO (ESA & NASA).

relative timing of coincident CMEs and flares is variable. The exact relationship between flares and CMEs is still an open question.

1.5.3 Everything in Between

Observationally CMEs can be defined as “new, discrete, bright features appearing in the field of view of a white-light coronagraph and moving outward over a period of minutes to hours” [83]. At present there are a number of observed eruptive coronal phenomena that do not meet most scientists’ standards for a CME, but which seem to be more substantial than solar wind [74, 68, 61, 40]. It is unclear whether these objects represent small CMEs, some sort of ancillary effect of CMEs, or another phenomenon, physically distinct altogether from CMEs. Chapter 5 discusses our measurements of these features using the STEREO COR1 coronagraph.

1.6 Impact of Solar Processes on Humanity

Understanding and predicting CMEs and conditions in interplanetary space is one of the most important goals of space physics. These so-called “space weather” conditions are of vital interest to humanity. CMEs can be damaging to electronic equipment and hazardous to people outside the protection of the Earth’s magnetic field because they contain energetic charged particles and frozen-in magnetic fields. Because they also carry frozen-in magnetic flux, they can have a strong impact on the Earth’s magnetic field when they collide with it. They can cause compaction of the geomagnetic field, and can deposit large numbers of charged particles into the Earth’s atmosphere. (See figure 1.9 for an artist’s conception of an Earth-directed CME.) The subsequent atmospheric disturbances can cause communications disruptions, global positioning system (GPS) inaccuracies, power outages, and equipment failures here on Earth. Increasing our understanding of the complex processes taking place on the Sun is critical for accurate prediction and prevention of these types of disruptions.

1.7 Summary

The solar corona is the outer part of the atmosphere of the Sun. It is roughly three orders of magnitude hotter than the visible surface of the Sun, and its behavior is dominated by the solar magnetic field. Material escapes from the corona constantly, in the form of both steady flows and impulsive ejections in a range of sizes. The mechanisms by which the coronal material is heated, and by which it

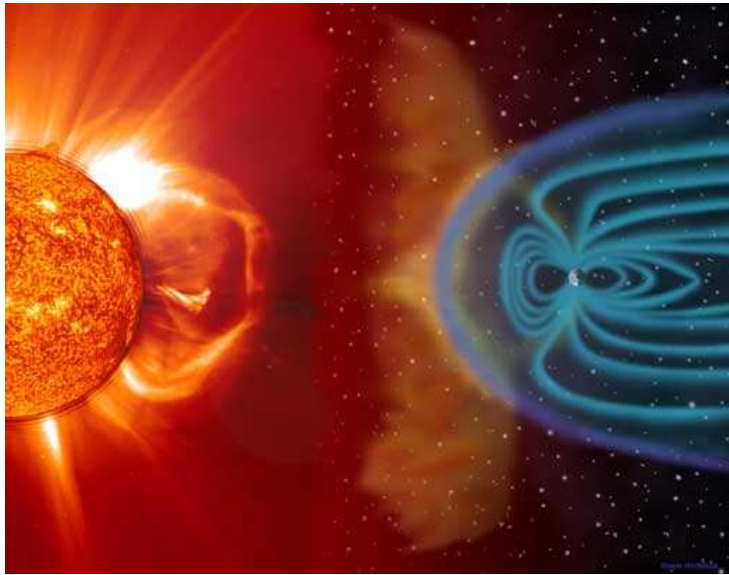


Figure 1.9: An artist’s rendition of a CME headed toward Earth. Image courtesy of NASA/Steele Hill.

escapes the Sun, are not well understood despite their importance and despite many decades of study.

1.8 Outline of the Thesis

The preceding was a basic review of the important solar physics background necessary to understand the motivation and content of this thesis. In chapter 2 I describe observable properties of the solar corona in greater detail, and describe the STEREO COR1 coronagraphs used to make the images I analyze in later chapters. Chapters 3 and 4 describe measurements of rotation rates in the solar corona. In chapter 5 I present a characterization of so-called “plasma blobs” ejected from the corona. Finally, chapter 6 contains a discussion of my results and a list of ideas for future work.

Chapter 2

The STEREO Mission and the COR1 Coronagraph

2.1 Introduction

Studying the solar corona, like many astrophysical endeavors, is very different from conducting laboratory experiments on Earth. Our laboratory is millions of miles away, and extremely hostile to instrumentation. The only way to observe the processes taking place in the corona is to study its output: electromagnetic radiation and the solar wind. In this chapter I describe the electromagnetic spectrum of the corona, the Solar TERrestrial RELations Observatory (STEREO) mission, and the COR1 coronagraph used to make the images used in this thesis.

2.2 Observing the Corona

As mentioned above, study of the corona is limited to imaging of its electromagnetic signal and to studies of the particles and fields of the solar wind. Here I concentrate on the electromagnetic spectrum of the corona. Coronal light is generally divided into three components: F-corona, K-corona, and E-corona. Figure 2.1 shows the relative strengths of the three coronal components as a function of radial distance from the Sun. The F-corona is the innermost part of the zodiacal light, photospheric light that is scattered by dust particles in the ecliptic plane, and as such is not true coronal light. I will focus on the E-corona and K-corona, which are of greater interest to solar physicists.

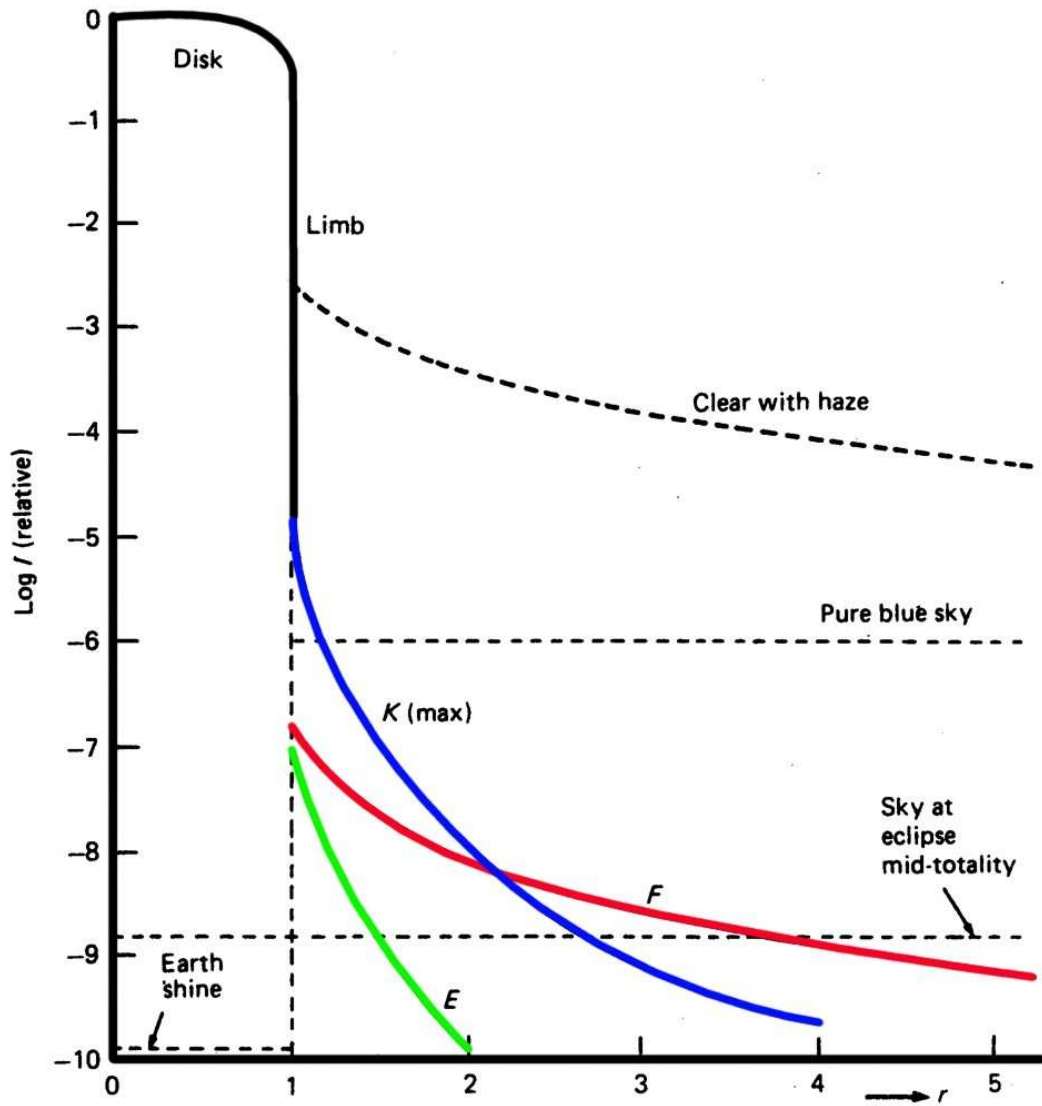


Figure 2.1: Plot showing the brightness of the three components of the corona, relative to the brightness of the solar disk. The intensity of the K-corona varies slightly with phase of the solar cycle; it is shown at solar maximum. Dashed lines indicate the brightness of the sky for several observing conditions on Earth. Figure courtesy of S. St. Cyr, private communication.

2.2.1 Coronal Emission

The E-corona is the portion of the coronal light that is actually emitted by coronal material. It consists of a discrete series of spectral lines, primarily in the ultraviolet (UV) and X-ray portion of the spectrum. These lines are produced by highly ionized heavy atoms, mainly Fe, Si, S, and O. While these lines are faint against the background of the light emitted by the F- and K-corona, they can be seen clearly in the low corona when a small enough spectral window is examined [28]. Several of the images shown in chapter 1 (for example, figures 1.3 and 1.5) are produced by isolating a single strong spectral line.

2.2.2 Scattering of Photospheric Light by Coronal Electrons

The K-corona is the portion of the coronal light that is produced by Thomson scattering of photospheric light from electrons in the corona. Since both the F- and K-corona are produced by scattering of photospheric light, they have very similar spectra, and at radial distances above about $2-2.5R_{\odot}$ the F-corona is brighter than the K-corona [28] (see figure 2.1.) However, the two components can be separated by exploiting the fact that the K-corona is highly polarized parallel to the solar limb¹, while the F-corona is thought to be unpolarized close to the Sun [28, 44].

Figure 2.2 illustrates the geometry of Thomson scattering in a plane containing the Sun, the scattering electron, and the observer, assuming that the Sun is a point source. Photospheric light is emitted from the Sun and travels radially away from it, polarized perpendicular to the direction of travel. When this light is scattered

¹Light emitted by the Sun is polarized perpendicular to the direction of travel; when it scatters from coronal electrons the component polarized parallel to the new direction of travel is removed.

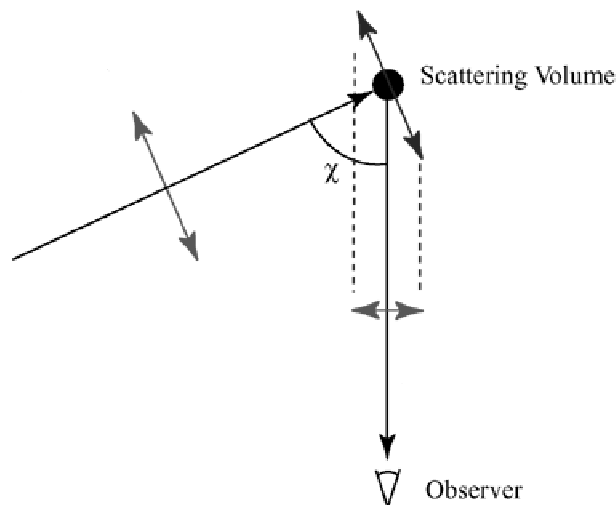


Figure 2.2: Diagram illustrating the geometry of Thomson scattering. Light traveling from the source towards the scattering volume can be divided into two polarization components, one in and one out of the plane of the paper. The component in the plane of the paper, when scattered, is reduced according to the cosine of the angle χ .

by a coronal electron, the light scattered in the direction of the observer must come from that portion of the photospheric light that was polarized perpendicular to the new direction of travel.

From inspection of figure 2.2 one can see that the signal seen by the observer is mostly strongly polarized when χ is 90° . Extending this picture to three dimensions one can imagine a plane, containing the solar center, and perpendicular to the observer's line-of-sight (LOS). Light scattered towards the observer from electrons in this plane, called the plane of the sky (POS), is more strongly polarized than that scattered from anywhere else, and the strength of the polarization decreases with increasing distance from this plane.

In order to understand the observed K-corona signal, we must consider two

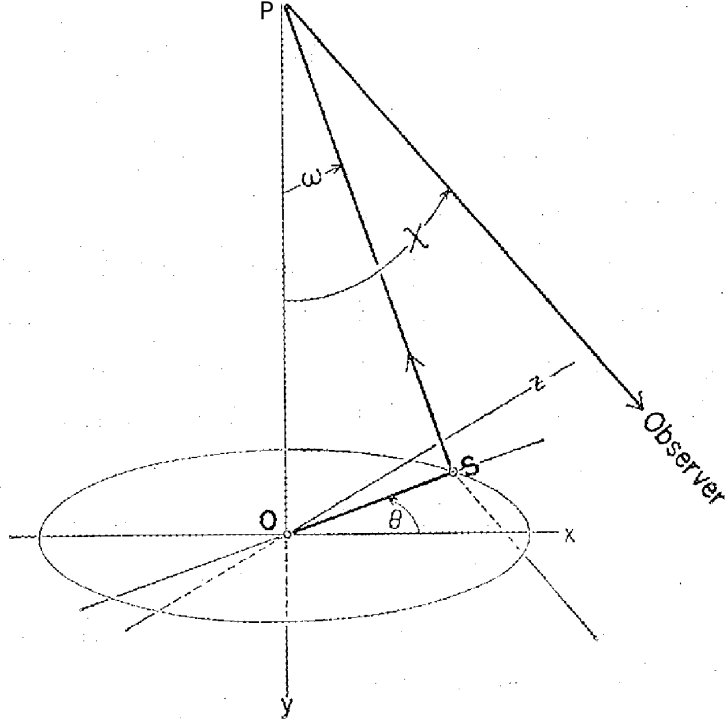


Figure 2.3: Diagram showing scattering of photospheric light from a point S in the photosphere by electrons at a point P in the corona. The point O is the nearest point on the solar surface to the point P . (Reproduced with permission [10].)

complications to the simple scattering scenario seen in figure 2.2. First, the Sun is not a point source; it emits photons over an extended surface. Figure 2.3, taken from Billings [10], shows the 3-dimensional scattering geometry. He describes the scattered light from a point P toward an observer in terms of the components polarized tangential to the apparent solar surface, I_{tan} , and normal to it, I_{rad} . The quantity $I_{tan} - I_{rad}$ is called the polarized brightness (pB). Using the variables as labeled in the figure, the pB light scattered from a small volume of the corona is:

$$pB = I_{tan} - I_{rad} = \frac{I_0 \pi \sigma}{2} N_e \sin^2 \chi [(1 - u)A + uB] \quad (2.1)$$

$$A = \cos \Omega \sin^2 \Omega \quad (2.2)$$

$$B = -\frac{1}{8}\left[1 - 3 \sin^2 \Omega - \frac{\cos^2 \Omega}{\sin \Omega}(1 + 3 \sin^2 \Omega) \ln \frac{1 + \sin \Omega}{\cos \Omega}\right] \quad (2.3)$$

where I_0 is the photospheric intensity at Sun center, σ is the Thomson cross section, N_e is the electron density at P , and u is a numerical factor that accounts for the decrease of the photospheric brightness from the Sun's center to its edge, a phenomenon known as limb darkening.

The second complication is that the corona is not composed of one electron but many. When we look at the Sun we perceive a solid surface, though no such surface exists. The illusion of solidity comes from the fact that below some finite depth along our LOS there is very little probability of photons from below escaping before being scattered by an intervening ion. Thus, the Sun is said to be optically thick. The corona, however, is optically thin; it is generally possible to look through the corona and see distant stars. This means that when we look at the corona, we can see light scattered by electrons all along our LOS, and the information localizing those electrons along the LOS is lost. The coronal signal is thus said to be *integrated* along the LOS.

However, using pB images partially mitigates the problem of LOS integration. Recall that the polarization of coronal scattered light decreases with distance from the POS. From equation 2.1 we can see that the pB signal falls off as $\sin^2 \chi$. The prominence in pB images of events close to the POS allows us to localize the source of the signal to some extent. So, the polarization of the K-corona not only helps distinguish it from the F-corona, it also helps reduce the problem presented by optical thinness.

2.3 The STEREO Mission Concept

The STEREO mission is a revolutionary upgrade to the current fleet of solar observing missions for two reasons: the positioning of the satellites and the opportunity they provide to view Coronal Mass Ejections (CMEs) and other solar phenomena simultaneously from multiple viewpoints. STEREO consists of a pair of satellites with identical instrument suites designed to orbit the Sun at nearly 1 AU just ahead of (the Ahead spacecraft) and behind (the Behind spacecraft) the Earth, at gradually increasing angular separation from Earth (see figure 2.4).

In the past coronagraphs have been placed almost exclusively on or near the Sun-Earth line [41]. For space-based telescopes this had the advantage that in-situ instruments on the same satellites could characterize the properties of the solar wind plasma upstream of the Earth. The downside is that this is not a very good viewing angle for coronagraph images of Earth-bound CMEs. CMEs that head directly toward (or away from) the satellite appear in coronagraph images as faint white rings around the Sun, and are referred to as halo CMEs [37]. Measuring the speed of propagation of Earth-directed CMEs is an important component of space weather prediction, and is difficult to do with halo CME images. The unique trajectories of the STEREO spacecraft allow for oblique observation of Earth-directed CMEs.

More than offering a unique viewpoint for studying Earth-bound phenomena, the STEREO satellites actually offer two simultaneous viewpoints, which has many advantages. The angular separation of the two satellites increases by approximately 45° per year, which has allowed for a number of studies not possible

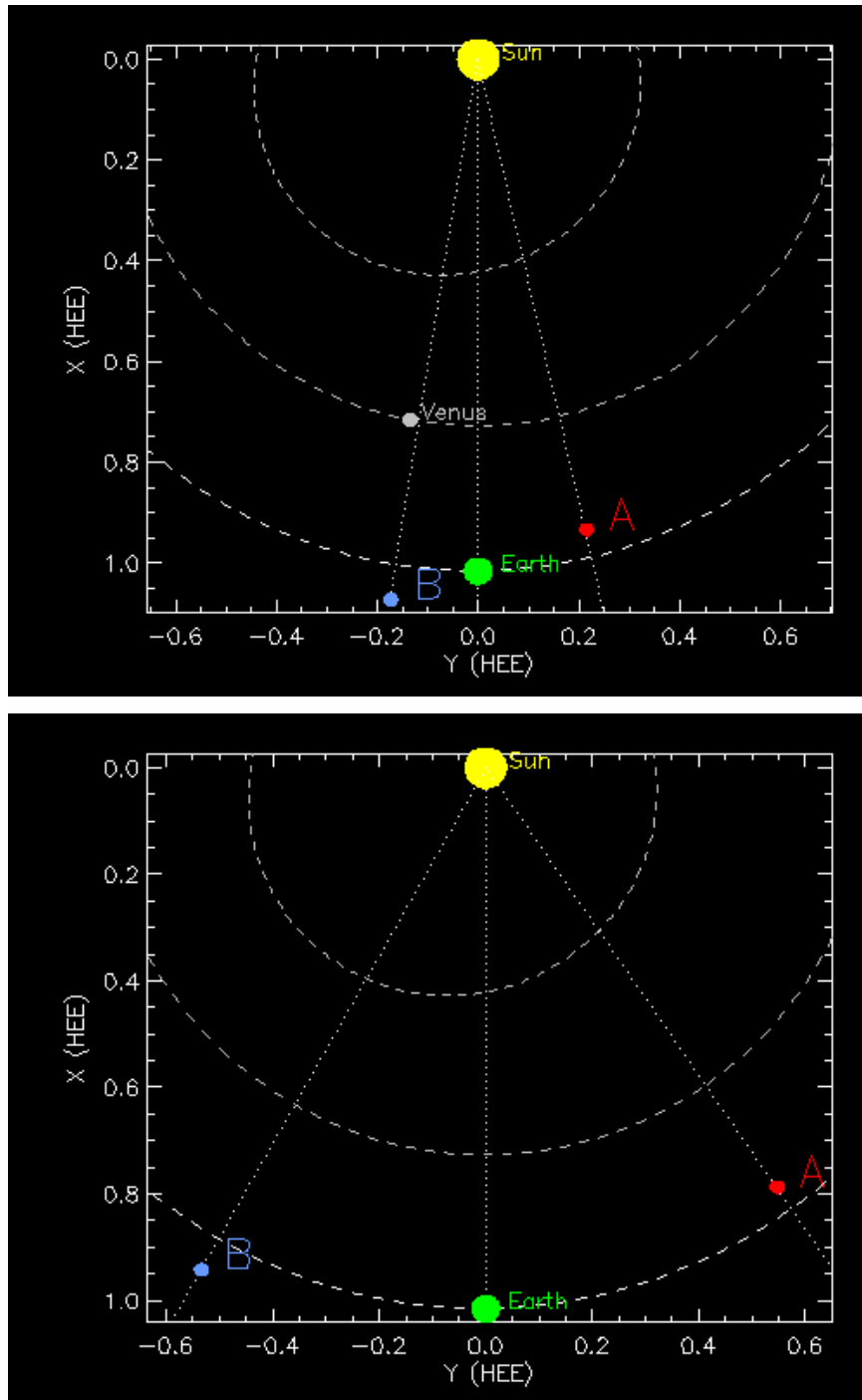


Figure 2.4: The positions of the two STEREO spacecraft with respect to the Earth and the Sun on August first of 2007 (a) and 2008 (b). ‘A’ indicates the position of the Ahead spacecraft, while ‘B’ indicates the Behind spacecraft.

before STEREO. Early in the mission, at a satellite separation around four degrees, STEREO images were ideal for the creation of 3-D movies of the transition region and lower corona. Additionally, small separation angles ideally positioned the satellites for 3-dimensional studies of coronal loops and CME fronts. As the separation angle grew it was possible to measure 3-dimensional CME trajectories and speeds. Around ninety degrees they were ideally situated for comparison of images of CMEs and other transient phenomena from one spacecraft with in-situ particle and field data from the opposite spacecraft [41]. As they neared 140° separation the viewing angle was optimal for tomographic reconstructions (see appendix 6.4) [17]. In short, the multiple viewing angles of STEREO open up many scientific possibilities. In chapter 4 I exploit the multiple viewing angles of STEREO to study coronal rotation on short timescales for the first time.

2.4 The COR1 Coronagraph

2.4.1 Instrument Design

Observing the K-corona is different than observing the E-corona, because much of the E-corona light is emitted in a spectral range where the photosphere is not very bright. The K-corona, on the other hand, is imaged in what is referred to as “white light”, which is really a relatively broad spectral window in the visible spectrum. In white-light images the photosphere is quite bright.

Unfortunately, because of the low density of the corona, the light it scatters is about six orders of magnitude less intense than the photosphere, and so is overwhelmed by the photospheric signal. This is why the corona was originally observed

only during total solar eclipses. In order to image the relatively faint corona without the interference of photospheric light, we create an artificial eclipse, using a coronagraph. A coronagraph is a telescope with an occulting disk that covers the solar disk and some of the surrounding inner corona.

The COR1 coronagraph is the instrument used to make the images analyzed in this thesis. COR1 is an internally occulted Lyot coronagraph [52, 28]. Figure 2.5 shows the optical layout of the instrument, described in detail by [92]. Light passes through the objective lens, which focuses it onto the occulter. COR1 uses an internal, conical occulter to direct photospheric light into a wedge-shaped light trap. Further along the optical path, a Lyot stop removes light diffracted from the entrance aperture. Behind the Lyot stop is a positive power, doublet lens with a Lyot spot on the front to remove ghosting from the objective lens. Immediately after the first doublet lens is the bandpass filter, followed by the rotating polarizer. A second doublet lens focuses the light onto the detector plane, where a focal plane mask removes light scattered from the occulter.

The COR1 bandpass filter has a 10 nm spectral window centered on 656 nm, the wavelength of the $H\alpha$ emission line. The rotating polarizer suppresses stray light and is used to create pB images as described above. For a thorough discussion of the COR1 stray light characterization see [92].

The corona in COR1 images is bounded at an inner radius set by the occulter size, at approximately $1.4R_{\odot}$ from Sun center. The outer radius of the images is set by the front aperture and Lyot stop, and corresponds to approximately $4R_{\odot}$, though part of the annular image falls off of the square charge-coupled device (CCD). These

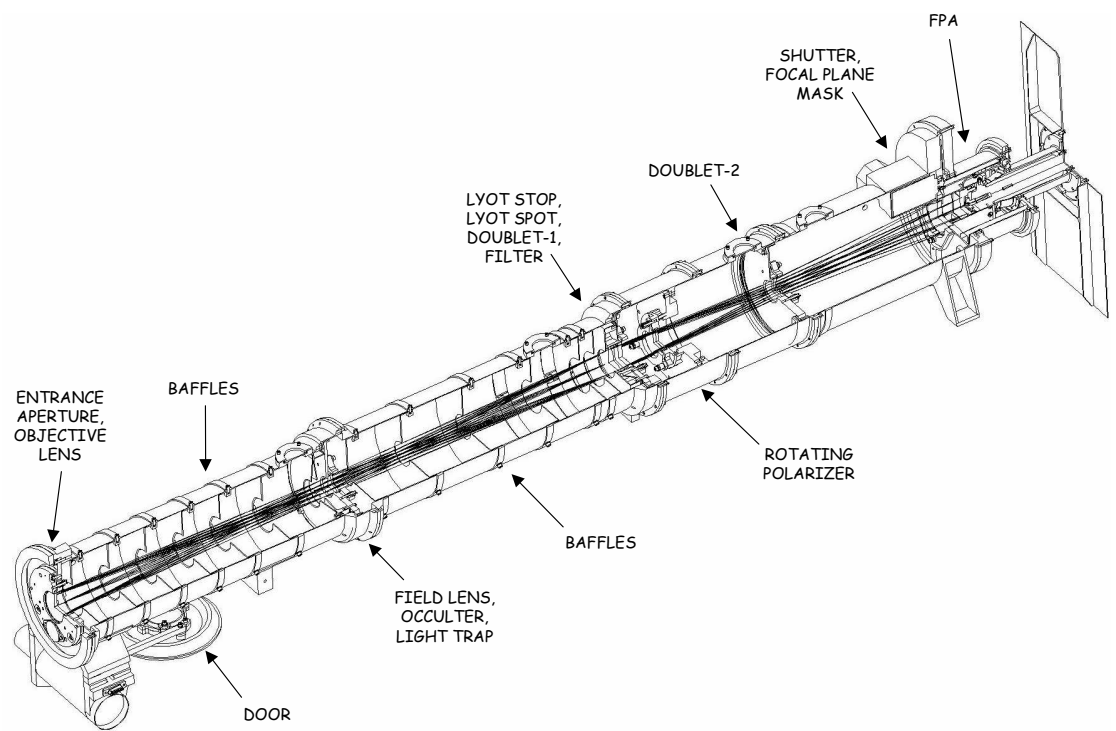


Figure 2.5: A schematic showing the optical layout of the COR1 coronagraph. (Reproduced with permission [92].)

numbers vary slightly throughout the mission due to changes in the distance between the satellite and the Sun. Also, the telescope was deliberately pointed slightly away from Sun center several months into the mission in order to accommodate the optical alignment of another instrument, so the inner and outer radii vary slightly depending on the angular position within the image. The CCD is a grid of 2048 x 2048 pixels, which are binned to 1024 x 1024 resolution onboard the satellite, giving an angular resolution of approximately 7.5". At 1 AU this is equivalent to about 5.4 Mm per pixel.

2.4.2 COR1 Data Processing

Figure 2.6 shows a sample COR1 image, in both the raw and processed forms. The second image has undergone extensive processing to bring out the K-corona. The original data are in the form of sets of three linearly polarized images, typically taken about 9s apart and exposed for 1.7s each. Between images the polarizing filter is rotated 120°, so the resulting three-image set can be used for the calculation of polarized brightness images. Image sets were generated at a cadence of 10 minutes during most of 2007 and 2008.

Minimally processed COR1 data files are distributed to the science community along with software to process the images into science-quality data products. The software package used to calibrate COR1 images is called *secchi_prep*, and is distributed through the SolarSoftWare library [24], a set of integrated software libraries developed for use with many solar physics missions and freely distributed through the internet. The *secchi_prep* software adjusts the images for exposure time,

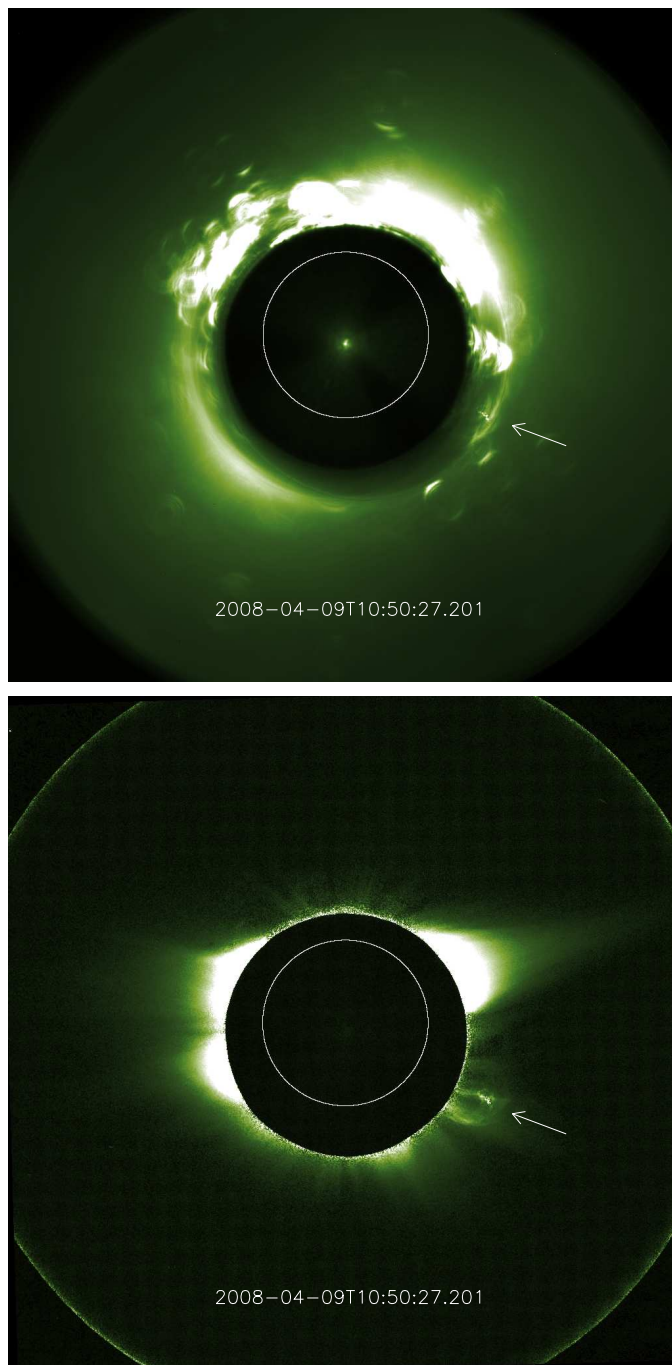


Figure 2.6: Top: An unprocessed STEREO COR1-B image. Bottom: a processed STEREO COR1-B pB image. The arrows indicate a small CME in progress. The white circles drawn over the occulter in both images indicate the approximate location of the solar limb.

converts them from units of digital number to mean solar brightness (see [93] for details on the calibration of COR1), and corrects for a slight vignetting near the occulter. It also rotates the images from both spacecraft so that solar north is at the top. Detailed information about *secchi_prep* can be found at http://sohowww.nascom.nasa.gov/solarsoft/stereo/secchi/doc/secchi_prep.html.

Another important part of the *secchi_prep* processing for COR1 is background subtraction. Even when studying pB images there is still a significant amount of light in coronagraph images from the F-corona and from light scattered in the instrument. In order to remove this light from the images, many coronagraphers exploit the fact that it is a relatively constant component of the signal. There are three ways to do this: (1) by subtracting a pre-event image (for example, an image made just before a CME), (2) by subtracting from each image in a sequence the image made immediately before it (called a running-difference movie) or (3) subtracting an empirically measured background image. The first two methods are very useful for studying impulsive events like CMEs that cause large changes in the corona.

As for method (3), there are many different ways to measure the appropriate background image to subtract. The COR1 instrument team uses two different methods, sometimes in combination, to calculate background images. The first method splits each day's worth of data evenly into shorter time segments in which it finds the median value of each pixel. Then the minimum value of the day's worth of medians is extracted. Finally, the minimum daily value over a month's worth of data is calculated for each pixel and the results are used to form a background image

that contains as much scattered light and as little K-corona as possible [94]. These 30-day backgrounds are generated every ten days and are automatically subtracted by the *secchi_prep* software.

The second background subtraction method uses image series exposed during slow satellite rolls. Roll-based backgrounds can be superior for some applications, but they produce less consistent results over the course of the long data sets in this study [93] and so are not used here.

2.5 Summary

There are three main components to the coronal spectrum: the F-, E-, and K-corona. The F- and K-corona result from scattering of photospheric light, while the E-corona is the product of emission of coronal ions. The component of interest for this study is the K-corona, which consists of photospheric light scattered by electrons in the corona. Light scattered by coronal electrons is strongly polarized and this fact is used to distinguish it from the F-corona.

We measure the intensity of the K-corona using polarized brightness images from the COR1 coronagraphs onboard the twin STEREO spacecraft. The STEREO spacecraft are in orbit around the Sun ahead of and behind the Earth, with their angular separation increasing by approximately 45° per year. Their unique perspectives enable studies like the one in chapter 4 that were previously impossible.

Chapter 3

COR1 Coronal Rotation Rate Measurements

3.1 Introduction

This chapter deals with coronal rotation. The first section reviews measurements of rotation in the solar photosphere and in the corona. Section 3.2 details the preparation of the STEREO COR1 data used in this rotation study, and section 3.3 details the methods used to search for rotation signatures in the COR1 data. Section 3.4 discusses the question of spectral significance. Coronal rotation measurements using COR1 are given in section 3.5, and section 3.6 discusses the influence of projection effects on the coronal rotation rate. Conclusions are presented in section 3.7.

3.1.1 Rotation of the Solar Photosphere

The Sun is not a solid body and does not rotate rigidly. The photosphere of the Sun is observed to rotate differentially, with the fastest rotation rate at its equator and gradually decreasing rates with higher latitude. The differential rotation of photospheric features has been a topic of interest throughout the modern era of space exploration, in part because of its relationship to the solar dynamo below and magnetic activity above [39].

Many authors express the latitudinal dependence of the rotation rate in terms of the formula:

$$\Omega(\phi) = A + B \sin^2 \phi + C \sin^4 \phi \quad (3.1)$$

where Ω is the rotation rate, ϕ is the solar latitude and A , B , and C are fitted constants. While some authors have objected to the use of equation 3.1 because the constants B and C appear to be inversely correlated (see [9] and references therein), and while coronal rotation rates don't always appear to obey this relationship except in an average sense (see, for example, figure three of [20]), it is useful for comparing new studies to historical results. Reviews of the seminal papers measuring photospheric rotation rates using several different methods are given by [9, 64], with thorough discussion of the problems and errors inherent to each. Table 3.1 gives a sampling of rotation measurements presented in those two papers.

Values obtained for A , B , and C in equation 3.1 tend to depend on the measurement technique being used; agreement between authors using the same measurement technique tends to be higher than agreement between those measuring different phenomena. For example, in table 3.1 one can see that studies based on tracer measurements give generally faster rotation rates than those based on spectroscopic measurements. Also, from Howard et al. [35] one can see that larger sunspots seem to rotate more slowly than smaller ones. It is believed that this variation between results obtained using different methods is the result of genuine differences in the rotation rates of the features studied. This idea is reinforced by the consistent differences between the photospheric measurements and those obtained in coronal studies.

| Reference | A | B | C | Time | Period | Notes |
|------------------------------------|--------|--------|--------|-----------|--------|-------|
| <i>Spectroscopic Measurements:</i> | | | | | | |
| Howard and Harvey [36] | 13.76 | -1.74 | -2.19 | 1966-1968 | 28.18 | (1) |
| LaBonte and Howard [47] | 14.23 | -1.54 | -2.80 | 1967-1980 | 27.18 | |
| Howard et al. [34] | 14.19 | -1.70 | -2.36 | 1967-1982 | 27.26 | (2) |
| Snodgrass et al. [79] | 14.112 | -1.69 | -2.35 | 1967-1982 | 27.43 | (3) |
| Pierce and Lopresto [58] | 14.07 | -1.78 | -2.68 | 1979-1983 | 27.52 | (4) |
| Ulrich et al. [96] | 14.044 | -2.030 | -2.074 | 1967-1987 | 27.570 | (5) |
| <i>Tracer Measurements:</i> | | | | | | |
| Newton and Nunn [57] | 14.368 | -2.69 | | 1878-1944 | 26.902 | |
| Ward [104] | 14.523 | -2.69 | | 1905-1954 | 26.594 | |
| Howard et al. [35] | 14.549 | -2.869 | | 1921-1982 | 26.543 | (6) |
| | 14.440 | -2.616 | | 1921-1982 | 26.758 | (7) |
| | 14.282 | -2.636 | | 1921-1982 | 27.076 | (8) |
| Snodgrass and Ulrich [81] | 14.252 | -1.678 | -2.401 | 1984-1987 | 27.138 | (9) |
| Komm et al. [45] | 14.420 | -2.005 | -2.089 | 1975-1991 | 26.798 | (10) |

(1) MWO data; very large daily scatter due to several instrumental error sources.

(2) MWO data; Applied a scattered light correction

(3) Same data as (2), but with correction for erroneous dispersion

(4) Observed lines in photosphere and chromosphere; found no apparent height variation of rotation rate.

(5) Extension of (2).

(6) Sunspots with $area < 5 mHem$ (millionths of a hemisphere).

(7) Sunspots with $5 mHem < area < 10 mHem$.

(8) Sunspots with $area > 10 mHem$.

(9) Correlation of MWO magnetograms.

(10) Correlation of KPNO magnetograms.

Table 3.1: A summary of seminal photospheric rotation measurements, based on similar tables by [9] and [64]. The column labeled “Period” gives the corresponding equatorial synodic rotation period in days, while the constants A , B , and C are side-real values from equation 3.1 in degrees per day. The first section lists measurements based on spectroscopic (Doppler) observations, while the second lists measurements based on tracking of specific features or magnetic intensity patterns across the solar disk.

3.1.2 Rotation in the Corona

Measurement of rotation rates in the solar corona have also obtained different latitude dependencies, though a general consensus has emerged that the corona seems to rotate more rigidly than the photosphere, at something close to the equatorial rotation rate. However, the observed rigidity has been challenged by [50, 49], who point out that it may simply be an artifact of bright, low-latitude features being projected into higher latitude POS bins. This does not seem to be the case in the present study (see section 3.6).

The conclusion that the corona rotates more rigidly than the photosphere is puzzling, since logically it seems that if magnetic features in the corona are rooted in the photosphere as they appear to be, then either they must rotate at the photospheric rate or they must undergo shear and even separation from the fields below them on an ongoing basis. Such a process could have important implications for the perennial problems of coronal heating and CME initiation [50], as well as initiation of other coronal transients like those discussed in chapter 5.

Rotation studies in the corona fall into roughly three categories: low corona emission studies (8-12 Mm above the photosphere) [32, 12, 43, 105], emission line coronagraph studies [89, 27, 26, 86, 38, 75, 1, 4, 8, 7], and white-light coronagraph studies [20, 50, 49, 55]. Coronagraph rotation measurements are conducted by studying a time series of intensity from a particular point in the sky during a period of several solar rotations, typically one year. If the corona were unchanging and the observer stationary during this period, the observed intensity would show periodic

variation as different regions of the corona rotated in and out of the LOS. The rotation period can then be extracted by searching for periodic signals in the time series, for example using autocorrelation, or correlation with the time series from a corresponding point on the opposite limb of the Sun. This method of measuring the rotation rate will naturally be more reliable when coronal conditions are relatively stable over the duration of the time series. The recent extended solar minimum studied in this work provided just such conditions.

It has been suggested that one reason different studies obtain different results for the latitude dependence of the coronal rotation rate is that there are multiple rotation modes at some latitudes [7, 4, 89, 3], and the different measurement techniques weight the modes differently. Some authors have noted what they believe to be excess width in the rotation spectrum peaks, possibly due to the combination of multiple features rotating at slightly different rates [105, 8, 86]. Some studies have tried to measure the frequency and time/latitude dependence of these secondary spectral peaks by filtering a sinusoid at the main spectral frequency from the time series [105, 86]. The main problem with this approach is that it assumes the coronal density at fixed latitude and radius is a sinusoidal function of longitude. In general there is no physical basis for this assumption. In this study I use a different technique, following [85] to remove the main periodicity from the data in order to search for secondary periodicities (see section 3.6).

Another possible explanation for the differences in latitude dependence between studies is that this dependence varies over the course of the solar cycle. Indeed, some long-term studies have identified a solar cycle dependence [1, 7, 20, 75],

in contrast to photospheric studies, where variations in the rotation rate are limited to less than 1% of the measured values, and demonstrate an interesting variation with latitude (referred to as torsional oscillations) but no global trends towards more or less differential rotation [39]. Altrock [1] measured more differential rotation at high latitudes near solar minimum (with very rigid rotation during the rising phase) and more differential rotation at low latitudes during the rising phase (with very rigid rotation at solar minimum). He notes that this is the opposite of the results obtained from studies of the convection zone rotation [2]. Badalyan [7] found the rotation during the descending phase and at solar minimum to be much more rigid than during other parts of the solar cycle.

It is possible the solar cycle dependence of the rotation rate has to do with the increased complexity of the solar magnetic field at solar maximum. Near solar minimum the solar magnetic field can be well represented using just the first one or two terms of the multipole expansion [101]. As the solar cycle progresses from solar minimum to maximum and increasing numbers of sunspots appear on the solar surface, and an increasing number of multipolar components are needed to account for the complexity of the magnetic field. As Wang *et al.* point out, the combination of only a few low-order modes cannot rotate as differentially as the photospheric magnetic field, so near solar minimum one might expect the coronal field to be more rigid. However, their calculation of the coronal magnetic field expansion is based on a potential field extrapolation of a model photospheric field, and the true complexity of the coronal magnetic field is not known due to the extreme difficulty of measuring it.

The variation of the rotation rate with the solar cycle is potentially very interesting, but requires very long data sets to study. I will not address the solar cycle dependence in this thesis, but it must be kept in mind when interpreting results from shorter-duration studies like this one.

Finally, the outer corona seems to rotate more rigidly than the inner corona during at least some parts of the solar cycle [75], perhaps due to the fact that measurements in the outer corona have until now only been performed on long-lived features (lifetimes $> \frac{1}{2} - 1$ rotation period) – features like large streamers that survive long enough to be seen when they reappear. Some authors have suggested for both observational ([4, 3, 64, 20, 78, 75]) and theoretical ([98, 69]) reasons that small-scale, short-lived features may rotate differentially while large, long-lived features rotate rigidly. The dependence of the rotation rate on the size and/or lifetime of the observed feature may explain the observed solar-cycle effect on the latitude dependence; average feature size and lifetime varies with the solar cycle, with larger, longer-lived features found near solar minimum [20]. It might also explain why some observers find multiple components in the rotation signal, as long- and short-lived features would mingle in the observer’s LOS.

The contrast between photospheric and coronal rotation profiles suggests that the radial profile of the rotation rate in the corona may be of interest. For the most part coronal rotation studies have identified little or no radial dependence in the rotation rate. Lewis et al. [50] identified an increase in the rotation period of 0.3 ± 0.1 days between the Large Angle Spectroscopic Coronagraph (LASCO) C1 and C2 coronagraph field of views (FOVs) (roughly between $2 - 2.5R_{\odot}$), though C1

and C2 measure different coronal components: the E-corona and K-corona. Sime, Fisher and Altrock [75] have speculated that the slight difference they observed between the Fe XIV emission line corona and the white light corona might be due to the fact that the E-corona is temperature dependent while the K-corona is not. The FOV of the COR1 coronagraph ($1.4 - 4.0R_{\odot}$) offers a unique opportunity to explore the question of whether or not the radial dependence observed between the LASCO C1 and C2 FOVs is also seen in white light.

3.2 Data Preparation

For this study I used data from the COR1 coronagraphs on the twin STEREO spacecraft. I selected up to 10 images per day throughout 2008 and most of 2007, neglecting the first five days January of 2007 due to artifacts in the images. The images were inspected visually and images with missing blocks or large CMEs were removed from the data set. Table 3.2 shows the minimum, maximum and mean times between observations for the four data sets. I used the `secchi_prep` software to perform background subtraction and polarization calculation for the individual images. In order to compare measurements from the two spacecraft I rotated the images so that solar north was up and rescaled to a common plate scale throughout the course of each year-long dataset.

The 1024×1024 COR1 images were then split up into radial and latitudinal bins, as shown in figure 3.1. The intensities of individual pixels inside the superpixels shown in figure 3.1 were summed for each image in the data series, leaving a single intensity time series for each superpixel. The time series were then run through a

| Satellite | Year | # of Images | Min (Min) | Max (Days) | Mean (Hr) |
|-----------|------|-------------|-----------|------------|-----------|
| Ahead | 2007 | 3390 | 0.5 | 2.13 | 2.55 |
| | 2008 | 3477 | 5.0 | 1.17 | 2.52 |
| Behind | 2007 | 3383 | 10.0 | 4.00 | 2.59 |
| | 2008 | 3474 | 50.0 | 1.38 | 2.53 |

Table 3.2: Number of images and size of minimum, maximum and mean times between observations in time series.

routine that identifies and replaces extreme outliers by comparing each datum to the mean in a 10-point neighborhood around it, marking as extreme those that are more than 2.5 standard deviations outside the local mean. This was found to be a very good method for screening cosmic rays from the data without eliminating valid data points.

3.3 Period Measurement Methods

I used two methods to measure the spectra of the time series. Both methods have been used before to measure coronal rotation, though I made slight modifications to each to account for the angular drift of the STEREO spacecraft. In both methods I assumed a model periodic signal $F(t)$ is produced by the coronal material repeatedly circling the Sun and reappearing in the same spot. If the signal that would be measured by a coronagraph on the Earth-Sun line is given by $F_{\frac{\odot}{\oplus}}(\omega t)$, then the signal observed by the COR1 instruments should be $F_{COR1}(\delta_{\tau})$, where $\delta_{\tau}(t) = \frac{2\pi}{\tau}t \pm \Lambda_{COR1}(t)$ and $\tau = \frac{2\pi}{\omega}$. The plus sign is used for the behind satellite and the minus for the ahead, and $\Lambda_{COR1}(t)$ is the angular separation between the satellite and Earth.

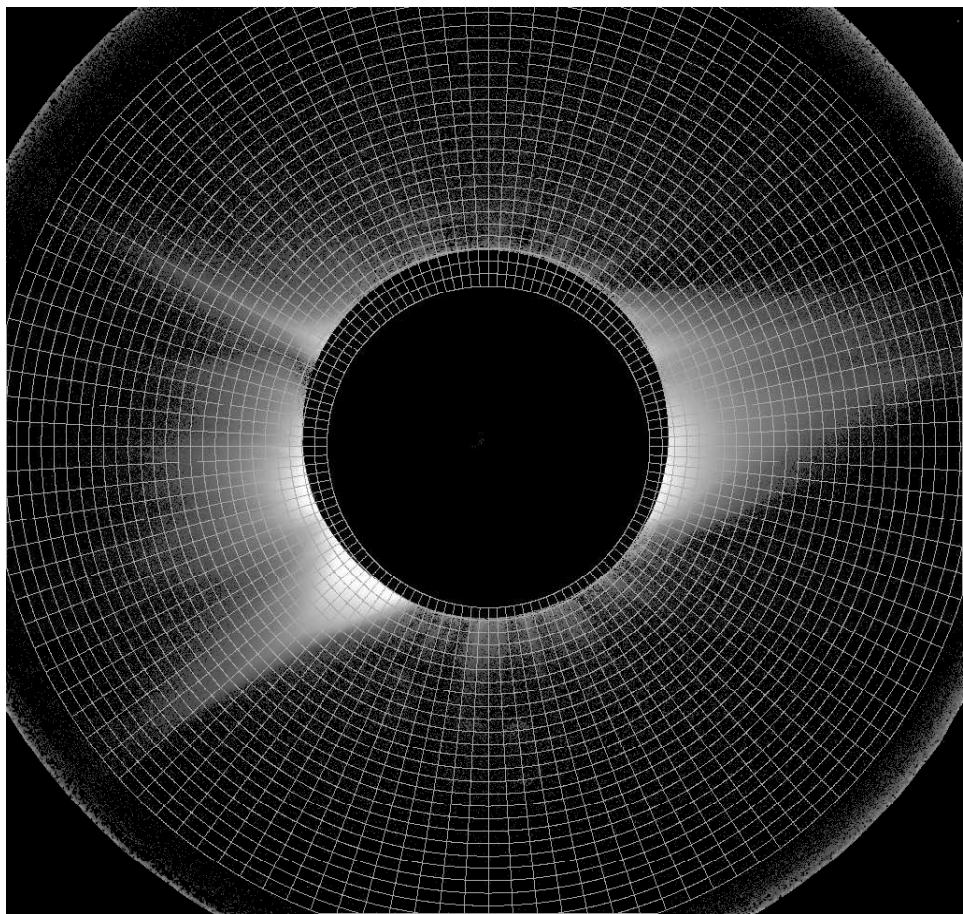


Figure 3.1: The distribution of polar superpixels over a COR1 Ahead image from 2008.

3.3.1 Autocorrelation

The first of the two measurement methods is a modified autocorrelation technique [31, 20, 75]. In traditional autocorrelation analysis the data series is interpolated at evenly spaced observation times and the following quantity is calculated:

$$P_A(L) = \frac{\sum_{i=1}^{N-L} (A_i - \bar{A})(A_{i+L} - \bar{A})}{\sum_{i=1}^N (A_i - \bar{A})^2} \quad (3.2)$$

The average rotation period over the time period used is then given by:

$$\tau = L_{max} \Delta t \quad (3.3)$$

where L_{max} is the lag at which $A(L)$ assumes a maximum and Δt is the elapsed time between interpolated observations.

In this study, however, the observed recurrence period is expected to change over the course of the time series, depending on the relative rotation speed of the observing satellite. The result obtained from the traditional autocorrelation is slightly inaccurate in two ways: the period at which the correlation curve peaks is artificially high (low) for the ahead (behind) spacecraft, and the peak is widened slightly by the averaging aspect of the autocorrelation calculation. The following algorithm is used to calculate the autocorrelation, corrected for the drift of the spacecraft:

1. Assume a particular Earth-synodic rotation period, τ
2. Calculate the argument $\delta_{\tau,i}$ of the periodic function $F(\delta_{\tau,i})$ at each observation time i
3. Interpolate the observed intensity $A(\delta_{\tau,i})$ at m evenly spaced δ_τ values

4. Calculate the autocorrelation coefficient $P_A(m)$ according to equation 3.2
5. Repeat for many values of τ

$P_A(m)$ should be greatest when τ is the correct Earth-synodic period.

3.3.2 Phase Dispersion Minimization

The second method used to measure the period in the COR1 time series is phase dispersion minimization (PDM) [85]. The basic algorithm used is as follows:

1. Assume a particular Earth-synodic rotation period, τ
2. Calculate the argument $\delta_{\tau,i}$ of the periodic function $F(\delta_{\tau,i})$ at each observation time i as above
3. Calculate $\Delta_{\tau,i} = \pm(\delta_{\tau,i} \bmod 2\pi)$, such that all values of $\Delta_{\tau,i}$ are between 0 and 2π .
4. Divide intensity values A_i into n bins based on their associated $\Delta_{\tau,i}$ values
5. Calculate the standard deviation $\sigma_{\tau,j}$ of the intensity values in each bin
6. Calculate the mean bin standard deviation $\bar{\sigma}_{\tau,j}$ and the standard deviation of the data series, σ ; the PDM statistic is $\Theta_\tau = \frac{\bar{\sigma}_\tau}{\sigma}$
7. Repeat for many values of τ

Θ_τ should assume a minimum at the correct Earth-synodic period. In a sense the PDM method minimizes the variation of the data points around a repeated curve of unknown length.

Figure 3.2 shows example spectra produced using the two methods. Spectra from the PDM method typically have more features, and have narrower peaks than

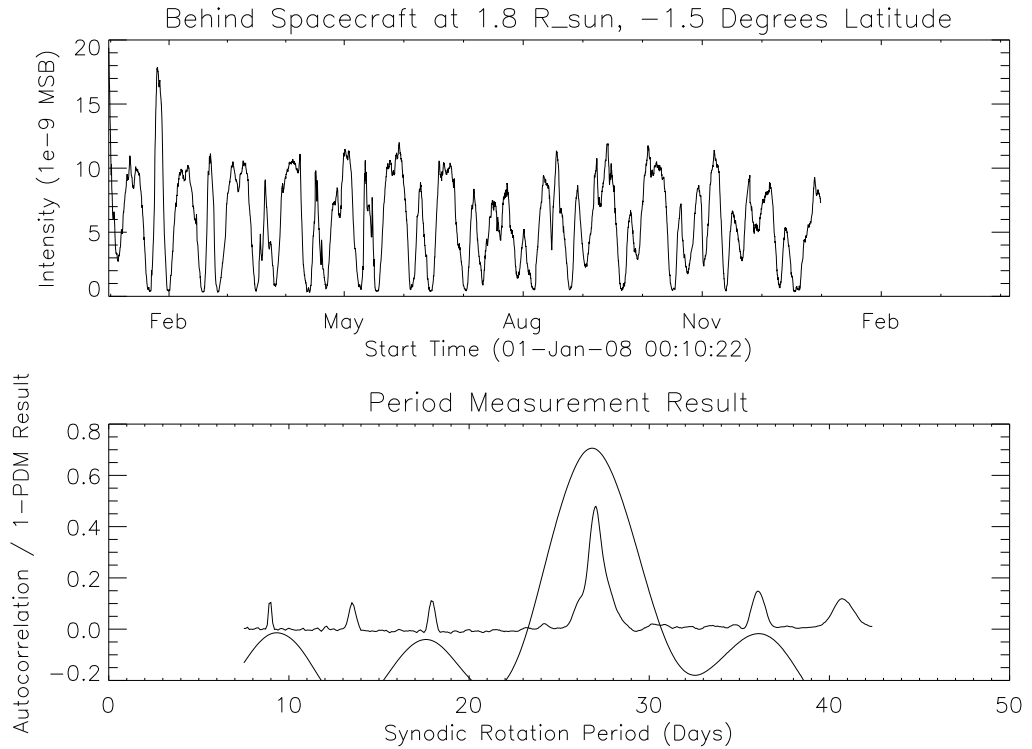


Figure 3.2: Top: Polarized brightness signal observed in 2008 from COR1-B at $1.8R_{\odot}$ and 1.5° S POS latitude. Bottom: The autocorrelation and PDM results obtained from the data series in the top panel. The PDM result has been subtracted from one so that for both methods likely periods are indicated by peaks. A perfectly periodic time series would produce an autocorrelation/PDM value of 1.0 at the appropriate period.

the autocorrelation curves; however, they also seem to be noisier. In order to interpret these spectra one must give some thought to the issue of spectral significance.

3.4 Evaluating Spectral Significance

Determining the significance of a maximum in our rotation spectra is a tricky problem for several reasons. For the PDM method, Stellingwerf suggests hypothesis testing [85]. Statistical hypothesis testing uses the distribution of spectral peaks

expected for a random (non-periodic) time series with similar noise characteristics [66]. Using the distribution it is possible to state a spectral peak's significance in terms of the probability that it was produced by random statistical fluctuations. There are several problems with applying such an approach in this work.

First, our periodic signal is not sinusoidal, it is a function of the longitudinal variation of the coronal electron density. In that case the observed spectrum represents a convolution of the rotation spectrum (which consists of peaks at any actual rotation frequencies of the data) with the Fourier spectrum of the underlying signal itself. Peaks may be found to be highly significant using the statistical test described above and yet still not represent true rotation frequencies in the corona [105, 86].

Second, the underlying coronal density signal is evolving in time. This evolution represents an additional contribution to the noise in our signal that is likely at least as important as the statistical noise in the CCD photon counts. The rate of this coronal evolution is highly variable in space and time and would be difficult to characterize.

Third, tests of statistical significance as described above rely on the statistical independence of individual data points. However, because of the optical thinness of the corona, each intensity value in our data series represent a sum of photons scattered from electrons all along the measuring pixel's LOS, rather than from a discrete point in space. Given the size of our superpixels, some of the material along the LOS at time step i is still in the FOV at time step $i + 1$; additionally, some of it is a distance, z , away from the POS and will reappear in the FOV when

it rotates through the POS and is seen at $-z$. This complicated interdependence of the intensity measurements is reflected in the fact that our time series always show high autocorrelation at small lags, indicating a high degree of dependence among measurements close in time.

Finally, the statistical distribution originally suggested to describe PDM spectra by Stellingwerf [85] does not accurately represent the PDM spectra [65, 16]. Linnell Nemec and Nemec [51] have suggested that the best way to deal with these spectra is to apply Fisher’s Method of Randomization (see [51] and references therein). In this method the measurement values are repeatedly scrambled, the analysis applied to the scrambled data, and a distribution is built up from the resulting spectra. However, this method does not account for any of the above problems and tends to indicate that every tiny bump in the spectrum is highly significant [86].

Given all of these difficulties it does not seem there is any hard and fast rule for accepting or rejecting peaks in these spectra; it is only possible to say whether our results are consistent or inconsistent with a given rotation scheme.

3.5 Period Search Results and Discussion

Figures 3.3 and 3.4 show the strength of the PDM and autocorrelation signals as a function of synodic rotation period and latitude for the 2007 time series at projected altitudes of $1.8R_{\odot}$, $2.2R_{\odot}$, $2.8R_{\odot}$ and $3.2R_{\odot}$. The results at each latitude are averages of the ahead and behind, east and west limb results. The image intensity shows the PDM result, while the contour lines show the strength of the autocorrelation signal for the same data. The dash-dot line represents the

rotation periods of the photosphere as measured by LaBonte and Howard [47]. The dispersion is only shown for latitudes between 60° and -60° ; outside that range the PDM curves are nearly flat. The results from the 2008 time series are in figures 3.5 and 3.6.

Figure 3.7 shows the results of fitting the autocorrelation peaks from $1.8R_\odot$ in each hemisphere in 2007 and 2008 to equation 3.1. Peaks were included in the fit only if the autocorrelation at that latitude reached a maximum greater than 0.2 between periods of 20 and 40 days, reached a minimum less than 0 between periods of 7.5 and 42, and the east- and west-limb maximum periods differed by no more than a day. There are also fits to the combined (north and south) dataset for those latitudes where measurements in both hemispheres were considered reliable. The fit coefficients are shown in table 3.3, along with the results of fitting the same data to a constant rotation rate A_c .

While the reduced chi-square values of the fits indicate that in most cases the fit to equation 3.1 was better than the rigid rotation fit, the reduced chi-square value for the constant fit of the combined 2008 dataset is better, for example, than the value for the combined 2007 fit to equation 3.1. Also, the fitted values of B for 2007 are all greater than one, in contrast to the photospheric results shown in table 3.1 (*i.e.* the fit is suggesting that the rotation rate initially *increases* with latitude), and the values of B for both hemispheres in 2008 are smaller than the uncertainty. There are several fits with reduced chi-square values less than one, which may indicate that the standard deviation of the rotation rate measurements at some or all latitudes overestimates the error in the measurement. From inspection of figure 3.7 there is

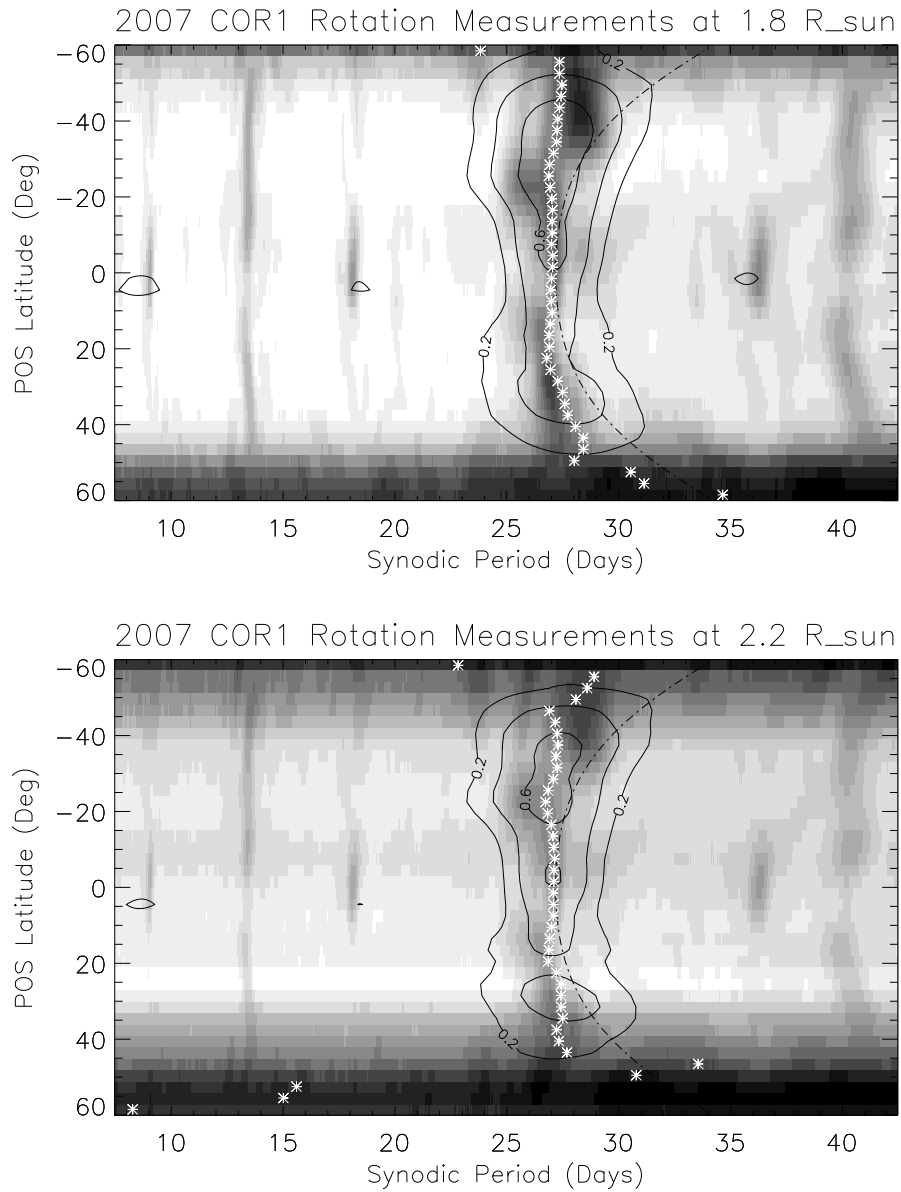


Figure 3.3: Coronal rotation measurements from 2007 at altitudes 1.8 and $2.2R_{\odot}$. The image intensity shows the PDM result as a function of latitude and rotation period. The contours show the intensity of the corresponding autocorrelation curves. The dashed line shows the photospheric rotation period as a function of latitude given by [47]. The asterisks show the positions of the autocorrelation maxima, averaged between spacecraft and limbs.

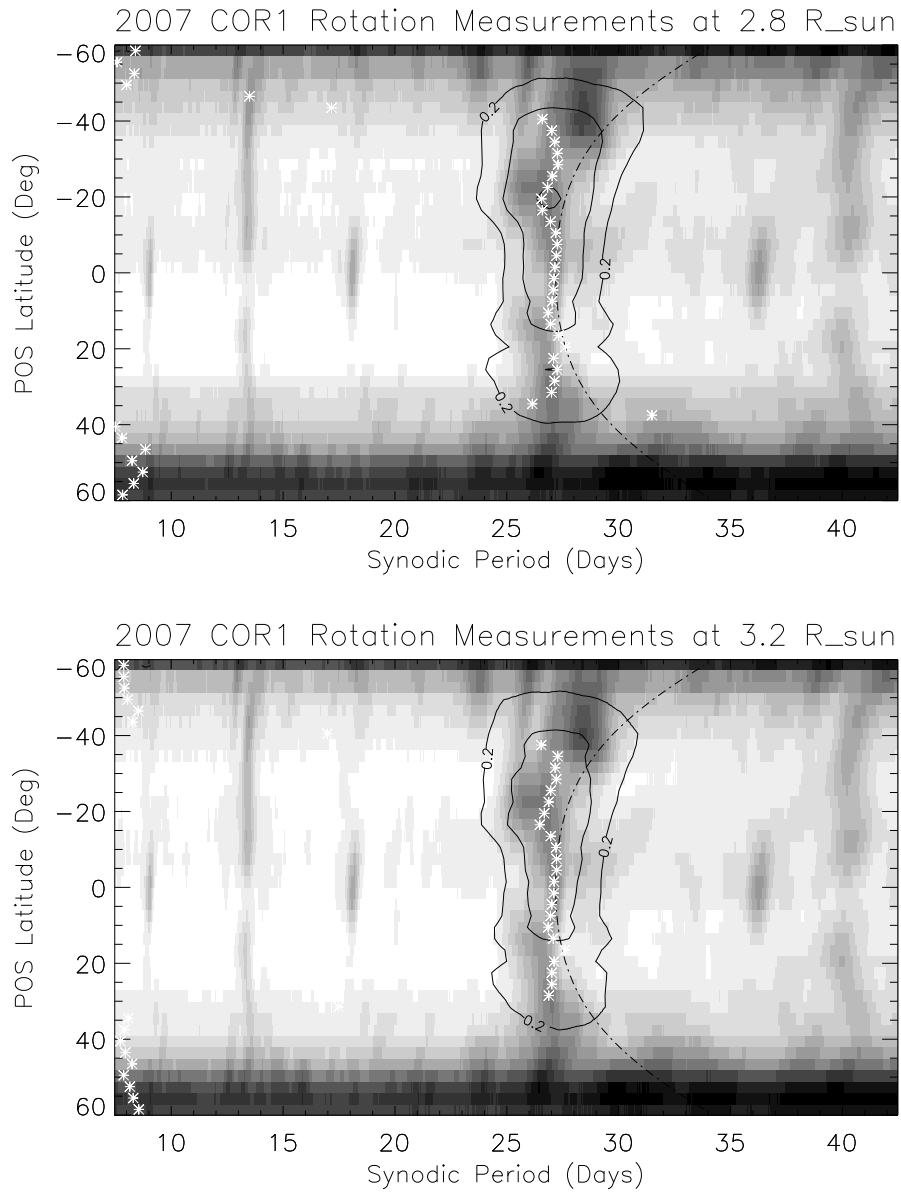


Figure 3.4: Coronal rotation measurements from 2007 at altitudes 2.8 and $3.2R_{\odot}$. The image intensity shows the PDM result as a function of latitude and rotation period. The contours show the intensity of the corresponding autocorrelation curves. The dashed line shows the photospheric rotation period as a function of latitude given by [47]. The asterisks show the positions of the autocorrelation maxima, averaged between spacecraft and limbs.

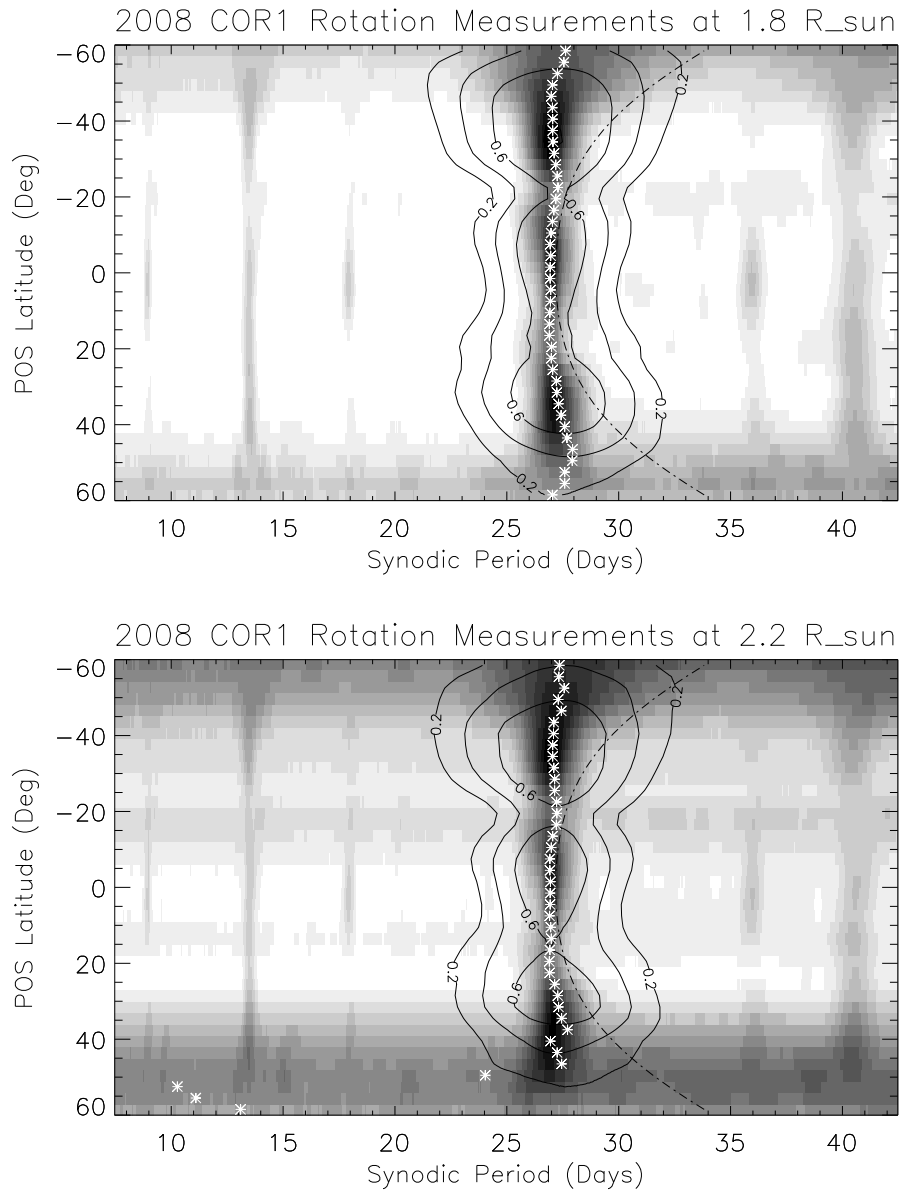


Figure 3.5: Coronal rotation measurements from 2008 at altitudes 1.8 and $2.2R_{\odot}$. The image intensity shows the PDM result as a function of latitude and rotation period. The contours show the intensity of the corresponding autocorrelation curves. The dashed line shows the photospheric rotation period as a function of latitude given by [47]. The asterisks show the positions of the autocorrelation maxima, averaged between spacecraft and limbs.

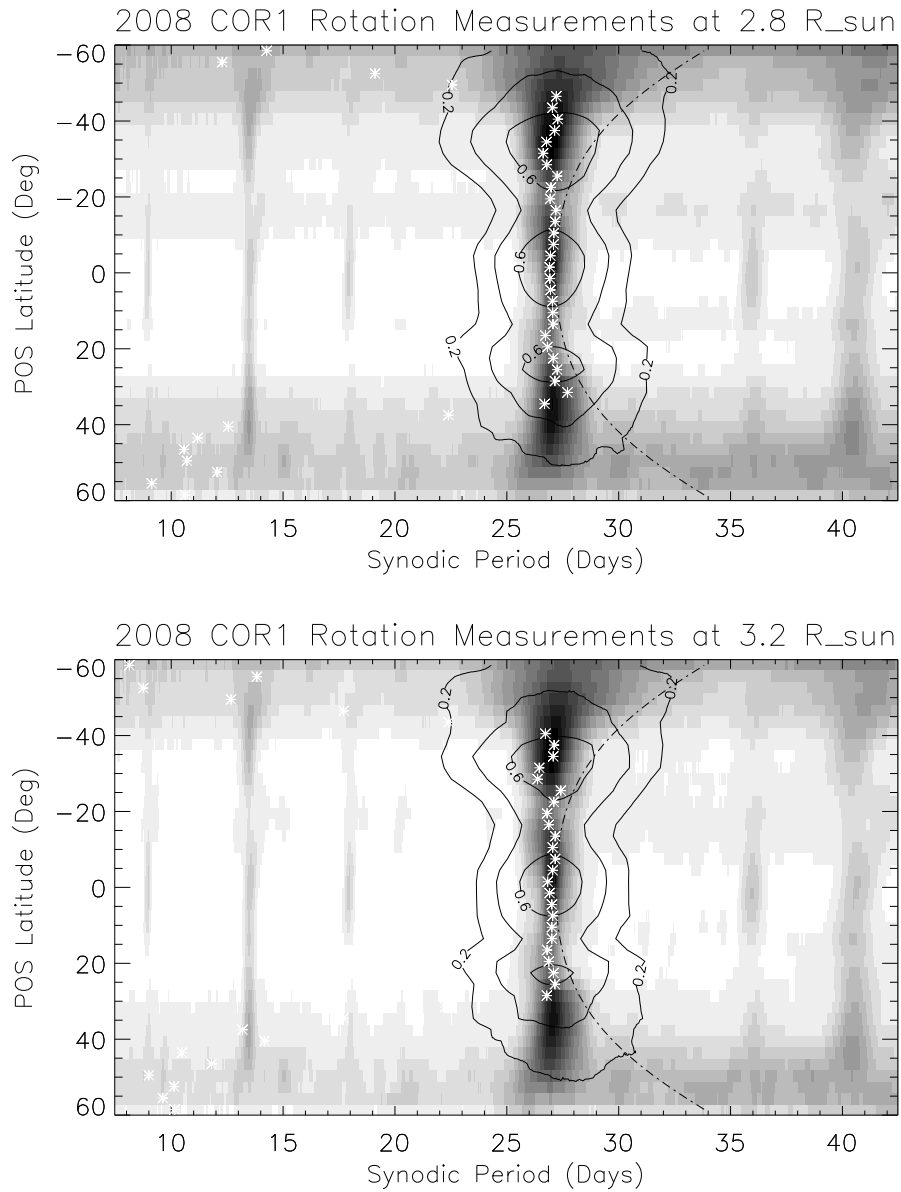


Figure 3.6: Coronal rotation measurements from 2008 at altitudes 2.8 and $3.2R_{\odot}$. The image intensity shows the PDM result as a function of latitude and rotation period. The contours show the intensity of the corresponding autocorrelation curves. The dashed line shows the photospheric rotation period as a function of latitude given by [47]. The asterisks show the positions of the autocorrelation maxima, averaged between spacecraft and limbs.

| Dataset | A | B | C | χ_ν | A_c | $\chi_{\nu A_c}$ |
|-------------|---------------|--------------|--------------|------------|-----------------|------------------|
| <i>2007</i> | | | | | | |
| North | 2.692 (0.004) | 0.26 (0.08) | -1.3 (0.2) | 0.64 | 2.6899 (0.0002) | 6.1 |
| South | 2.690 (0.004) | 0.12 (0.04) | -0.48 (0.08) | 2.2 | 2.6874 (0.0001) | 5.7 |
| Comb. | 2.691 (0.003) | 0.17 (0.03) | -0.70 (0.09) | 2.3 | 2.6883 (0.0001) | 5.4 |
| <i>2008</i> | | | | | | |
| North | 2.704 (0.006) | -0.03 (0.08) | -0.29 (0.17) | 0.78 | 2.6857 (0.0003) | 4.0 |
| South | 2.692 (0.006) | -0.03 (0.05) | -0.02 (0.09) | 0.64 | 2.6857 (0.0003) | 0.80 |
| Comb. | 2.702 (0.004) | -0.10 (0.05) | 0.00 (0.11) | 1.10 | 2.6863 (0.0002) | 2.1 |

Table 3.3: Results of fitting autocorrelation rotation measurements to equation 3.1, as well as fitting them to a constant A_c . Values for A , B , C and A_c are in units of μrads^{-1} and 1-sigma error estimates for the fit parameters are in parenthesis. χ_ν and $\chi_{\nu A_c}$ give the reduced chi-square values for the fits.

a notable difference between the two solar hemispheres in that the rotation in the southern hemisphere appears to be more rigid during both years. Inspection of figures 3.3 through 3.6 reveals several interesting features:

1. The coronal rotation in both years appears to be quite rigid in comparison to the photosphere, consistent with previous results. The equatorial synodic period, calculated by averaging the $1.8R_\odot$ peak periods at 1.5° S and N for both methods, both spacecraft, and both limbs is 27.06 ± 0.08 days in 2007 and 26.97 ± 0.10 days in 2008.
2. The results for higher altitudes are strikingly similar except that as the altitude increases the range of latitudes showing strong rotation signal decreases. There is little if any apparent radial gradient in the rotation rate.
3. Several peaks can be seen in addition to the main peak near 27 days. These

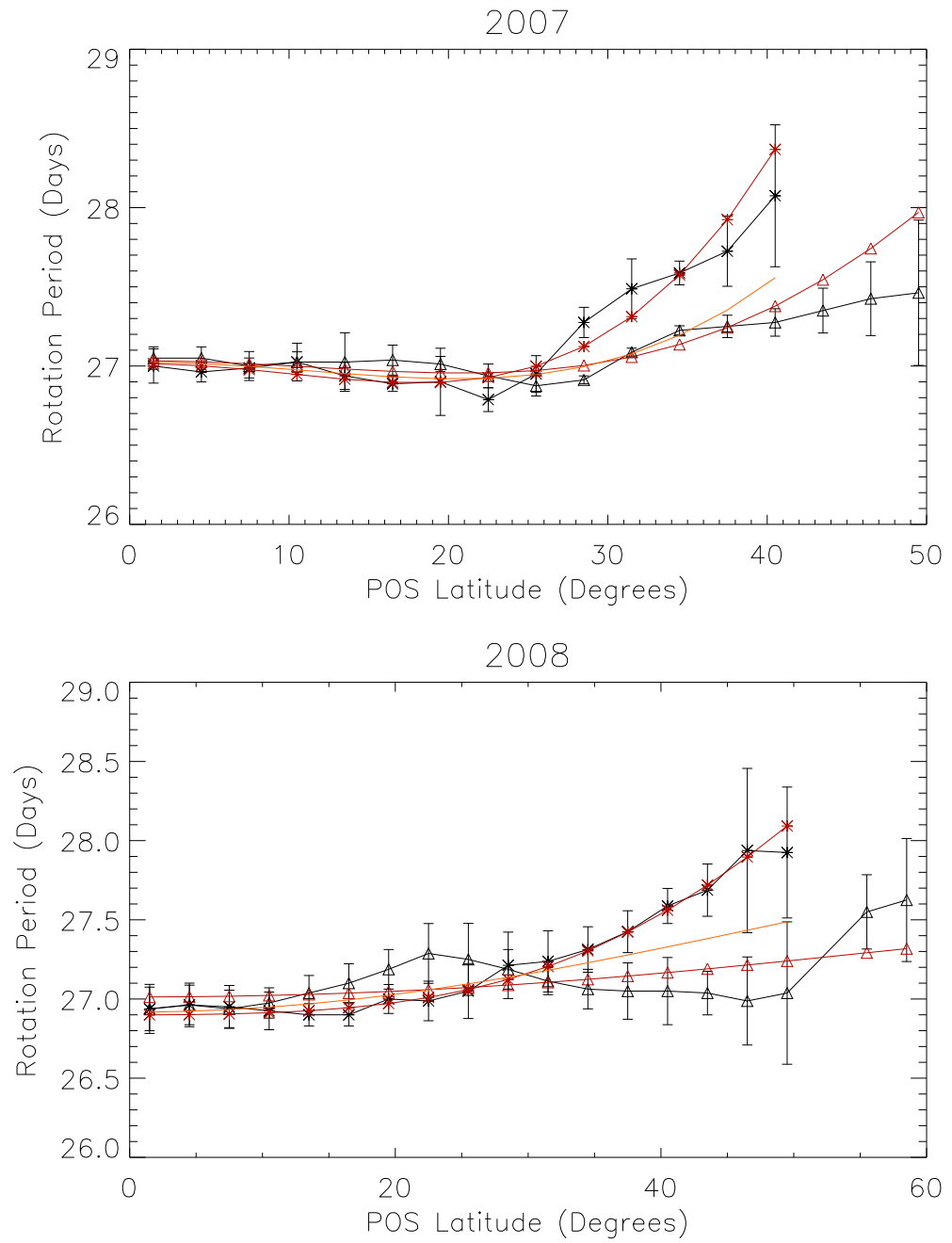


Figure 3.7: Results of fitting autocorrelation peaks to equation 3.1. Asterisks denote synodic rotation periods measured in the northern hemisphere while triangles denote measurements from the southern hemisphere. The red lines show the results of the fits to the individual hemisphere data, while the orange lines show the results of fitting data from both hemispheres simultaneously.

additional peaks appear to be harmonics of the main periodicity and its echoes. (See section 3.7).

4. There is apparent weakening of the rotation signal near 25° S and 15° N, seen using both measurement methods and in both years studied.

The use of the PDM method reveals many high-frequency peaks not usually seen in coronagraph studies using autocorrelation techniques. However, these peaks all appear to be harmonics of the main periodic component and its echoes, peaks due to the reappearance of a coronal feature after two, three, or four rotations. In figure 3.2 one can see the harmonic peaks are at approximately 9 ($\frac{27}{3}$) days, 13.5 ($\frac{27}{2}$) days, 18 ($\frac{54}{3}$) days, 36 ($\frac{108}{3}$) days, and 40.5 ($\frac{81}{2}$) days.

The cause of the apparent weakening of the rotation signal near 25° S and 15° N in both 2007 and 2008 is not really clear. Figure 3.8 shows the PDM spectra for several latitudes along the east limb in 2008. Along with the weakening there appears to be a widening of the main peak in the spectrum. Stenborg and coworkers conducted a PDM study on data from April-October 1996 [86, 87] and identified a trend at mid-latitudes towards the development of what they referred to as a pseudo-peak on the right side of the main peak, indicating that some material at these latitudes might be rotating slower than the rest. A similar trend is present in the PDM spectra in figure 3.8, along with a small shoulder on the left hand side of the main peak near the equator, not mentioned by Stenborg.

The significance of these pseudo-peaks is difficult to assess. It is very suggestive that they happen to be consistent with a differentially rotating component of the

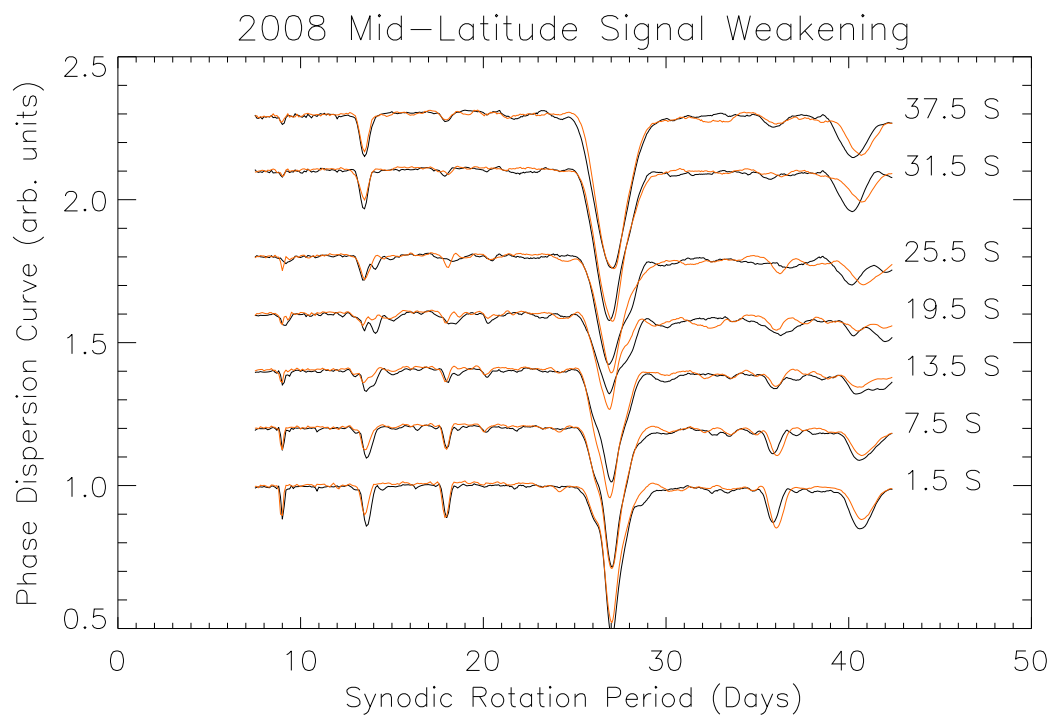


Figure 3.8: Detailed PDM spectra for several southern latitudes at $1.8R_{\odot}$ in 2008. The black curve shows the Ahead spacecraft results and the orange curve shows the Behind.

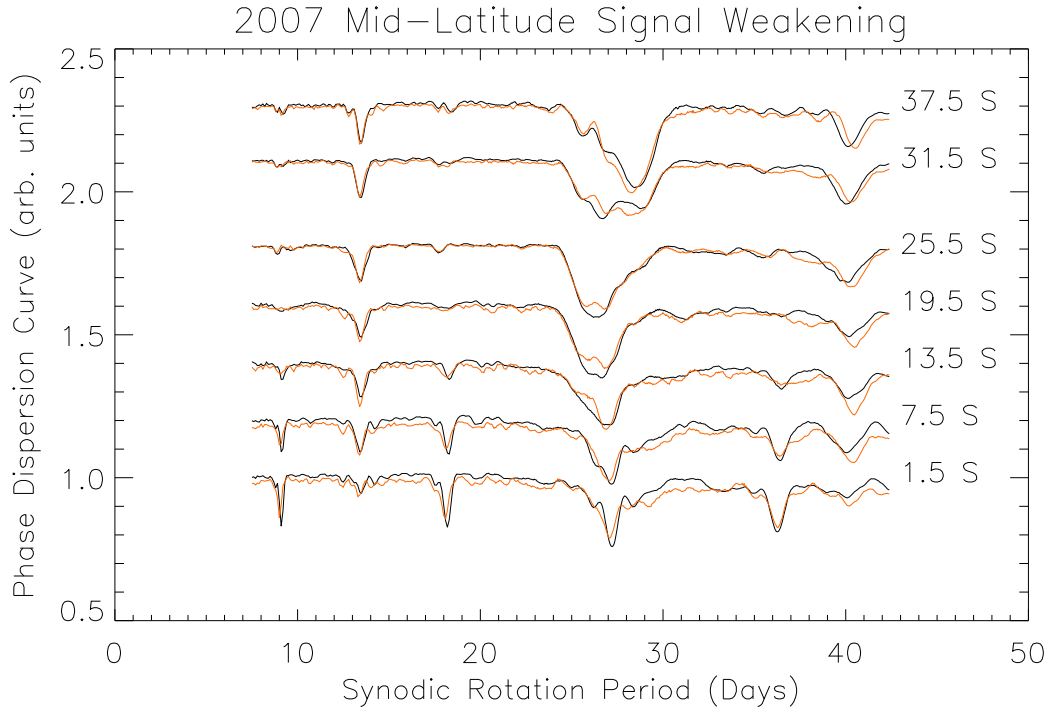


Figure 3.9: Detailed PDM spectra for several southern latitudes at $1.8R_{\odot}$ in 2007. The black curve shows the Ahead spacecraft results and the orange curve shows the Behind.

corona, and that they happen to have been seen at two successive solar minima. However, they are rather minor features in figure 3.8, and they could be explained by coronal evolution or a change in the rotation rate over the course of the year-long time series. Furthermore, a similar set of PDM spectra from 2007 show some spectral details that are not consistent with a differentially rotating component (see figure 3.9). None of these spectral details are seen in the autocorrelation analyses for either 2007 or 2008 (see figure 3.10).

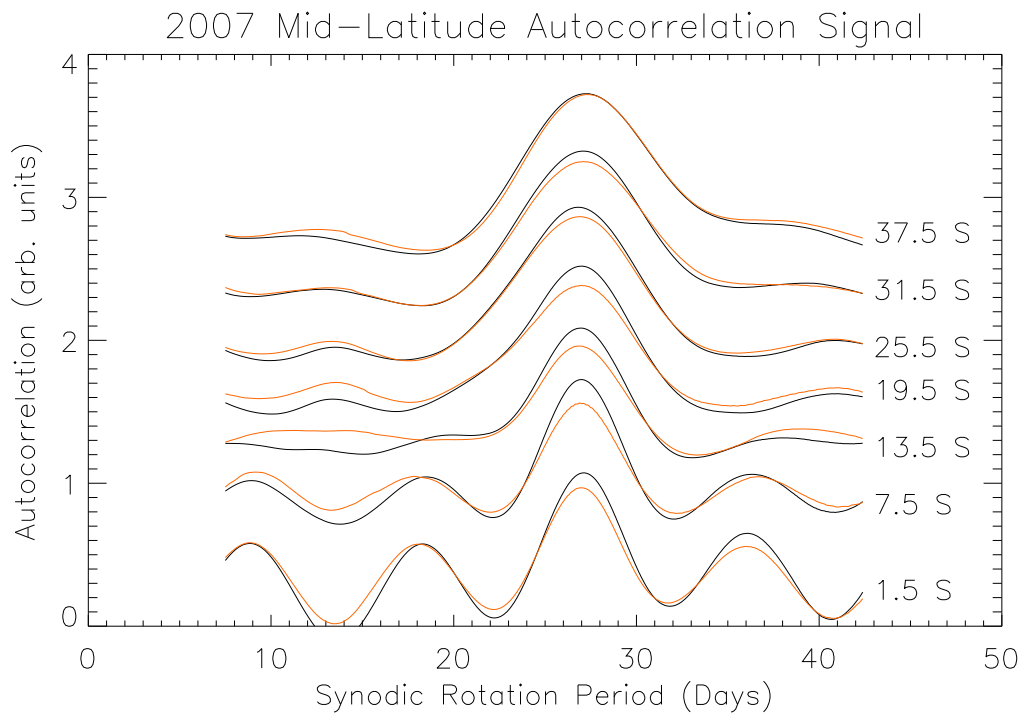
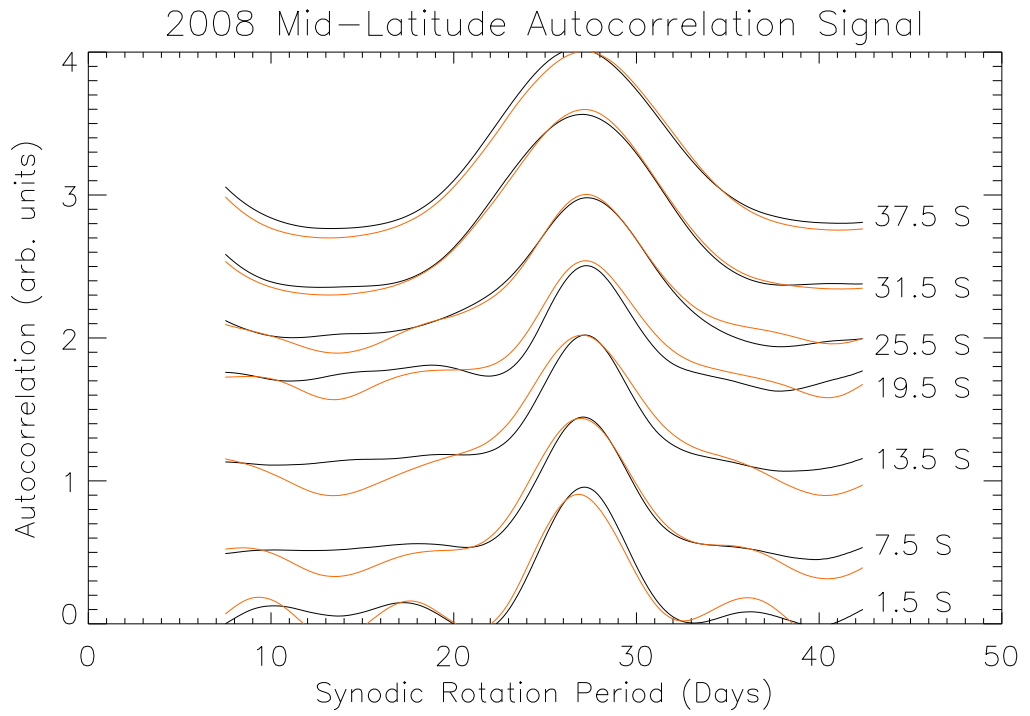


Figure 3.10: Autocorrelation results for several southern latitudes at $1.8R_{\odot}$ in 2007 and 2008. The black curve shows the Ahead spacecraft results and the orange curve shows the Behind.

3.6 Projection Effects and Secondary Periods

The observations above bring to mind two key questions from the literature. As mentioned earlier in this chapter, some researchers have noted that the apparent rigidity of the corona's rotation signal may be due to the projection of bright, low-latitude coronal features into the LOSs of high-latitude pixels. [50, 1]. The fact that the high-latitude signal tends to break down at larger radii could be consistent with this theory, or it could simply be a result of the fact that the COR1 signal is not as strong there. Also as discussed above, there has been a lot of interest in the literature in the possible co-existence of multiple rotation signals [105, 8, 86], which could be related to the weakening of the mid-latitude rotation signal. To investigate these issues, the following algorithm was used to remove the main periodic component from the time series:

1. Calculate the rotation spectrum using either autocorrelation or PDM
2. Find the most prominent frequency in the spectrum, τ_{main}
3. Calculate the argument $\delta_{main,i}$ of the periodic function $F(\delta_{main,i})$ at each observation time i
4. Calculate $\Delta_{main,i} = \pm(\delta_{main,i} \bmod 2\pi)$, such that all values of $\Delta_{main,i}$ are between 0 and 2π .
5. Divide intensity values A_i into m bins based on their associated $\Delta_{main,i}$ values
6. Calculate the average value of A_i in each bin (this gives the approximate average white-light coronal signal $C_{main}(\phi)$ as a function of longitude ϕ)
7. Interpolate the coronal signal corresponding to each point in the time series,

$$C_{main}(t)$$

8. Subtract $C_{main}(t)$ from $A(t)$ to get the residual time series $R(t)$
9. Calculate the rotation spectrum of $R(t)$

Figure 3.11 shows how the algorithm works for the example time series in figure 3.2.

If the rotation signal is dominated by the rotation rate of the most active latitude as suggested by [50], then $C_{main}(\phi)$ should be fairly uniform in each hemisphere over all latitudes with strong rotation signal. As can be seen in figure 3.12, the derived coronal signal exhibits a wide range of structures over the range of latitudes where good rotation signal was observed. One could argue that the signal seen at each latitude could be quite different and still result from a combination of projected and actual-latitude features; however, the inverse ‘C’ shape traced out between roughly 30°N , 215° longitude and 30°S , 250° longitude would be difficult to reproduce in such a situation.

As further evidence that the derived coronal signal is not greatly affected by projection effects, I compared figure 3.12 to the average coronal electron density for 2008 as calculated by Kramar et al. [46] using solar rotational tomography (SRT) [21, 22, 19], a technique that determines the full 3-dimensional coronal electron density from 2-dimensional images like those produced by COR1 (see appendix 6.4 for an explanation of the basic idea of SRT). The rotation tomography result, shown in figure 3.6, and the periodicity removal result are quite similar. The coronal hole near 300° carrington longitude is reproduced well, as are the regions of enhanced

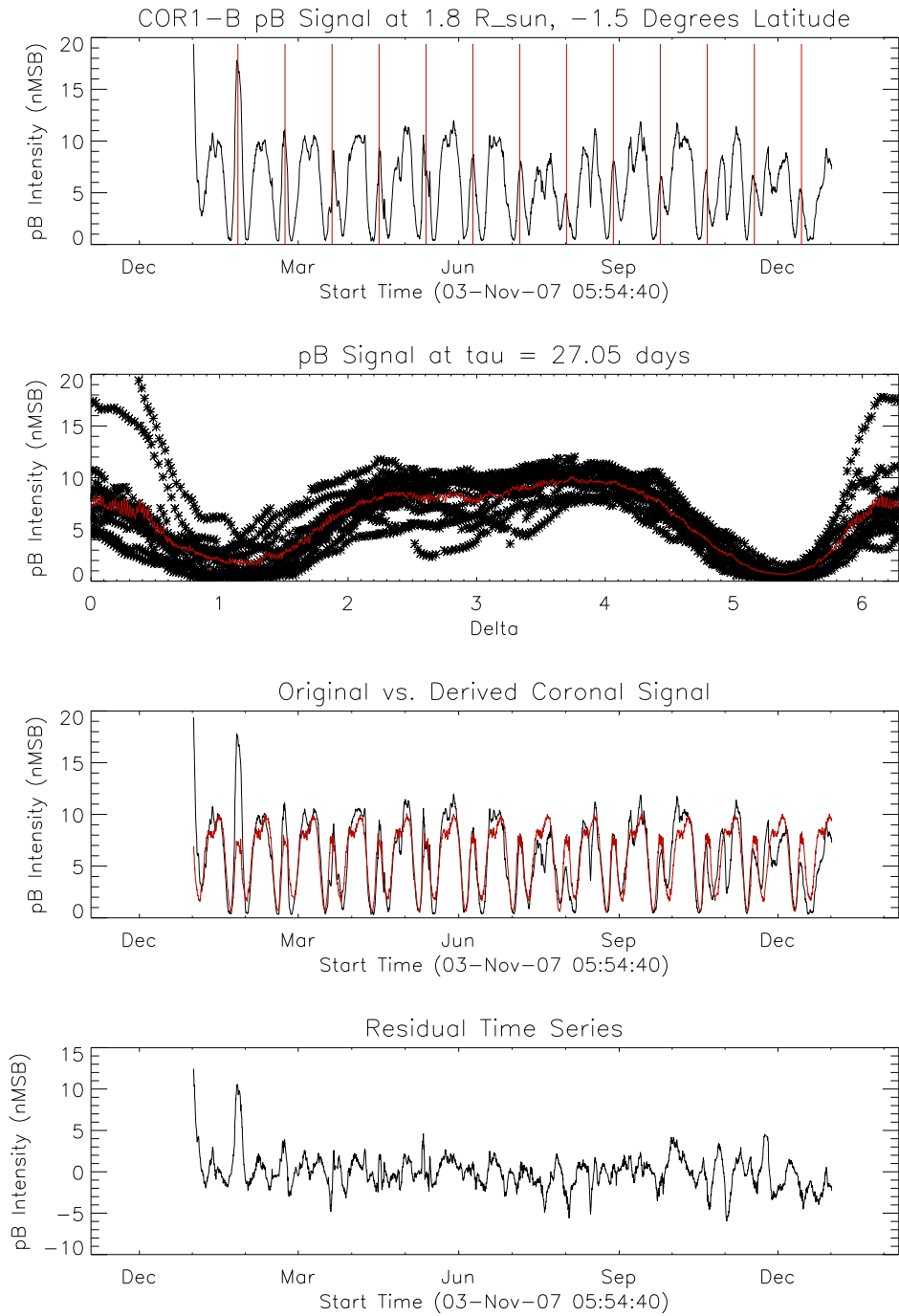


Figure 3.11: An example showing how the main periodic component is removed from a time series. The top panel shows the original data series, divided into segments containing one rotation each. These segments are then plotted on top of one another in panel two. The orange curve in panel two shows the average rotating signal, $C_{main}(\Delta)$. This curve has been interpolated at the value δ_i for each point in the original time series in panel three. Panel four shows the difference between the original time series and the interpolated values of C_{main} .

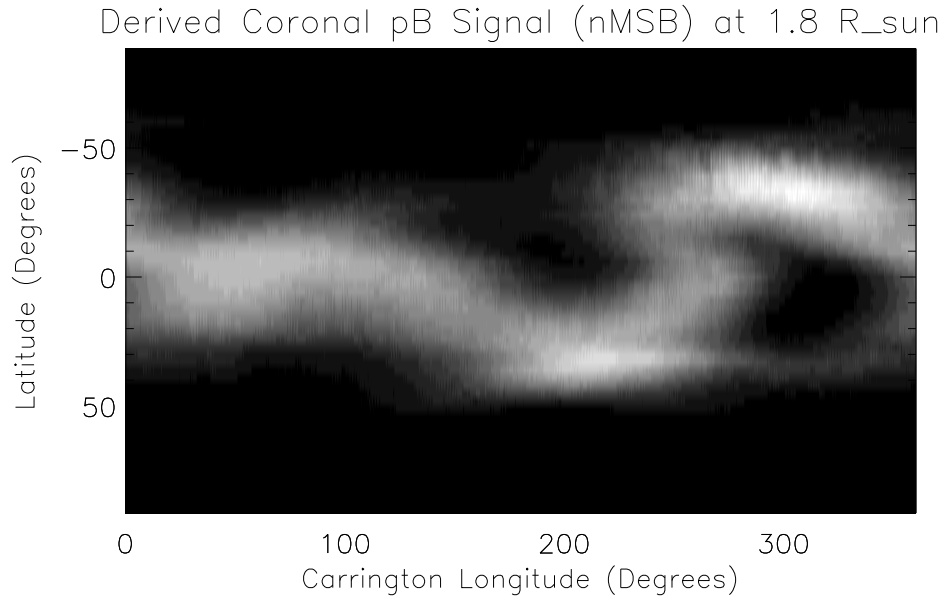


Figure 3.12: The coronal signal derived from calculating the main periodic component from every time series at $1.8R_{\odot}$ in 2008. Image brightness corresponds to the intensity of the pB signal scattered from the corresponding latitude and longitude in the corona towards the behind spacecraft. This quantity is expected to be approximately proportional to the coronal electron density shown in figure 3.6.

brightness near 210° and 290° longitude. This seems to indicate that the observed periodicity primarily reflects rotation over a range of latitudes.

As for the residual signals $R(t)$, the PDM results were uninteresting. There were no features in the PDM curves that could be clearly identified as a second periodic component. At some latitudes a double peak centered on the original main periodic component was observed, but with no objective measure of their significance it was difficult to evaluate whether the two peaks showed that a range of frequencies were present in the same latitude bin, whether the rotation rate had varied over the course of the year-long time series, or whether they were just the result of imperfect subtraction of the main component due to coronal evolution. The position of the

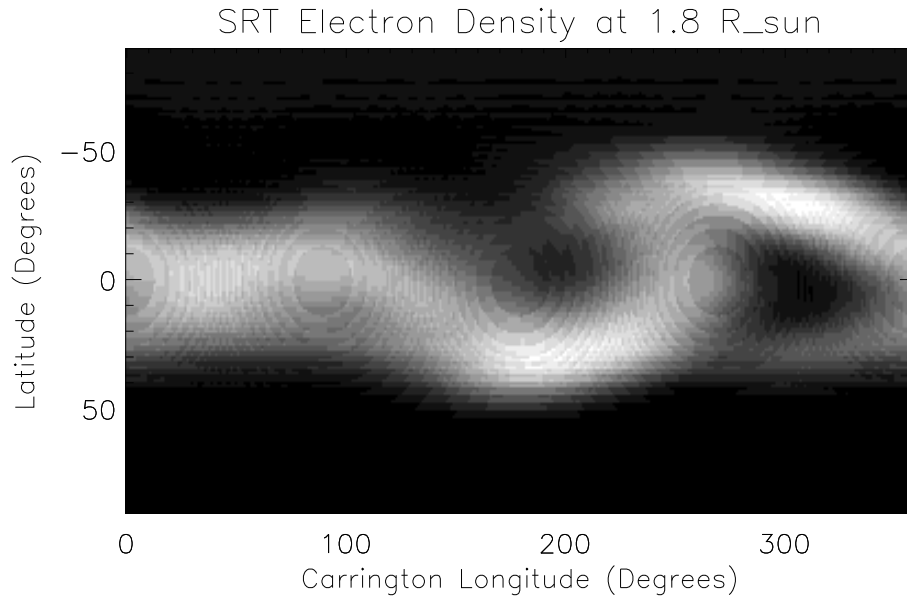


Figure 3.13: The average 2008 coronal electron density at $1.8R_{\odot}$ as estimated using solar rotational tomography (SRT).

two peaks relative to the component removed did not seem to have any latitudinal or radial dependence.

3.7 Conclusions

To summarize, the main conclusions from this chapter are as follows:

1. Coronal rotation during 2007 and 2008 is remarkably rigid compared to the photospheric rotation, with synodic rotation periods of 27.06 ± 0.08 days in 2007 and 26.97 ± 0.10 days in 2008.
2. The rotation rate does not show a radial dependence in the COR1 FOV.
3. Based on the coronal signal derived from the time series data, the observed rigidity of the rotation rate is not the result of projection of low-latitude features into higher latitudes.

4. The COR1 data do not indicate the presence of additional periodic components, though they cannot be entirely ruled out.

Chapter 4

Rotation Rates from Multi-Spacecraft Observations

As is discussed in chapter 2, the two spacecraft of the STEREO mission offer an opportunity to investigate many existing solar physics problems in new ways; coronal rotation is one such problem. While in chapter 3 I presented measurements of coronal rotation using the two COR1 coronagraphs separately, in this chapter I measure the coronal rotation rate using them in combination. The combination of data from the Ahead and Behind spacecraft makes it possible to study features with lifetimes much shorter than those that can be observed with a single coronagraph, allowing the question of rotational rigidity of short-lived coronal features to be addressed.

4.1 Introduction: Opportunities from Multi-Spacecraft Observations

Most rotation measurements using coronagraph data have until now been performed by measuring the intensity at a particular point in the POS over a period of several solar rotations and searching for periodicity in the resulting time series, by for example using autocorrelation. This method *selectively observes features that persist for a minimum of one solar rotation*. Inhester *et al.* [38] and a later related study by Stenborg *et al.* [86] were able to reduce the minimum persistence time to half a solar rotation by comparing features on opposite sides of the solar image. Beyond this the selective observation of long-lived features is an unavoidable limitation of single-viewpoint coronagraph studies.

The reason this limitation is troubling is that photospheric magnetic observations have revealed different rotation rates from studies that looked for repetition after a complete rotation (long time lag studies) than from studies that looked for repetition after time lags on the order of a few days (short time lag studies) [98, 78, 76]. Wang and coworkers were able to create a model of photospheric magnetic flux transport (based on earlier work by Leighton [48]) that reproduced some of the observational differences between short and long time lag studies [98, 101, 69]. The model explains the evolution of the photospheric magnetic field as being dominated by the eruption and subsequent transport of magnetic flux from the sunspot latitudes. Flux elements from the sunspot latitudes are slowly transported poleward by meridional flow, while undergoing differential rotation and a random walk over the solar surface due to supergranular convection. Collectively these small flux elements act like large-scale, long-lived magnetic patterns that rotate rigidly. Snodgrass [78] compared these large-scale patterns to the cloud of smoke coming out of a factory smokestack: the cloud appears stationary even though individual particles within it are constantly moving away from the smokestack.

There were, however, problems with the smokestack model, one of them being that the model could not account for the differential rotation of so-called mesoscale features at time lags on the order of a solar rotation observed by Snodgrass [78]. In a later paper, Snodgrass and Smith [80] identified the mesoscale features as differentially rotating clumps of smaller flux components, the mesoscale flux elements having lifetimes on the order of a solar rotation and the smaller flux elements having lifetimes of approximately one day. They were able to explain the differences

between long and short time lag studies as being caused in part by procedural differences in the correlation computation. They conclude that it is possible to measure differential rotation in photospheric magnetograms at time lags on the order of a solar rotation if sufficient longitudinal resolution is available and if a sufficiently long dataset exists and the observer averages correlation functions from several image pairings.

To what extent the differential rotation of short-lived and/or small-scale features persists into the corona is unknown, because until now it has been impossible to make short time lag measurements of coronal rotation. UV emission line instruments can be used in a similar manner to photospheric magnetograms, but they suffer from the limitation that coronal emission originates over a large range of heights. Correlating longitudinal strips from one image to the next, as is done with magnetograms, implicitly assumes that the emission in that strip all originates at the same height above the solar surface. Tracer methods, where bright features are traced through a series of images, require that the height of the feature be estimated [12, 62].

Coronagraph measurements to the present have been limited to time lags longer than one-half solar rotation. With the two STEREO spacecraft, it is now possible to compare coronagraph observations of the same coronal features after only a fraction of a solar rotation. Instead of autocorrelation of a time series, I can cross-correlate corresponding time series from satellites that are just a few degrees apart, thus observing shorter-lived coronal features. Because the separation between the spacecraft increases over the course of the mission, the time lag at which I am

studying the rotation rate gradually increases.

The rest of this chapter is organized as follows. Section 4.2 briefly describes the Ahead and Behind COR1 time series used throughout this chapter, primarily focusing on the differences between the time series in this chapter and those in chapter 3. Section 4.3 describes how the coronal rotation rate is measured by cross-correlating the two COR1 coronagraphs, with details of the cross-correlation calculation deferred to appendix B. In section 4.4 I show the results of simulations used to test the accuracy of the dual-spacecraft methods used here. Results of applying the method to the actual Ahead/Behind time series pairs are presented in section 4.5. Section 4.6 describes the separation and analysis of time series features of large and small scale sizes, and sections 4.7 and 4.8 contain discussion and conclusions.

4.2 Data

I chose to study the period from 1 March - 31 June 2007 because of the relatively small angular separation between the two STEREO satellites, plotted in figure 4.1. When the longitudinal separation is too small the temporal resolution is too small to adequately distinguish between, for example, a 27.0 day rotation period and a 27.1 day rotation period. On the other hand, at the end of June 2007 the spacecraft separation had increased to 15.87° , which would take approximately 1.19 days to traverse at a 27.0 day rotation period. This data set allows us to study features having lifetimes below the one-day value measured by Snodgrass and Smith [80] for the finest-scale photospheric magnetic features.

The time series used in this chapter have been prepared in a similar manner

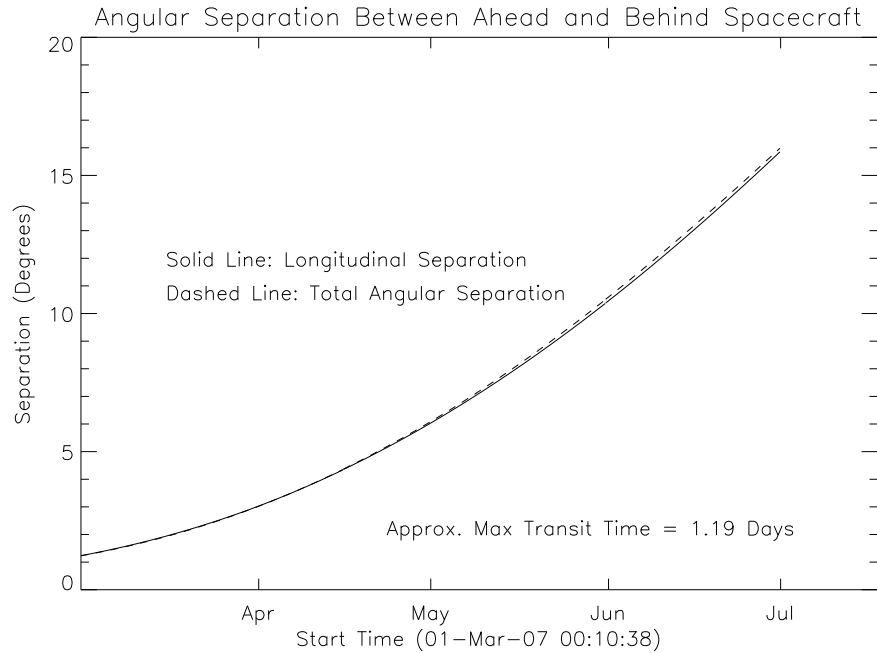


Figure 4.1: The angular separation between the Ahead and Behind spacecraft during the time period studied. The solid line shows the longitudinal separation, while the dashed line shows the total angular separation. The max transit time is the time required for a corona rotating once every 27 days to traverse the angular separation of the satellites at the end of the time series.

to that in chapter 3: they were rescaled to a common platescale and rotated so that solar north is at the top of all the images. However, because the separation between the spacecraft is small, I need higher temporal resolution than in chapter 3 to achieve reasonable resolution in the period measurement. For that reason I use all available COR1 images from both satellites for the time period studied.

Figure 4.2 shows a sample time series for each spacecraft. (Throughout this chapter I will plot Ahead time series in black and Behind time series in red.) Because the number of images in the time series is greatly increased from the previous chapter, no attempt was made to remove CMEs from the data set. I did, however, remove many images that were corrupted by an onboard software problem between

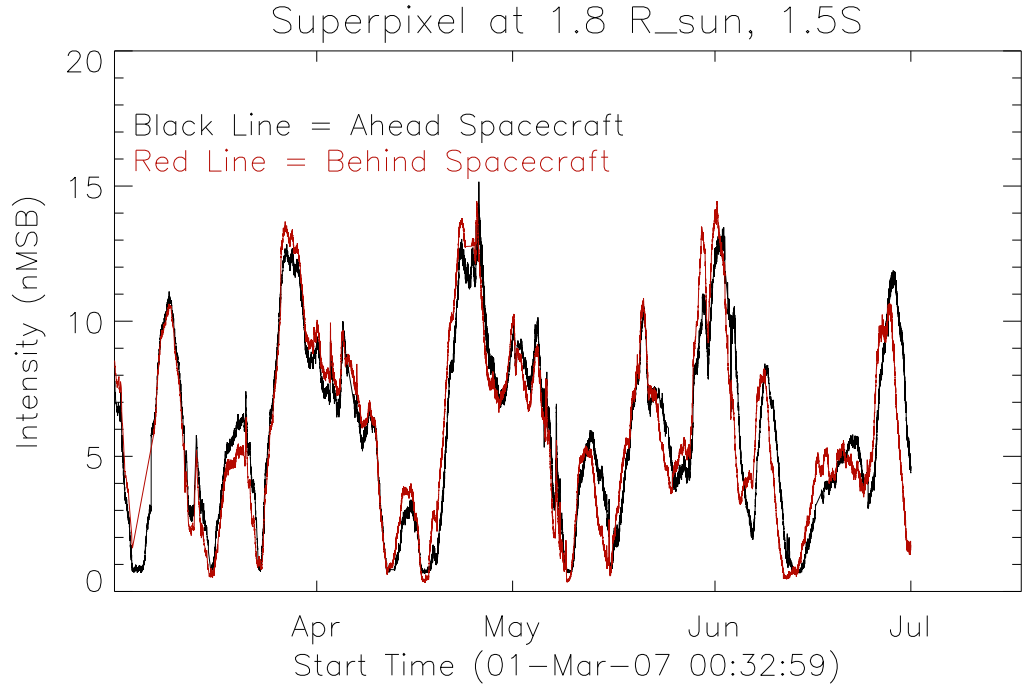


Figure 4.2: Intensity time series from $1.8 R_{sun}$, $1.5 S$ POS latitude.

March and May of 2007. Table 4.1 shows the number of images used from each spacecraft, and minimum, maximum and mean data gaps. The large data gap in the Behind series can be seen in figure 4.2 near the beginning of the time series. Note that the nominal cadence of the COR1 coronagraphs is five minutes during some parts of the time periods studied and ten minutes during others.

4.3 Dual-Spacecraft Method

If the two STEREO satellites were stationary, and the time series were evenly sampled, then the cross-correlation would be given by:

$$P_{AB}(L) = \frac{\sum_{i=1}^{N-L} (B_{i+L} - \bar{B})(A_i - \bar{A})}{\sqrt{\sum_{i=1}^N (A_i - \bar{A})^2 \sum_{i=1}^N (B_i - \bar{B})^2}} \quad (4.1)$$

| Satellite | # of Images | Min Gap (Min) | Max Gap (Days) | Mean Spacing (Min) |
|-----------|-------------|------------------|-------------------|-----------------------|
| Ahead | 19,735 | 4.987 | 0.903 | 8.900 |
| Behind | 22,349 | 4.986 | 3.236 | 7.860 |

Table 4.1: Number of images and size of minimum, maximum and mean times between observations in the Ahead and Behind COR1 time series.

The sidereal rotation period would then be given by:

$$\tau_{sidereal} = \frac{2\pi L_{max} \Delta t}{\Delta\Theta} \quad (4.2)$$

where Δt is the time between observations, $\Delta\Theta$ is the angular separation between the two spacecraft, and L_{max} is the value of L at which $P_{AB}(L)$ assumes a maximum.

However, the increasing longitudinal separation of the STEREO spacecraft distorts direct cross-correlation of time series. From examination of figure 4.2 the time lag giving optimal alignment of the Ahead and Behind time series clearly grows over the course of the time period studied.

Two methods are used to approximate the cross-correlation, similar to those used for autocorrelation of unevenly spaced data (see [63] and references therein). In the first method I interpolate both series at times corresponding to smooth rotation of the POS. The second method does not require interpolation of the time series, but compares measurement pairs that represent very similar (but not equal) rotation period values. These two methods are described in greater detail in appendix B.

4.4 Simulated Results

In order to test the feasibility of detecting the rotation signal, I generated artificial time series, one highly idealized and one slightly more realistic, to study how well I was able to reproduce the correct rotation period using the measurements available. Figure 4.3 shows an artificial pair of time series, generated using the observation times and angular separations of the real Ahead and Behind times series, and the results of both the single- and dual-spacecraft analyses of these idealized time series. The artificial time series are composed of two half-wave sine curves with identical periods of 27 days, a relative amplitude of 0.4:1, and a phase difference of π . A small, normally distributed random noise component with a standard deviation of 0.005 relative to the amplitude of the larger half-wave is added to the combined signal.

The cross-correlation peaks in figure 4.3 are clearly much wider than the single-spacecraft autocorrelation peaks, though the peaks occur very near the expected value of 27.0 days. The excess width can be most easily understood in terms of equation 4.2. The cross-correlation is calculated by shifting time series \vec{B} with respect to \vec{A} and multiplying for a range of lags L . The range of values of L over which $P_{AB}(L)$ is high is completely determined by the characteristic scales of features in the time series \vec{A} and \vec{B} , so in order to decrease the range over which τ is high (*i.e.* narrow the cross-correlation peak), I simply have to increase $\Delta\Theta$. Equations 4.1 and 4.2 are equivalent to equations 3.2 and 3.3 when \vec{A} is replaced by \vec{B} and $\Delta\Theta$ by 2π , hence the peak is narrower in the autocorrelation calculations.

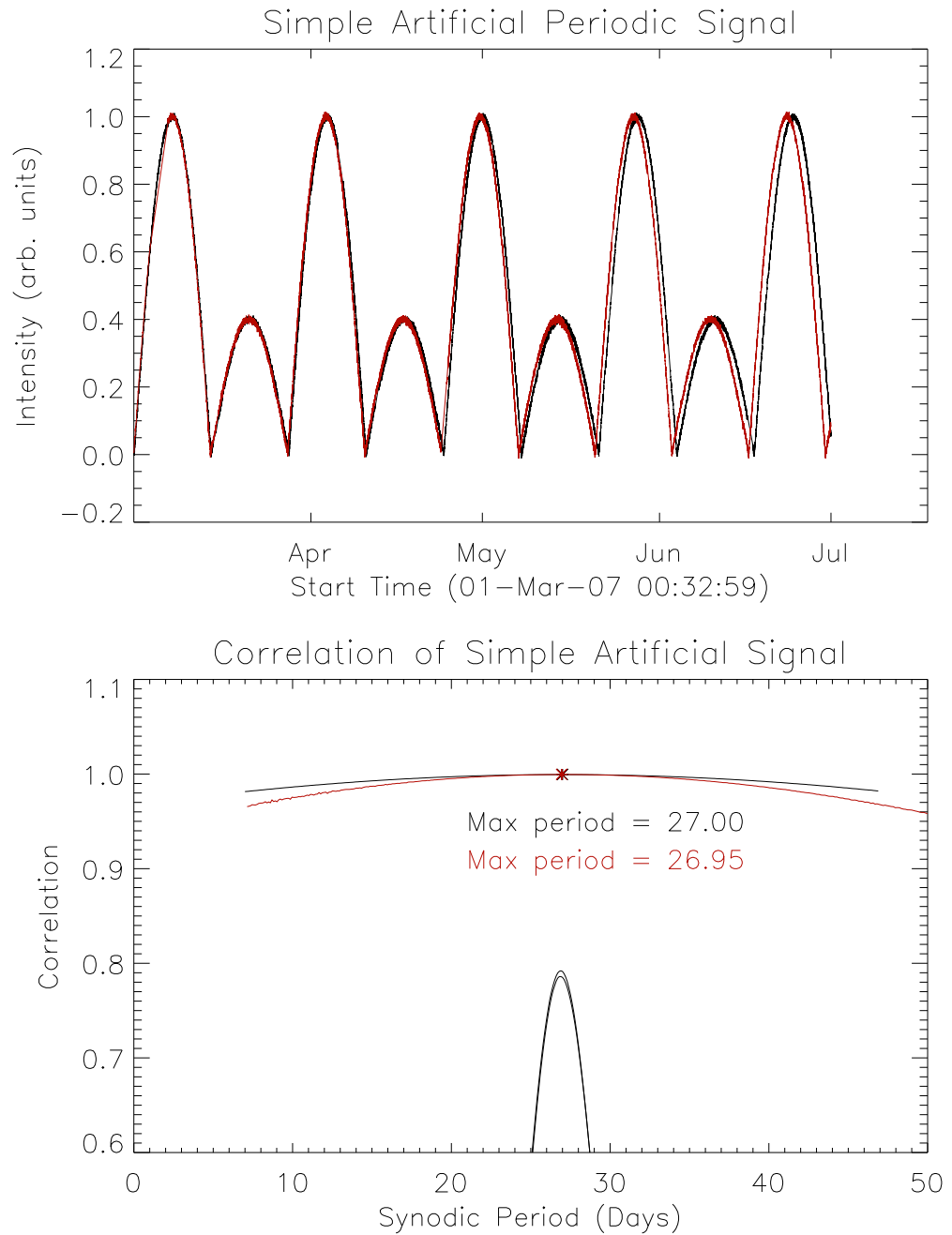


Figure 4.3: The top panel shows an artificial Ahead/Behind time series pair. The bottom panel shows the cross-correlation functions for these two artificial time series. The two cross-correlation curves that peak near 1.0 result from the two dual-spacecraft analyses, while the narrower peaks below result from the single-spacecraft autocorrelation analysis used in the previous chapter.

In addition to the simple periodic curves in figure 4.3, I also created somewhat more realistic time series. These series start out with the same basic structure as the series in figure 4.3. This time, however, I construct a two dimensional surface, in which the first dimension gives the longitudinal structure of the coronal intensity (initialized to a pair of offset rectified sine waves with a relative magnitude of 0.4:1 and a relative phase of π) and the second dimension represents time. For each time step I randomly select 60 percent of the 500 longitudinal points and add a randomly distributed number with a standard deviation of 0.035 relative to the larger sine curve. (The model parameters were chosen to generate curves that somewhat resembled the curves of figure 4.2, though the evolution from one solar rotation to the next is not as pronounced as in the real data.) Then the longitudinal strip is interpolated between these points, in order to produce a smoother time series, similar to the actual intensity curves. The longitudinal structure at each time step starts not from the longitudinal configuration of the time step before it, but from the same basic two-sine configuration. If the former method were used then as time went on the longitudinal structure would evolve towards a random state, which is in fact the opposite of what the corona does in 2007.

Once the two-dimensional surface is constructed, the time series of both satellites can be interpolated from the satellite positions and observation times. Figure 4.4 shows an example of these complex artificial time series and the average result when the correlation analysis is applied to several realizations of the randomized two-dimensional surface. The location of the maximum peak varies around the expected value of 27.0; for 20 sets of artificial time series the mean and standard

deviation are 26.79 and 0.02 using the first correlation calculation method and 26.87 and 0.06 using the second. It is interesting that the estimated value for the rotation period is systematically lower than the expected value. This effect is dependent on the percentage of the longitudinal points that are altered in each time step (*i.e.* the independence of the data points). I will return to this issue in section 4.7.

4.5 Results

Figure 4.5 shows the results of applying the two cross-correlation calculation methods to a pair of time series at $1.8R_{\odot}$ at several latitudes in the southeastern image quadrant; the result of the first (second) cross-correlation method is in black (red). The cross-correlation curves have similar widths to what was seen in the artificial time series, but the differences between the two estimated cross-correlation curves are greater than in the artificial cases described above and the cross-correlation curves peak at period values much lower than those seen in chapter 3. The measured values are not consistent with previous measurements of rotation in either the corona or the photosphere.

Clearly the results were not as good as expected based on the artificial time series shown above. One difference between the artificial and actual time series that may help explain this discrepancy is the presence of impulsive events like CMEs, whose longitudinal extent is sufficient that they may show up in the same pixel of both spacecraft at the same or nearly the same time, introducing a spurious correlation at small rotation periods. Figure 4.6 shows an example of a series of relatively small events near the equator on the eastern limb, seen in the time series

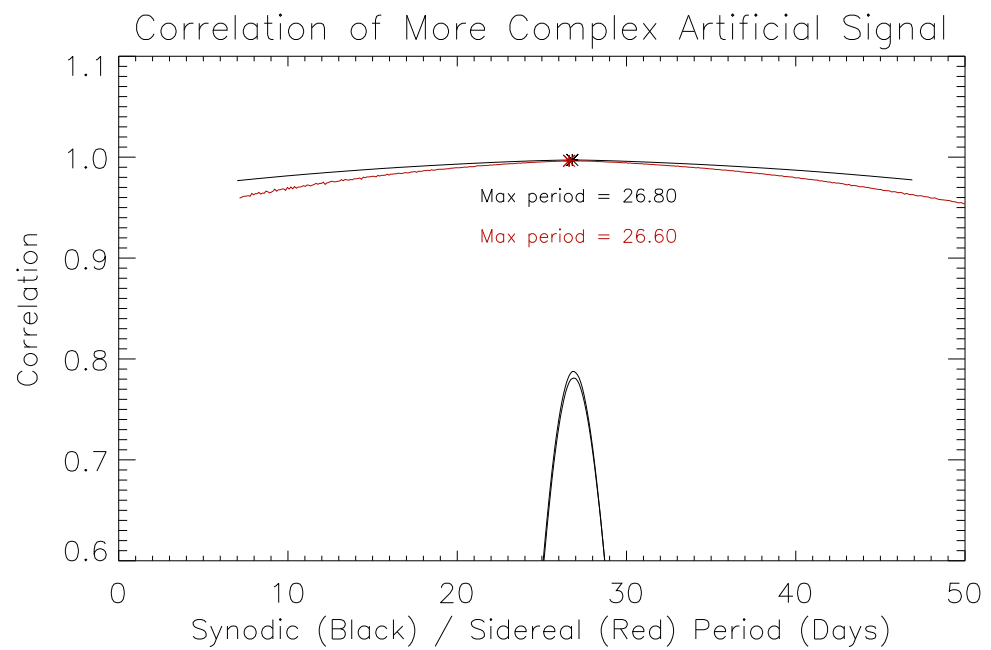
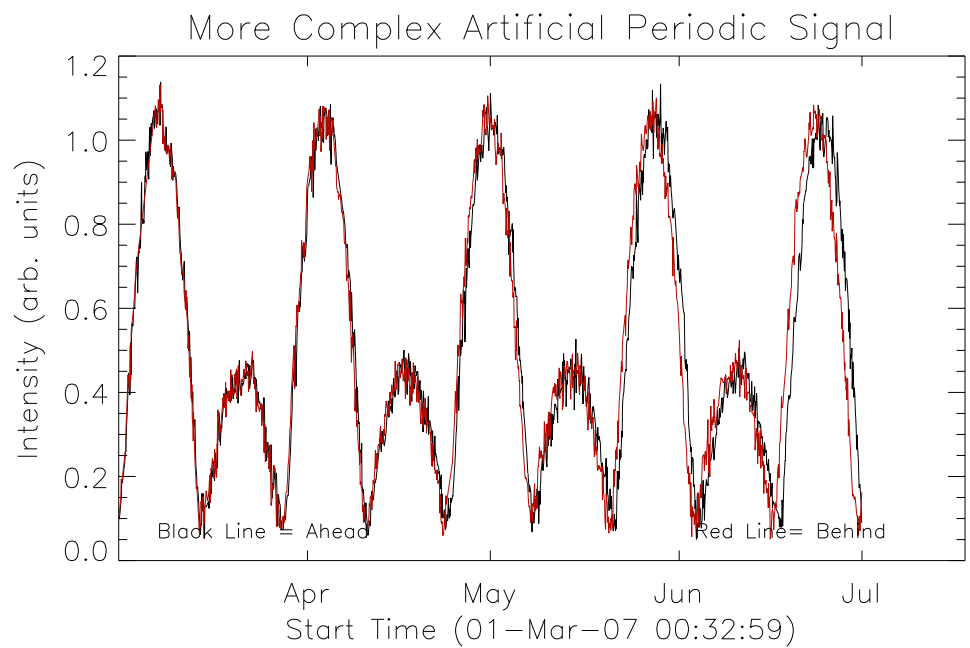


Figure 4.4: Top: An artificial Ahead/Behind time series pair. Bottom: The average correlation functions for a set of 20 time series pair like those in the top panel. The correlations near 1 result from the dual-spacecraft method, while the correlation peaks near 0.8 are found from the individual spacecraft methods used in the previous chapter. See text for details on the creation of the artificial time series pair in the top panel.

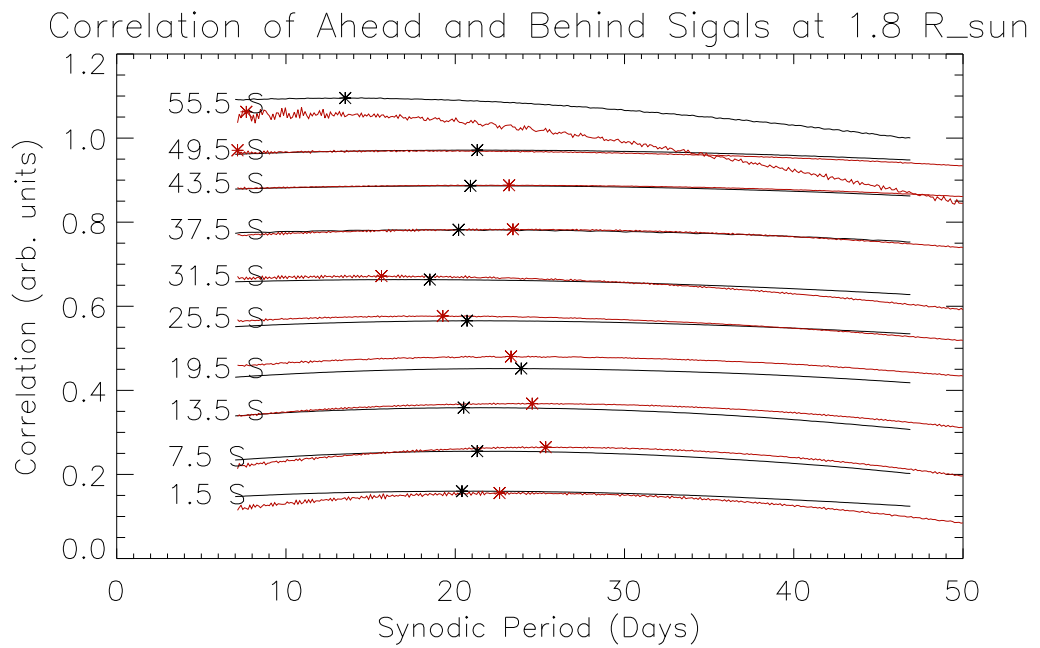


Figure 4.5: The dual-spacecraft results for several time series in the southeastern quadrant. The black (red) curves are determined with the first (second) method described in appendix B. The peaks of the individual curves are marked with asterisks. The time series for the 55.5 S and 49.5 S latitude bands showed streamer belt material sporadically over the course of the time series, which likely degraded the cross-correlation results. The results for all latitude bands peak at unexpectedly low values.

of both spacecraft. The first sharp spike, while noticeable in the time series, is an ejection that is small and faint enough to almost go unnoticed in coronagraph movies. The second spike (indicated by the arrow) occurs just after the passage of a CME front, when the more diffuse core of the CME brightens a large portion of the selected superpixel. Removing events such as these by eye would have been a very difficult and subjective process.

Quantifying the contribution of these impulsive, simultaneous events to the correlation function is also difficult. In the case of the CME in figure 4.6 it is difficult to say at what point each CME starts and stops affecting the time series. Also, a CME may have associated phenomena (like streamer deflections) that occur at different relative times. The number of CMEs that occur during the time period studied (STEREO COR1 observed over 400 CMEs between late 2006 and late 2009, about 0.5 per day [84]) makes them difficult to dismiss.

4.6 Feature Scale-Size Analysis

In this section I discuss different ways in which I have examined the rotation rates of small- and large-scale features of the time series separately. There are two reasons the correlation of features of various scale sizes is of interest here. The first concerns the unresolved question of the relative importance of impulsive events like CMEs in the correlation function calculation. CMEs typically take on the order of several minutes to several hours to traverse the COR1 FOV, so it was hoped that removal of features with these scale sizes might improve the rotation period measurements in figure 4.5.

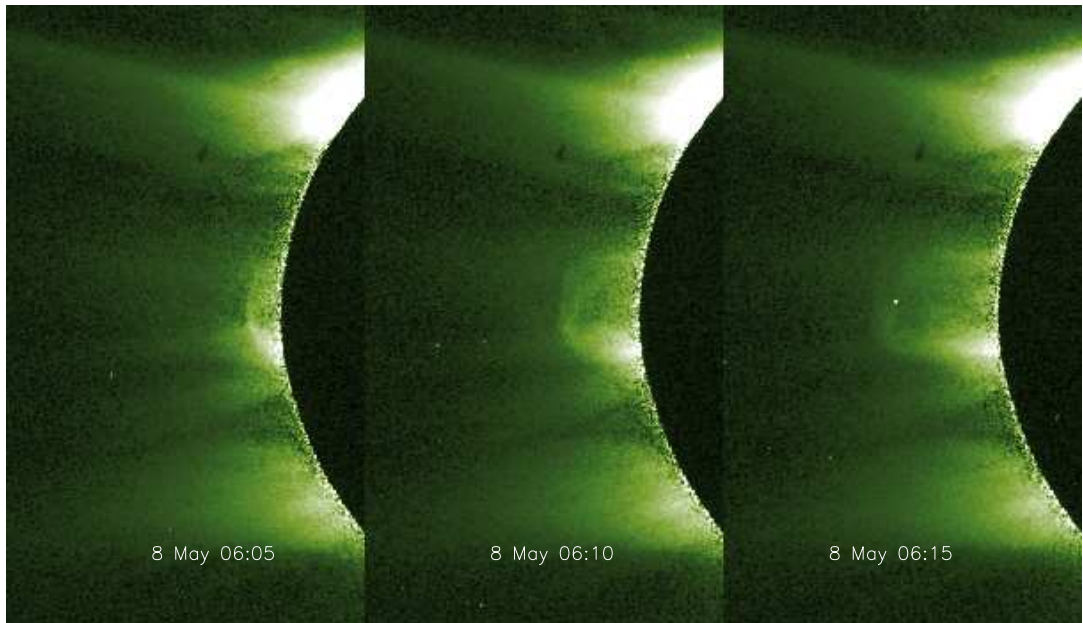
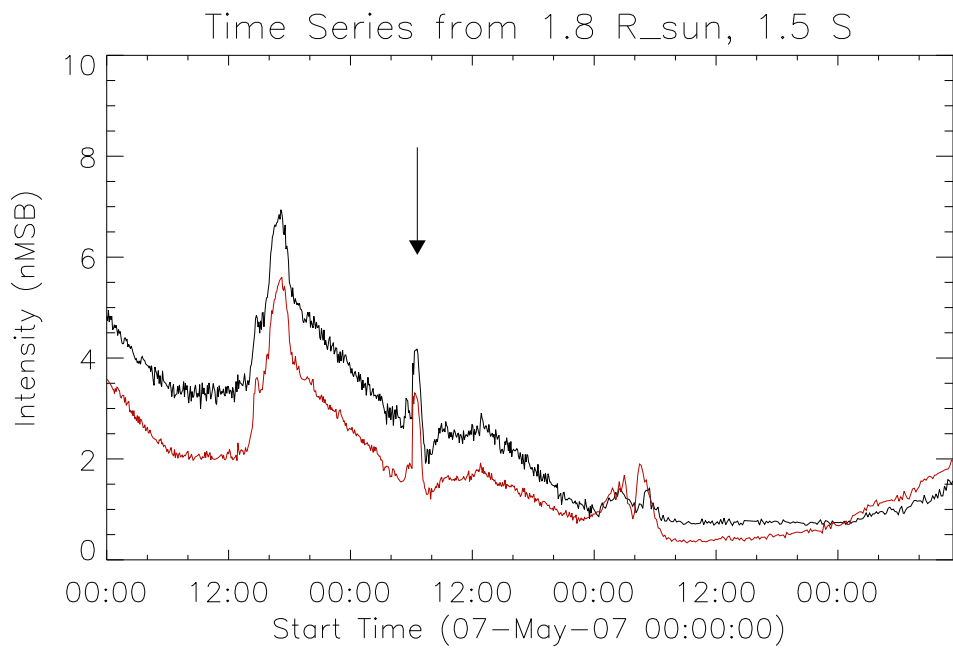


Figure 4.6: Top: A portion of the two time series from a superpixel at 1.8 R_{sun} and 1.5 S POS latitude, showing several impulsive events that happen nearly simultaneously in the two spacecraft despite the 14.5° longitudinal separation during the time period shown. The second spike, indicated by the arrow, occurs at 06:35, just after the passage of the CME front shown in the bottom panel.

The second reason to investigate the correlations of features with different scale sizes is related to the optical thinness of the corona. If the ability to measure differential rotation by cross-correlating photospheric magnetic measurements is dependent upon having sufficient longitudinal resolution, as stated by Snodgrass and Smith [80], then the optical thinness of the corona presents a serious challenge, since what is measured at a single projected latitude is actually the scattering by electrons over a range of longitudes all along the LOS. Small scale features (small, abrupt changes in the intensity as a bright, narrow feature moves into and then out of the LOS) may represent the only possibility for measuring the rotation of longitudinally fine-scale structures.

Features of different scale sizes have been isolated by pre-processing the Ahead and Behind time series in three different ways:

1. Constructing a boxcar smoothed version of the time series (using smoothing windows of variable width) to isolate large-scale features, and subtracting it from the original time series to isolate smaller-scale features.
2. Convolution of the time series with a kernel akin to a derivative operator, $K = \frac{1}{2m}[-1 \dots -1, 0, 1 \dots 1]$, where the ellipses represent a variable number $n = m - 2$ of duplicate entries.
3. Reconstructing the time series from wavelet expansions using a variable number of small and large wavelet scales.

Once a particular scale size has been isolated the time series are cross-correlated as described in section 4.3.

Each of the methods listed above assumes even spacing of the data points, which requires interpolation of the data; in this study I chose to interpolate over Θ , the heliospheric longitude of the spacecraft at the time of each observation. The heliospheric longitude used here is expressed in the Heliocentric Inertial (HCI) coordinate system, based on the earlier Inertial Heliographic (IHG) coordinate system [14]. This system takes the center of the sun as its origin, and aligns the z-axis with the north rotational pole and the x-axis with the ascending node of the ecliptic in 2000. (See [91] and references therein for a description of coordinate systems used in analysis of STEREO data.) Ideally one would want to interpolate the time series in such a way that the features being observed at the limb by the spacecraft in each observation were equally spaced in heliospheric longitude. However, this would require knowledge of the solar rotation rate I am attempting to measure. Interpolation over Θ is not quite equivalent, but is adequate for our purposes. Data points that are interpolated from time periods when there is a data gap larger than the interpolation spacing are neglected when the correlation of the resulting two time series is calculated.

4.6.1 Boxcar Smoothing

The first method I used to separate the large and small scale features in the time series was smoothing with a running average. This smoothed signal emphasizes the large-scale features of the time series. Subtracting the smoothed signal from the original time series emphasizes the small-scale features. I varied the size of the smoothing window between 50 and 2500 spacecraft longitude steps, or (using the

average spacecraft rotation speeds) about 8 hours to 16 days.

Figure 4.7 shows the results of cross-correlating smoothed versions of the curves in figure 4.2. As the size of the smoothing window is increased, the correlation curve shifts rightward and upward. Eventually a peak correlation curve (shown in red) is reached, and the cross-correlation curves begin to flatten while their peak continues to move towards longer periods. The optimal smoothing width, corresponding to the highest cross-correlation peak, is about 2.6 days and indicates a synodic equatorial rotation rate of 27.2 days. The bottom panel shows the smoothed curves for the Ahead (black) and Behind (red) spacecraft using the optimal smoothing width, for reference.

Figure 4.8 shows the result when the original time series in figure 4.2 are cross-correlated after being roughened by subtracting smoothed curves of varying width from them. As the smoothing width of the subtracted series decreases, the cross-correlation function gradually falls, with the cross-correlation at high periods falling faster than that at shorter periods. Eventually the correlation signal becomes very small and noisy, with some short, wide, noisy peaks near 20 and 28 days. A reference curve has been chosen (plotted in red) and the corresponding roughened time series for the Ahead and Behind spacecraft are shown in the bottom panel.

4.6.2 Convolution

The second scale separation method focused more on the relationship between changes in the Ahead and in the Behind time series. I convolved each time series with a kernel $K = \frac{1}{2m}[-1, \dots, -1, 0, 1, \dots, 1]$, where the ellipses represent a variable

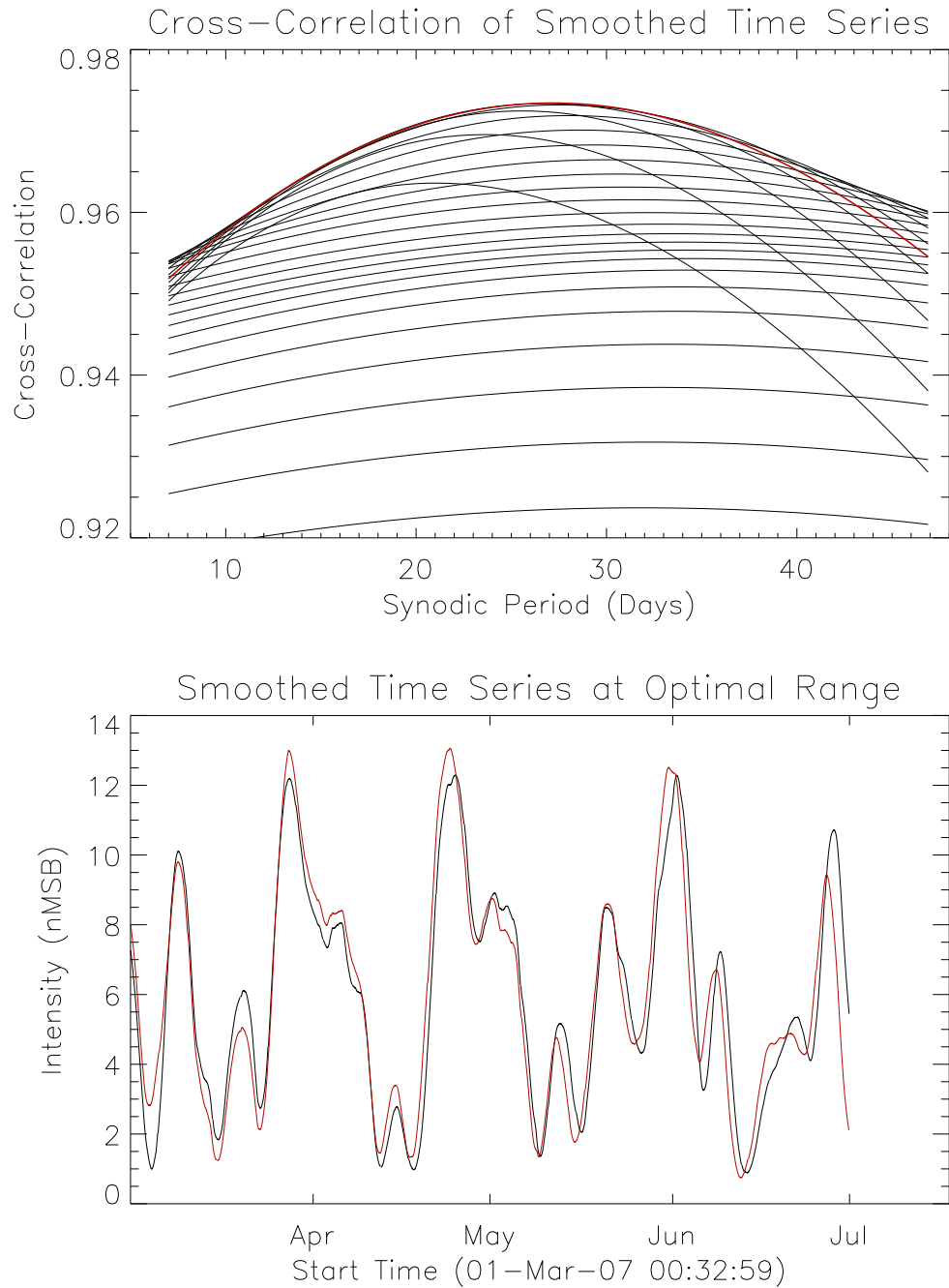


Figure 4.7: Results of pre-processing the cross-correlated time series by smoothing with a boxcar average. The top panel shows the cross-correlation functions for smoothing windows between 8 hours (most sharply peaked curve) and about 16 days (bottom curve). The cross-correlation maximum evolves towards longer periods as the width of the smoothing window is increased. The curve highlighted in red achieves the greatest maximum cross-correlation value, and is referred to in the text as the optimal curve. The bottom panel shows the smoothed time series corresponding to this cross-correlation curve.

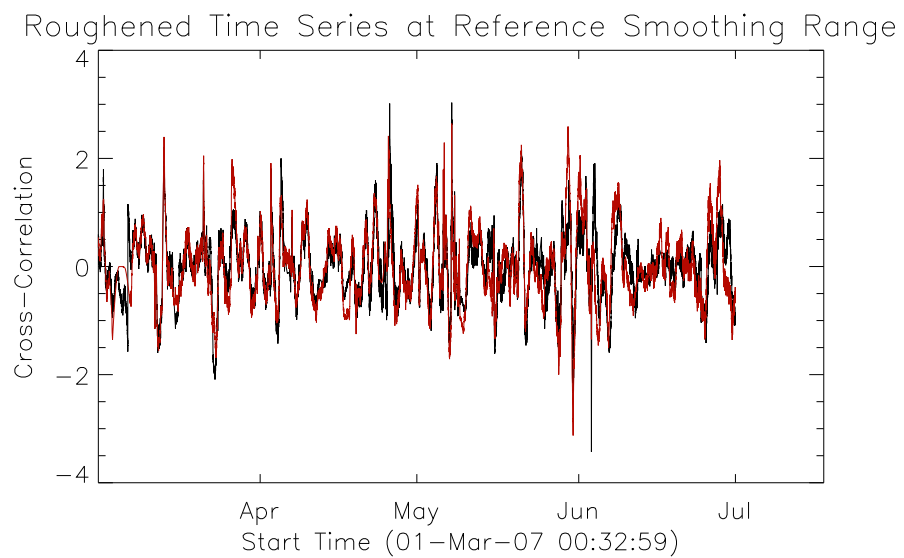
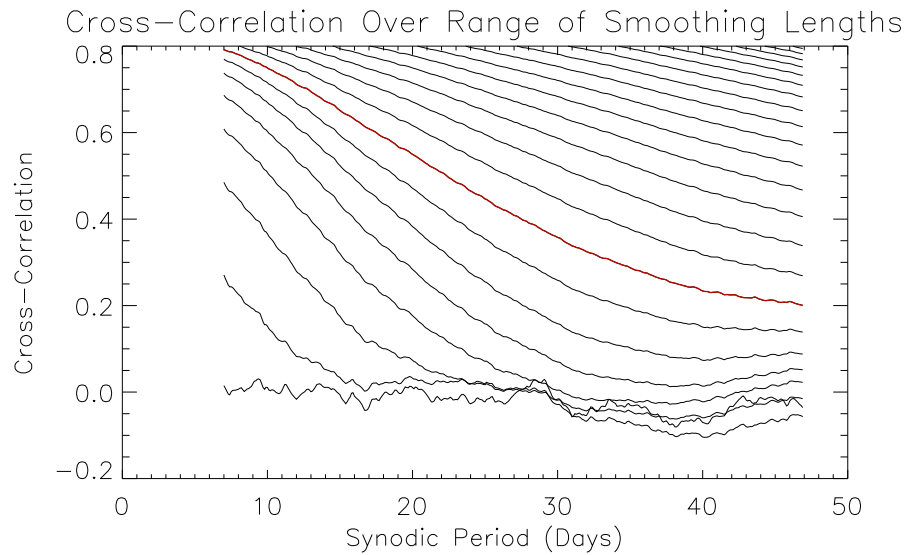


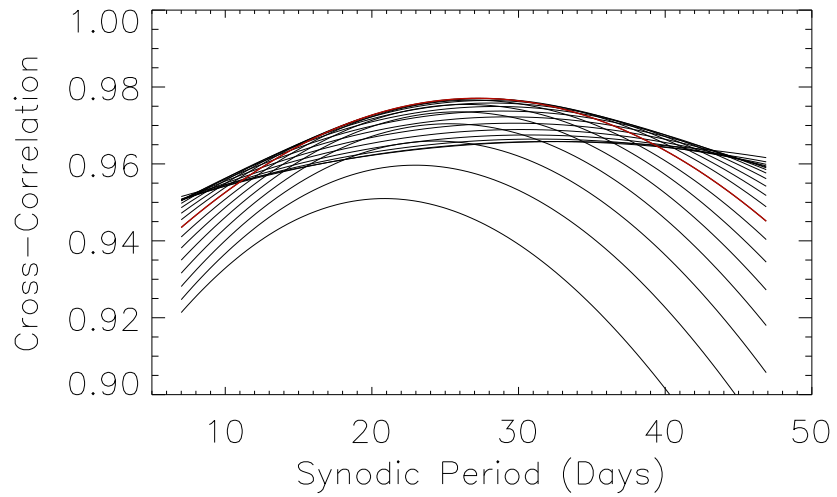
Figure 4.8: Cross-correlation results after pre-processing the input time series by subtracting a smoothed time series. The top panel shows the cross-correlation curves for smoothing windows between about 8 hours (bottom curve) and about 8.5 days (top curve). For reference, a representative curve has been highlighted in red and the pre-processed intensity time series corresponding to this red curve are shown in the bottom panel.

number $n = m - 2$ of repeated elements. Convolution with the kernel K is equivalent to subtracting the average of the m observations preceding each observation from the average of the m observations following it. In this sense it is proportional to a local derivative of scale m . Varying m allows one to examine the correlation of various scale-size changes between the Ahead and Behind spacecraft. To study the large-scale changes I used values of m corresponding to times from about 1.5 days to about 6.6 days, and for the small-scale changes I used values of m corresponding to times from about 19 minutes to about 47 minutes.

The top panel of figure 4.9 shows the cross-correlation of the large-scale changes, for a range of values of m . The cross-correlation behaves in a similar manner to that seen with smoothed input time series: as m increases the cross-correlation peak shifts up and towards longer periods, then the curve begins to flatten, with the peak dropping but continuing to move towards longer periods. The curve with the highest peak correlation is again highlighted in red and the m value used to create this curve is referred to as the optimal kernel size, which corresponds to about 3.4 days and indicates a rotation period of 27.2 days. The curve corresponding to the optimal kernel size is marked in red. The bottom panel shows the convolved Ahead and Behind curves for the optimal value of m .

Figure 4.10 shows the results of the convolution scheme for a range of smaller m values. As m decreases the correlation curve falls towards zero; as in figure 4.8, the correlation at longer periods decreases more rapidly than at shorter periods. For small m values the curve develops some peaks, which gradually become noisier until the minimum scale size is met. A reference correlation curve is highlighted in red,

Cross-Correlation of Convolved Time Series



Convolved Time Series at Optimal Kernel Size

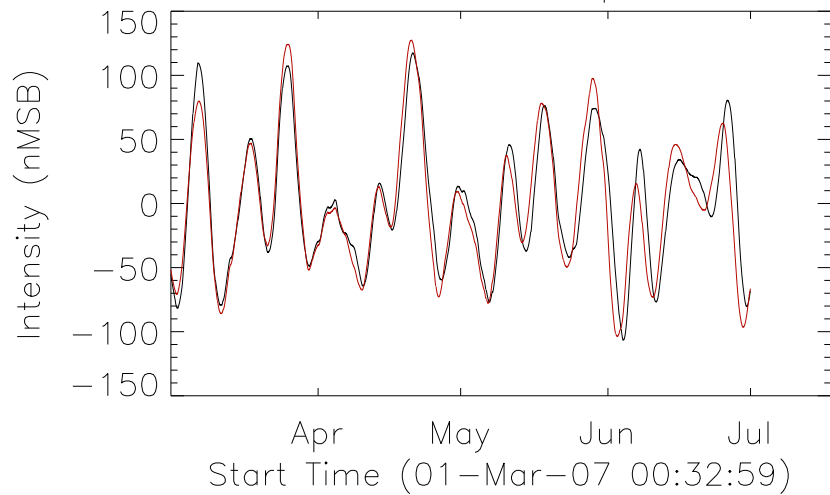


Figure 4.9: Results of pre-processing the cross-correlated time series by convolution with the kernel K described in the text for a range of m values. The top panel shows the cross-correlation curves for m values between about 1.5 days (bottom curve) and about 6.6 days (flattest curve). The optimal cross-correlation curve is again highlighted in red. The pre-processed time series corresponding to this curve are shown in the bottom panel.

with the convolved Ahead and Behind time series corresponding to this value of m shown in the bottom panel.

4.6.3 Wavelet Filtering

The final method I used to separate the small and large features was wavelet filtering, using the Interactive Data Language (IDL) program *wavelet.pro* created by Torrence and Compo [95]. By applying a wavelet transform with only a limited number of small (or large) wavelet scales, and reconstructing the time series from just those wavelet components, I isolated features with the scale sizes I was interested in. The mother wavelet used to form the basis functions of the wavelet expansion in this study is the so-called “Mexican Hat” wavelet, also known as a derivative of Gaussian (DOG) of order 2. Figure 4.11 shows the DOG wavelet.

To study the large-scale features using wavelet filtering, I first reconstructed the two time series using all wavelet scales above approximately 2.4 hr (the largest scale is set by the length of the data series, approximately 120 days). Then I gradually removed the smaller wavelet scales. For the small-scale features I used scale sizes up to a limit, initially set at approximately 20 hours, then gradually removed the larger scales. The minimum scale size would normally be twice the interpolation spacing, but I used four times the interpolation spacing, about 41 min, because of irregularities in the nominal cadence of the COR1 images, noted in section 4.2.

Figure 4.12 shows the cross-correlation functions for a pair of time series reconstructed from their large-scale wavelet components. As the minimum wavelet

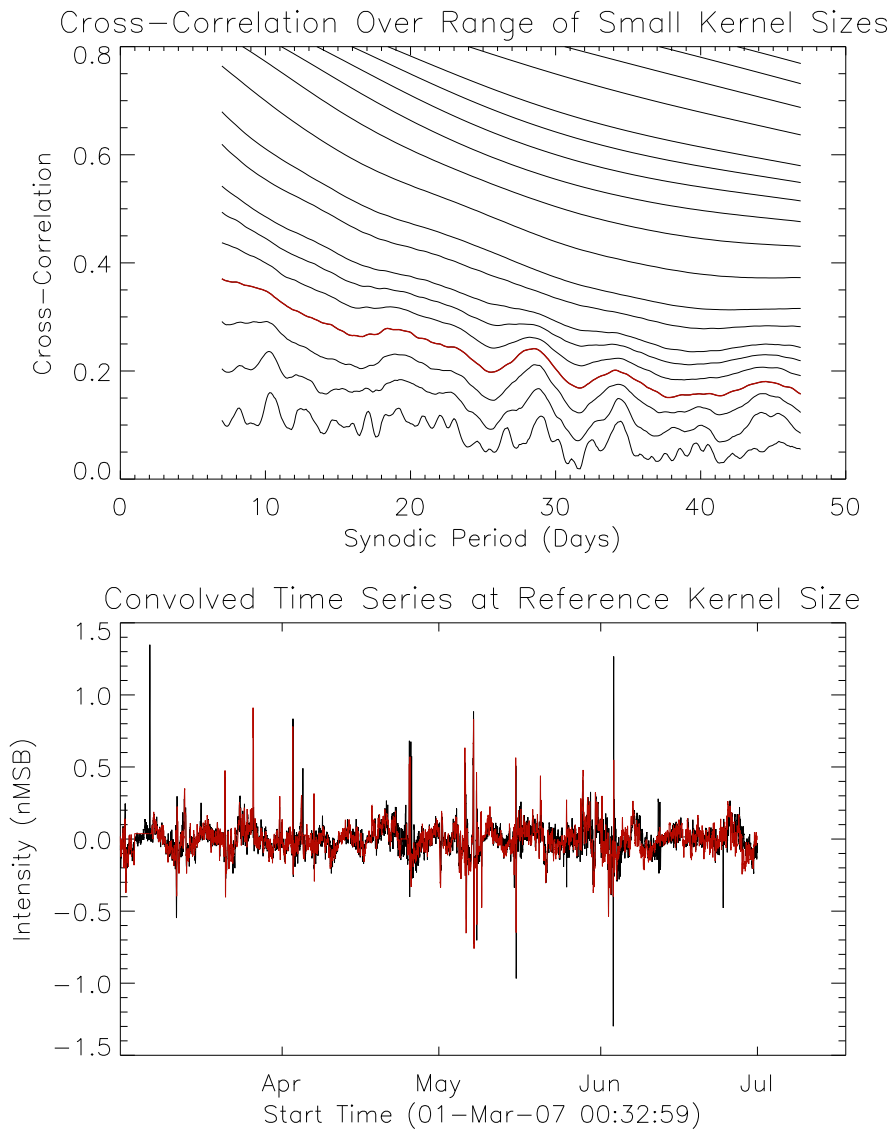


Figure 4.10: Results of pre-processing the cross-correlated time series by convolution with the kernel K for a range of m values between about 19 minutes and 47 minutes. The pre-processed time series corresponding to the red highlighted curve are shown in the bottom panel for reference.

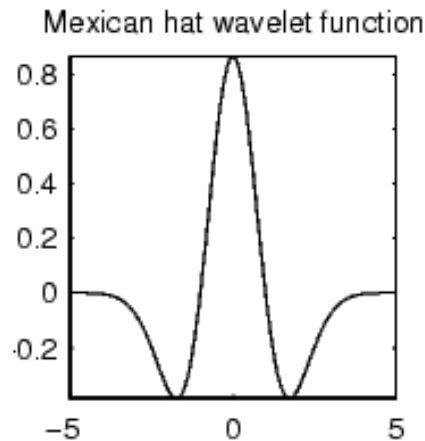
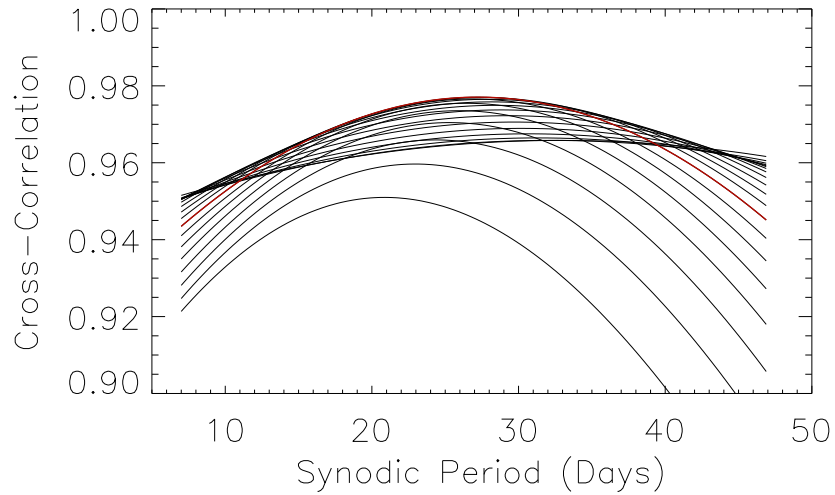


Figure 4.11: The “Mexican hat” mother wavelet.

scale is gradually increased, the peak of the cross-correlation function shifts upward and towards longer periods, as in figures 4.7 and 4.9. The correlation curve with the highest peak is again marked in red in the first panel, and the Ahead and Behind curves associated with this optimal value of the minimum scale size are plotted in the bottom panel. The optimal correlation curve is generated using a minimum wavelet scale of approximately 20 hours, and indicates a synodic rotation period of 27.1 days.

Finally, figure 4.13 shows the result when the two time series are reconstructed from only their smallest wavelet scale components, for a range of maximum scale sizes. As the maximum scale size is decreased, the cross-correlation function behaves as in figures 4.8 and 4.10, falling first at longer periods and then at shorter, gradually settling to a much smoother curve than obtained from the previous two methods, with a pronounced peak near 28 days. The result for the smallest wavelet scale used is highlighted in red, and the corresponding reconstructed time series are shown in the bottom panel.

Cross-Correlation of Convolved Time Series



Convolved Time Series at Optimal Kernel Size

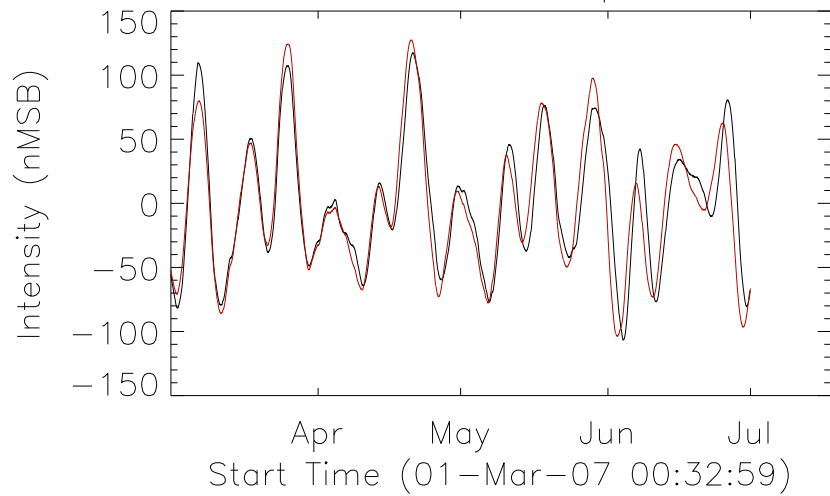


Figure 4.12: Cross-correlation of Ahead and Behind time series after reconstruction from the largest wavelet components. The minimum wavelet scale included in the reconstruction increases from about 2.4 hours for the bottom curve to about 3.4 days for the flattest curve. The cross-correlation curve with the highest maximum is again highlighted in red and referred to as the optimal curve. The bottom panel shows the pre-processed time series corresponding to this optimal cross-correlation curve.

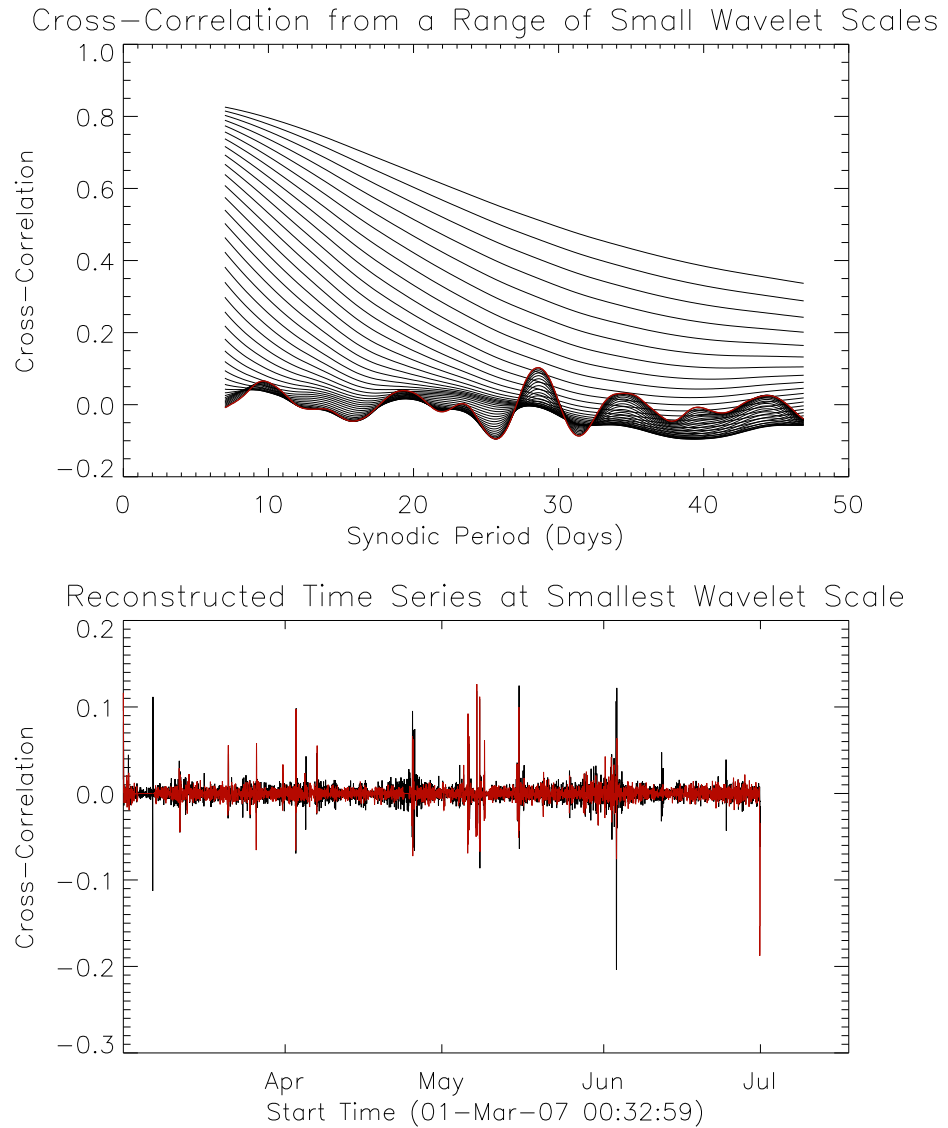


Figure 4.13: Cross-correlation of Ahead and Behind time series reconstructed from their smallest wavelet components. Here the minimum wavelet scale is set at about 41 minutes by the resolution of the time series, and the maximum wavelet scale included in the reconstruction is progressively decreased from about 20 hours to just the minimum scale to isolate progressively smaller-scale features in the time series. The top panel shows the cross-correlation curves, where the red curve at the bottom includes just the minimum wavelet scale and as the size of the maximum wavelet scale is increased the curve flattens and rises. The bottom panel shows the pre-processed time series corresponding to the red curve.

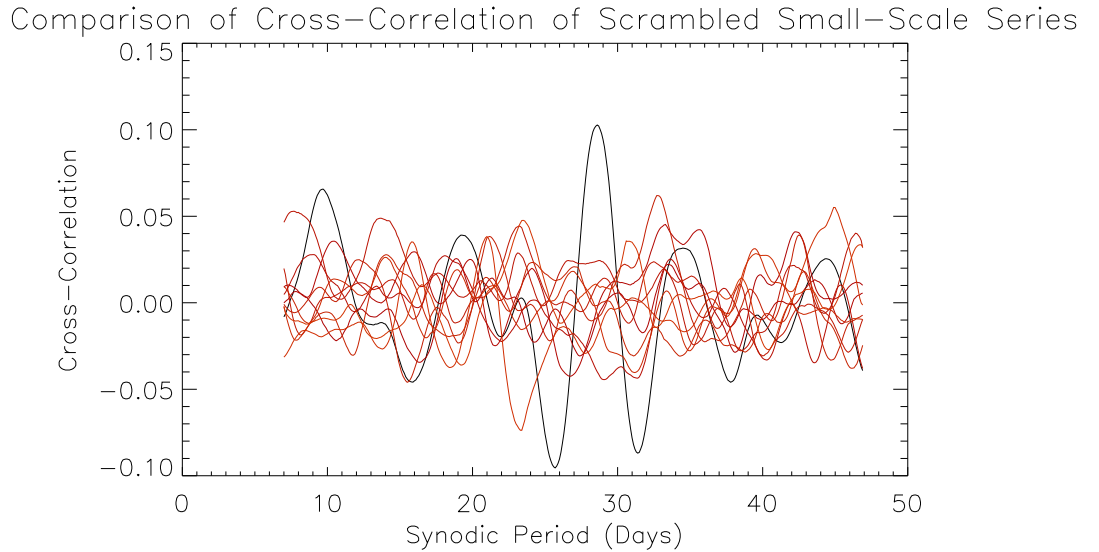


Figure 4.14: Cross-correlation of the wavelet-processed time series from the bottom panel of figure 4.12 (black) and the cross-correlation functions measured after scrambling the Ahead time series into random order (red).

For comparison purposes, I tried scrambling the Ahead time series in the bottom panel of figure 4.13 into a random order and then calculating the cross-correlation between the Behind and scrambled Ahead time series, for several realizations of the scrambling order. The resulting cross-correlations are shown in red in figure 4.14, along with the cross-correlation function for the original, unscrambled, reconstructed time series. The largest feature of the cross-correlation function, the peak near 28 days, does not seem to be a result of either random chance or of the time series spacing or length.

The correlation curves resulting from the large- and small-scale analyses using the three different techniques listed above are shown together in figure 4.15. The top panel shows the “optimal” results from figures 4.7, 4.9, and 4.12. The peaks of these curves give an average synodic rotation period of 27.2 days. The bottom

panel compares the red reference curves from figures 4.10 and 4.13, and the smallest-scale roughened correlation curve from figure 4.8. The curves are more similar than might be expected from inspection of the reference time series in the bottom panels of figures 4.8, 4.10 and 4.13. The main peaks between 25 and 31 days synodic period in the small-scale cross-correlation curves occurred at an average 28.6 days. (The boxcar-roughened curve's peak location was determined using a Gaussian fit while the convolved and wavelet filtered curves' peaks were taken to be the absolute maximum between 25 and 31 days.)

4.6.4 Discussion of Scale-Size Analyses

The consistency of the cross-correlation functions in figure 4.15 tends to suggest that the periodicities indicated by the cross-correlation curve may actually be physical. However, when I tried processing time series pairs from several latitudes in the southeastern quadrant in the same way, the results were highly variable. Figure 4.16 shows the latitudinal dependence of the cross-correlation function obtained from the optimal smoothing, convolution, and wavelet scales determined as described above. If the peaks in the cross-correlation curves represented actual rotation measurements I would expect to see the peak near 27 days in the top panel of figure 4.15 to appear consistently at or above that value in the higher latitudes. Instead, the peaks tend to drift toward shorter periods with increasing latitude, in disagreement with previous measurements in the corona and photosphere.

Figure 4.17 shows the cross-correlation functions at the same latitudes after pre-processing to emphasize small-scale features. While the three methods seem to

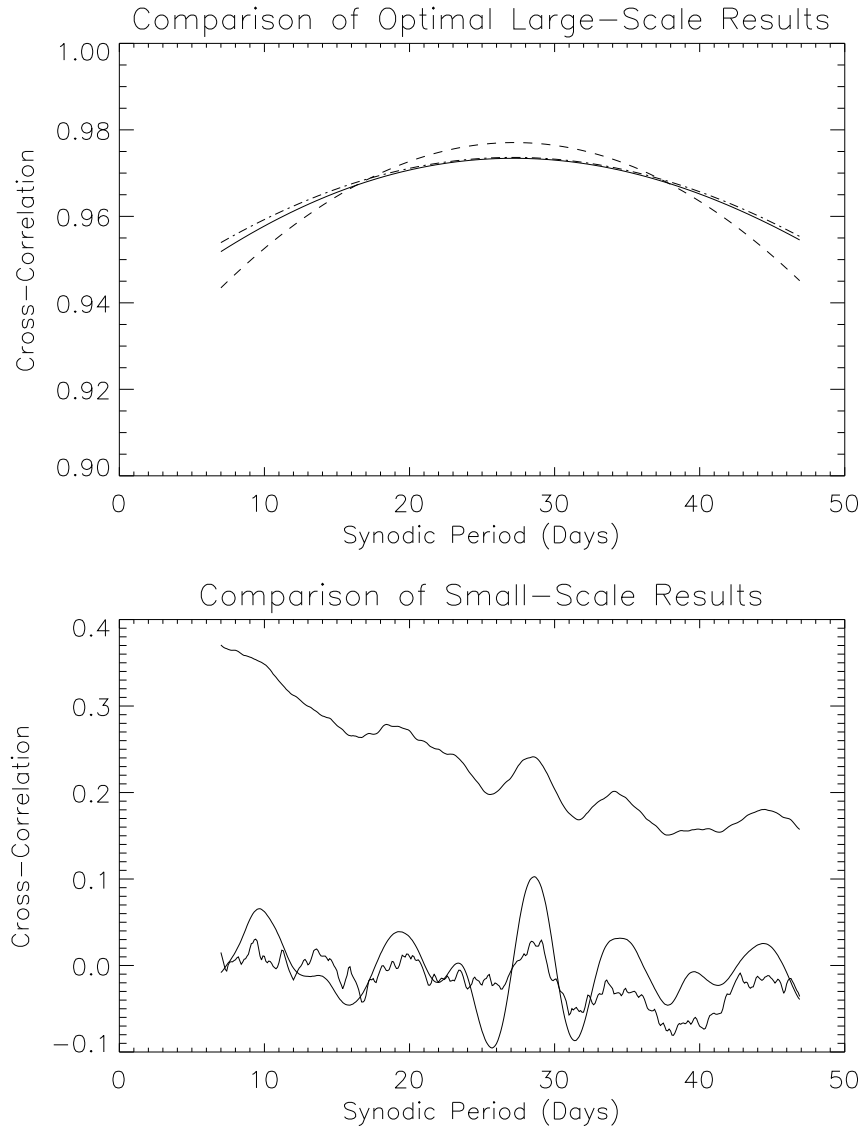


Figure 4.15: Top: A comparison of the “optimal” large-scale results of the three scale separation techniques for time series at $1.8R_{\odot}$ and 1.5 S POS latitude. Bottom: A comparison of the cross-correlation functions for the same time series pre-processed at the smallest wavelet scale, smallest smoothing scale, and at the reference kernel size from figure 4.10.

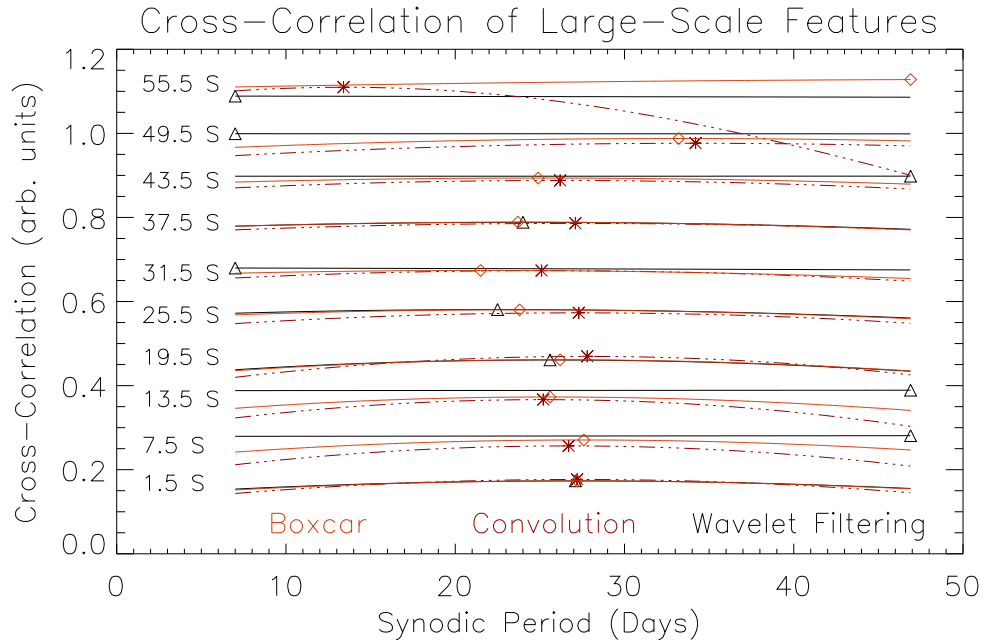


Figure 4.16: Cross-correlation of time series pairs from several latitudes in the south-eastern quadrant after pre-processing using the optimal smoothing (diamonds), convolution(asterisks), and wavelet scales (triangles) as explained in the text.

agree with one another to some extent, the cross-correlation curves vary from one latitude band to the next. Given this variability, it seems likely that the curves in 4.17 are dominated by noise in the time series. This seems reasonable given the largely incoherent appearance of the curves in the bottom panels of figures 4.8, 4.10, and 4.13.

4.7 Discussion

The STEREO mission has offered a unique opportunity to study the short time-lag rotation rate of the white-light solar corona. In this study I have presented several attempts to cross-correlate the Ahead and Behind intensity signals during times when the spacecraft were separated by less than one day's rotation (assum-

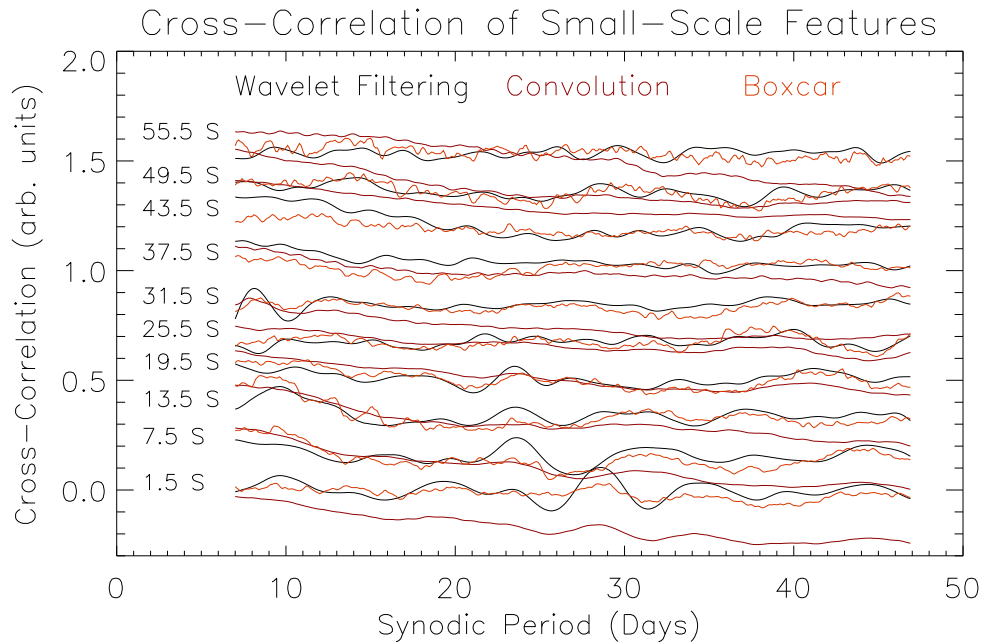


Figure 4.17: The results of cross-correlating time series pairs from several latitudes in the southeastern quadrant after pre-processing using the smallest wavelet and roughening scales and the reference convolution scale as described in the text.

ing the rotation rates measured in chapter 3). The results of cross-correlation of the original time series (see figure 4.5) show little apparent dependence on latitude; however, the rotation periods measured are inconsistent with results obtained in previous studies of the photosphere or corona, including the measurements presented in chapter 3. Cross-correlation of time series pre-processed using several techniques chosen to draw out large- or small-scale features (see figure 4.15) were more consistent with previous studies, particularly at equatorial latitudes, where the indicated rotation periods were 27.2 days in the large-scale analysis and 28.6 days in the small-scale analysis. No latitudinal dependence of the rotation rate was observed in either the large- or small-scale cross-correlation curves.

One explanation for the unexpectedly low values of the rotation rates measured

in the original data series may be that the cross-correlations are biased towards higher frequencies by the presence in the data of impulsive coronal phenomena like CMEs. In appendix C I show, for the idealized case of constant satellite separation, that the presence of simultaneous events in the two time series introduces a second term to the cross-correlation, proportional to the autocorrelation one of the time series (the autocorrelations of the two time series are roughly equal). This second term peaks around a rotational period of 0, indicating as one might expect that some of the material seems to be rotating from one spacecraft's POS to the other's at infinite speed. The cross-correlation spectrums of figure 4.5 may then be explained as a combination of two functions, one peaking near a time lag consistent with coronal rotation and one peaking at (or near) zero. Depending on the relative strengths and widths of the cross-correlation and autocorrelation peaks, the resulting cross-correlation curve might appear to have a single peak at an intermediate value of the rotation period.

To test the theory that the results of section 4.5 are influenced by a bias towards shorter rotation periods, I performed two tests. In the first I recreated the bias using artificial time series. In section 4.4 I presented artificial time series generated by introducing a random change to 80% of the 500 longitudinal points at each "time step" and interpolating between them. I later found that if I increased the standard deviation of these random changes to 0.08 and varied the percentage of the points to which a change was applied the measured rotation rates of the resulting series fell with the number of random changes. (The same effect was observed when the deviation was left at 0.035 as in section 4.4, but was less pronounced.) Figure

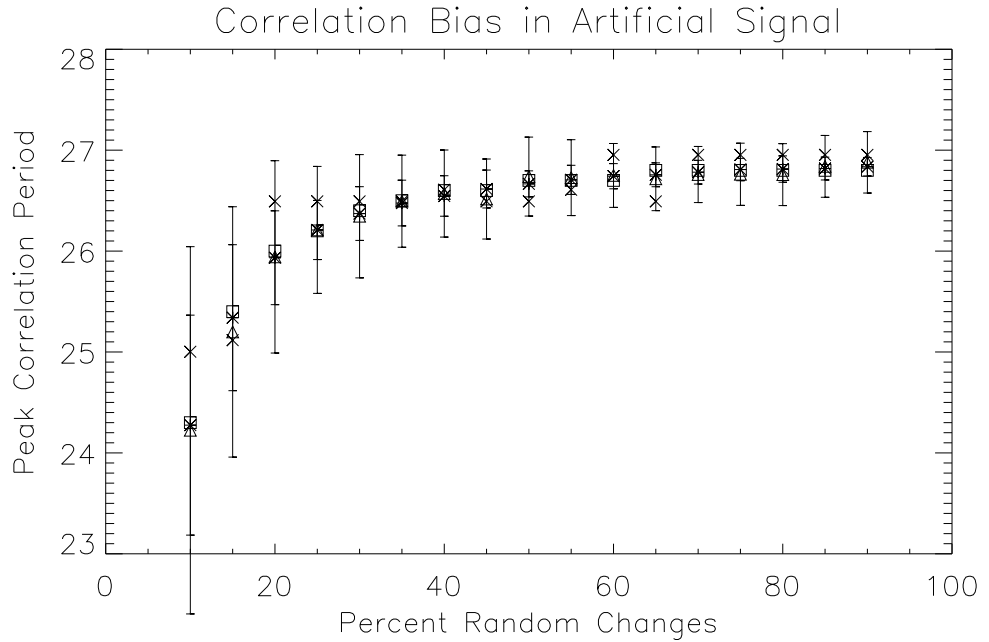


Figure 4.18: The rotation periods measured from complex artificial time series pairs generated by introducing random changes to the longitudinal structure and interpolating over 500 points. For each percentage value 100 realizations of the artificial time series were created. Asterisks and triangles represent the mean of the 100 period measurements, using cross-correlation calculation methods 1 and 2, respectively, as described in appendix B. Squares and X's show the location of the peaks when the 100 cross-correlation curves are averaged. The measured rotation period using all methods varies systematically with the percentage of the longitudinal points that are changed.

4.18 shows the measured rotation rates versus the percentage of random changes. By decreasing the number of longitudinal points changed in each time step I am also decreasing the number of points over which I interpolate, which increases the interdependence of the artificial Ahead and Behind time series. (Qualitatively this is like increasing the constant β from appendix C.) The rotation period derived from the cross-correlation clearly decreases with the number of altered points in figure 4.18.

The second test I conducted to explore the effects of simultaneous events on the

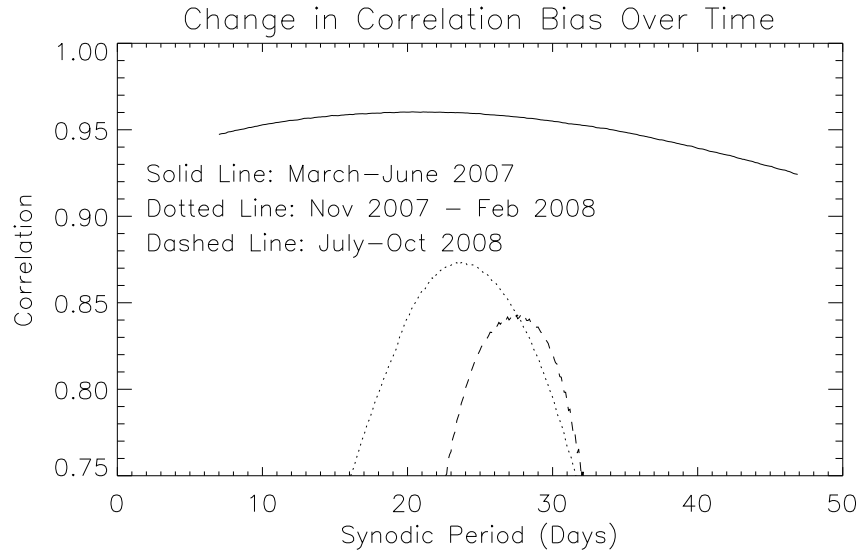


Figure 4.19: Cross-correlation of several four-month data sets from 2007 and 2008, showing a decrease in correlation bias as the STEREO mission progressed. The first data set is the one analyzed above, during which the longitudinal separation angle of the spacecraft increased from 1° to 16° . During the second data set the separation angle went from 38° to 46° , and during the third it increased from 58° to 81° .

cross-correlation was a comparison of cross-correlation of three sets of four months' worth of data. Figure 4.19 shows the cross-correlation of equatorial superpixels from the Ahead and Behind spacecraft during Mar-Jun 2007 (solid line), Nov 2007 - Feb 2008 (dotted line), and Jul-Nov 2008 (dashed line). In the figure the correlation peak is seen to decrease in height and width as the mission progresses and the spacecraft separation increases, and the peak location is seen to increase to about 27 days, as was seen in the previous chapter. The shift towards longer rotation periods is to be expected because the increase in the spacecraft separation ($\sim 85^\circ$ at the end of November 2008) results in fewer events seen in both STEREO spacecraft, and because the rotation-associated cross-correlation peak has narrowed and shifted away from the zero-lag autocorrelation peak.

If the cross-correlation curves in figure 4.5 are biased towards shorter rotation periods, that might explain not only the low measured rotation periods, but also some of the results of the scale-size analysis of section 4.6. It would seem that the bias comes from mid-sized features of the time series, consistent with CMEs, and is gradually removed as they are filtered out. This would explain why the cross-correlation curves of the small-scale analysis decrease first at large rotation periods as more and more intermediate-scale features are filtered out, because the width of the zero-lag autocorrelation peak is dictated by the size of the time series features.

Setting aside the issue of cross-correlation bias, the small-scale feature analysis is of particular interest. Given the apparent dominance of the small-scale cross-correlation by phenomena not related to rotation, it is probably not possible to resolve the smaller-scale features described by Snodgrass and Smith [80] well enough in the COR1 coronagraphs to measure their rotation rates.

4.8 Conclusions

The short time lag rotation period measurements resulted in unexpectedly low values at all latitudes, with an unexpected decrease in the rotation period with increasing latitude compared to the single spacecraft analyses. This result is inconsistent with previous measurements of coronal rotation in the corona and photosphere and most likely reflects a bias in the cross-correlation functions towards low periods, as demonstrated using artificial time series. From these results it would be unwise to try to draw any conclusions about the latitudinal dependence of the short time lag rotation rate.

Attempts to cross-correlate large-scale features extracted from the Ahead and Behind COR1 time series using smoothing, convolution, and wavelet filtering produced somewhat less irregular rotation measurements that fell between 21 and 28 days, suggesting that some but not all of the bias was being filtered out. Further scale-size analysis suggests that much of the bias is contributed by mid-size features, while small-scale features are dominated by noise. No evidence was seen for differential rotation in these measurements. Given the apparent dominance of the small-scale cross-correlation by phenomena not related to rotation, and the mid-size features by bias, it is not possible to resolve the rotation of the smaller-scale features described by Snodgrass and Smith [80] in the corona in this analysis.

Chapter 5

Localized Plasma Density Enhancements Observed in STEREO COR1

In the first chapter of this thesis I introduced CMEs, large eruptions of magnetized plasma from the solar corona. A formal definition of a CME was given by St. Cyr *et al.* [83], although there it is generally accepted that many coronal eruptions are seen that are arguably too small and too faint to be labeled CMEs. In this chapter I will describe measurements of small, localized plasma density enhancements (also known as “plasma blobs” in the scientific literature) traveling outward through the STEREO COR1 FOV. Using many height-time measurements of these features I attempt to measure the acceleration of the blobs in the COR1 FOV, and draw some inference about the physical process that causes the blobs to move away from the Sun. The results presented in this chapter have been previously published in the *Astrophysical Journal* [40].

5.1 Introduction

Plasma blobs is the term used to refer to small, moving density enhancements first observed by Sheeley *et al.* [74]; subsequently, plasma blobs and related inflows have been observed in many other studies [68, 61, 73, 72, 71, 70, 102, 100, 59]. The authors of [74] treated the density enhancements as passive tracers of the solar wind through the LASCO C2 and C3 coronagraph FOVs (see [13] for a description of LASCO). By measuring the heights of these features as a function of time and

combining many such measurements, they were able to plot an approximate curve of solar wind velocity versus height above the Sun. Additionally, Tappin *et al.* [90] performed a correlation analysis on low-latitude data from LASCO C2 and C3 and found a broad excess in correlations at positive radial speeds, indicating outward radial flow that almost certainly included plasma blobs, both resolved as in the studies by Sheeley, Wang, and co-workers and likely density enhancements that were too faint or small to be visually isolated. Both [74] and [90] treated their flow measurements as indicators of the local solar wind speed and acceleration.

Robbrecht *et al.* [61] describe the automated detection of small eruptions by the CACTus CME detection software. CACTus finds many more small eruptions than are catalogued by observers as CMEs and the authors pose the question: do these small ejections represent a unique eruption process, or are they generated in the same manner as CMEs but on a smaller scale? Indeed, the first description of plasma blobs offered by Sheeley *et al.* [74] is entirely consistent with the observational description of CMEs given by St. Cyr *et al.* [83].

Given their use as solar wind tracers and their possible relationship to CMEs, it is important to understand the origin of the blobs themselves. Wang and co-workers have proposed three possible origins for the observed inhomogeneities [102, 103]: (1) streamer evaporation, (2) magnetic reconnection at the tips of distended streamers, or (3) reconnection between closed and open field lines in or near the streamer belt (also sometimes referred to as footpoint exchanges). While streamer evaporation may account for some of the events, it is problematic for several reasons. It requires a steady addition of new loops into the streamer to be consistent with the observed

stability of coronal streamers, it leads to an increase in the solar magnetic flux, and it is inconsistent with the shapes of plasma blob observations in the outer corona [103]. Thus it seems that either pinch off of streamer tips or footpoint exchanges are the most likely origins for the observed plasma blobs.

One way to distinguish between these two proposed blob origins is through observations at lower altitudes. A two-dimensional model of streamer tip reconnection is presented by [106], and shows the formation and propagation of several blob-like plasmoids. These plasmoids are not unlike small flux ropes recently observed by *in situ* solar wind instruments [18, 53, 54]. However, the magnetic islands produced in the model tend to form above the streamer tops, near or above $2R_{\odot}$. Footpoint exchanges between open and closed field lines, on the other hand, seem more amenable to the formation of blobs over a range of heights in the lower corona.

In this study I use COR1 height-time images at fixed angular position to trace the motion of faint density enhancements outward through the corona as was done by Sheeley *et al.* [70]. The COR1 FOV extends as low as $1.4 R_{\odot}$, so using this instrument I can lower the threshold altitude at which blobs are observed (previously $2 - 2.5 R_{\odot}$).

In the next section I will show some examples of the observed plasma blobs and discuss the image processing techniques used to help identify them. Section 5.3 displays some characteristics of these events in the COR1 FOV based on height-time measurements for a large sample. The final section compares these measurements with previous results and discusses the implications for blob origin.

5.2 Method

Observations of plasma blobs in COR1 are complicated by multiple effects. In order to see coronal features in COR1 images the stray light background must be removed from the images, as described in chapter 2. Using the standard instrumental background images used in chapters 3 and 4 is unsatisfactory because relatively stationary features like streamers that are bright enough to hide the fainter plasma blobs remain.

A special running-difference technique is used, where the background subtracted from each image is the minimum value of each pixel in a small window (approximately 1.5 hours) of images around it. This has the advantage of subtracting features like streamers that are stationary on the timescale of days so that faster-evolving features can be clearly seen, while tending to produce a less noisy image than a standard (single-frame) running difference technique.

Even using the running-background subtraction it can be difficult to track small features that expand against a large, noisy background (see figure 5.2). To simplify this task I use “J-maps”, following [70, 15]. J-maps are formed by removing an angular slice (some authors use a rectangular slit) centered on the feature’s trajectory, subtending five degrees latitude in the POS, from each frame in a running difference movie. By integrating the intensity in each slice over angle and stacking the resulting pixel columns side-by-side sequentially to form an image in which the vertical direction is the POS height and the horizontal direction is time (for example, see figure 5.2.) The angular integration increases the visibility of features as they

move outward through the corona. In fact, many features are observed in height-time plots that are very difficult or impossible to see in the running-difference movies, although a careful observer can usually predict where they will be seen. Figure 5.2 shows some examples of COR1 height-time images; they have been enhanced to show feature locations more clearly using the Radon transform, similar to the Hough transform used by the CACTus automated CME detection program [60]. While the Radon transform can be used to help confirm the general location of a faint track, it also smears out areas of strong signal over linear paths; it can give the false impression that the feature does not undergo acceleration, or that it has broken up into diverging tracks. For these reasons all data analysis was done using measurements from the original running-difference, height-time images.

Using running-difference images does introduce some ambiguity in the interpretation of the observations. Because a different background image is subtracted from each frame, it is difficult to distinguish relative brightness changes due to reorganization of the coronal plasma from changes in the subtracted background image. In order to show that the features seen are real and not artifacts of the differencing process, figure 5.3 shows an event seen in both COR1 running difference and COR2 base difference images. The top image shows sections of several COR2 images, with arrows indicating the feature of interest. The lower left image shows the same feature in a COR1 height-time image, enhanced using the Radon transform, a transform used to identify linear features in images [56]. The bottom right shows the COR1 and COR2 height measurements plotted together as a function of time; the measurements below $4 R_{\odot}$ are from COR1 and those above are from COR2. De-

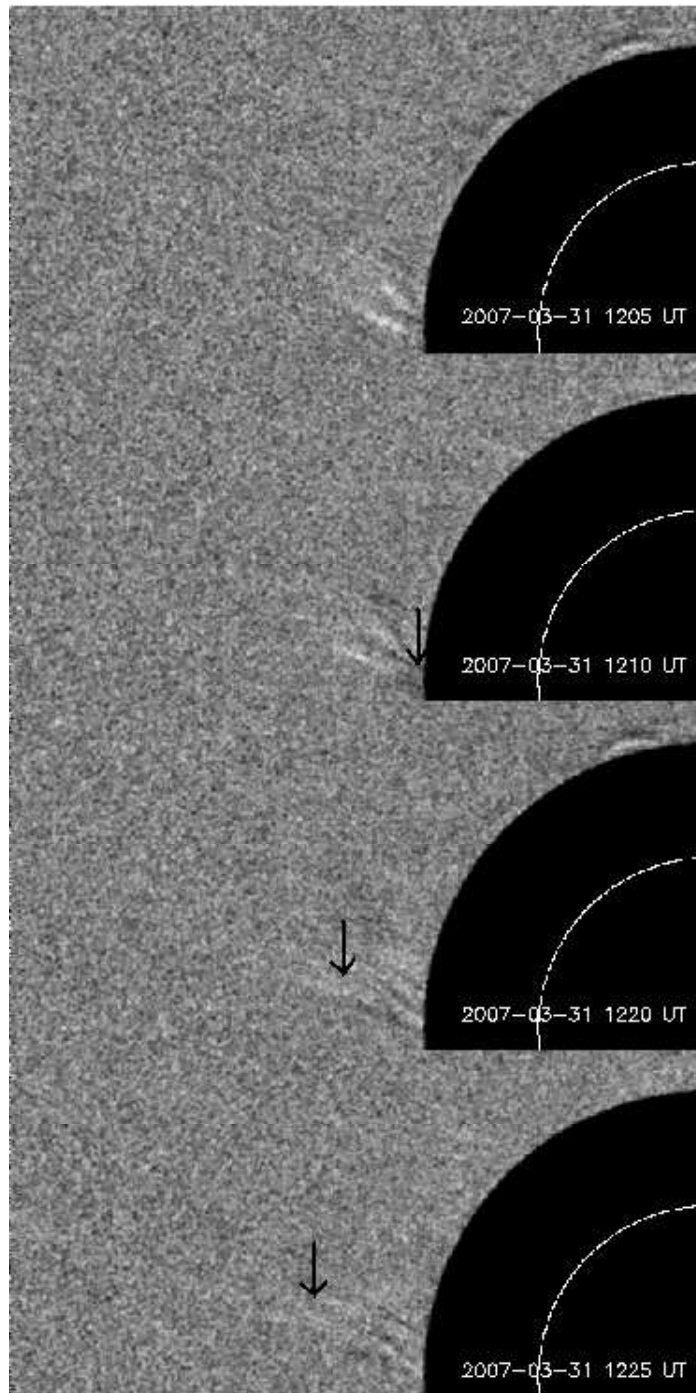


Figure 5.1: A plasma blob seen in COR1-B running difference images. Arrows in the bottom three frames point to the approximate location of a Y-shaped tail at the back end of the feature. The front of the feature seems to be much fainter and is obscured during its emergence from beneath the occulter by an apparent twisting motion.

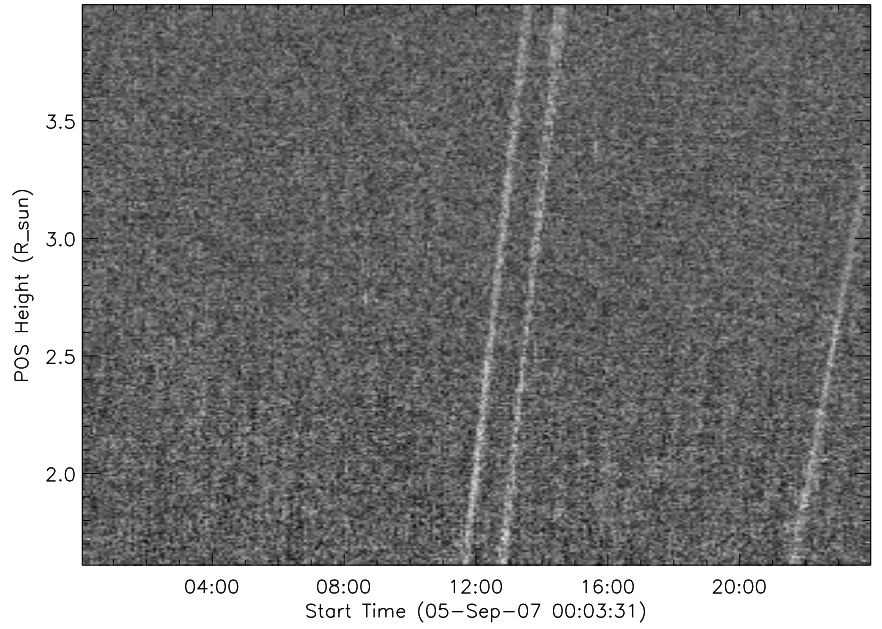
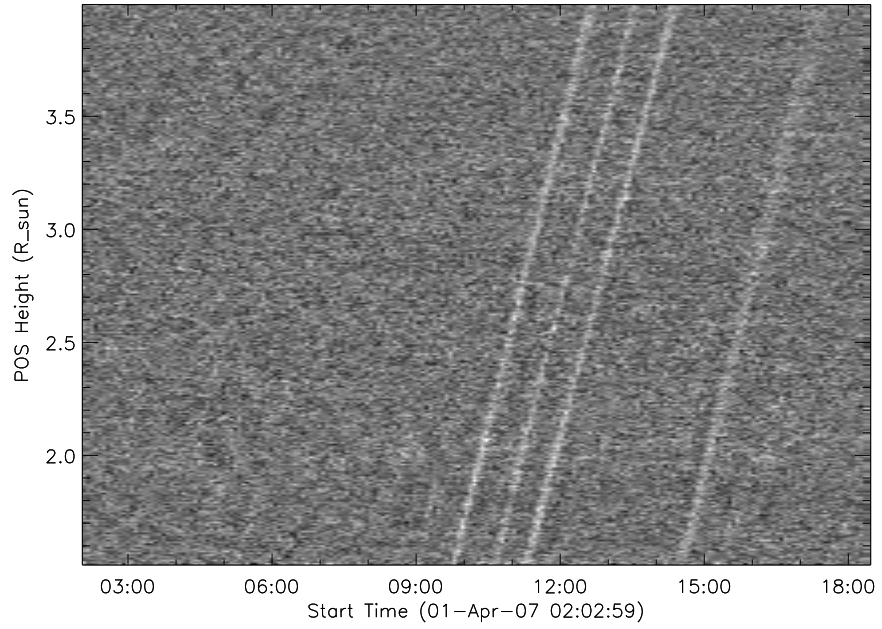


Figure 5.2: Blobs seen in COR1-B height-time images at 345° and 172.5° . These images were enhanced using the Radon transform.

spite the ambiguity introduced by using running-difference images, the track seen in the COR1 height-time image corresponds to a real, traveling density enhancement observed in COR2.

In order to study the plasma blobs in the COR1 FOV, I divided nineteen days' worth of COR1-B data (recorded 27 March - 2 April 2007, 4-8 September 2008, and 27 March - 2 April 2008) into five-degree angular bins. I made height-time images of each angular bin and measured the trajectories of as many events as possible. The dates above were chosen to contain as few CMEs as possible, as these complex events tend to be seen multiple times in multiple bins, so that they would likely skew the overall statistics. (For example, a CME seen on 31 March 2007 contributed 32 separate "events" out of a total of 54 for that day, all with similar trajectories.) Those CMEs that did occur within the observational periods were carefully removed from the dataset. Three CMEs were identified unambiguously in the COR1 CME Catalog during the three time periods studied, while others were identified according to the following criteria:

1. They span at least three adjacent 5° angular bins.
2. At least two outward-moving features are seen in at least one of the angular bins within one hour.

For each CME identified I searched for the first 6-hour quiet period after the passage of the CME, and any features taking place before the quiet period were removed along with the CME itself. I also identified events in adjacent angular bins whose heights differed by less than $0.1 R_\odot$, about twice the error in the height

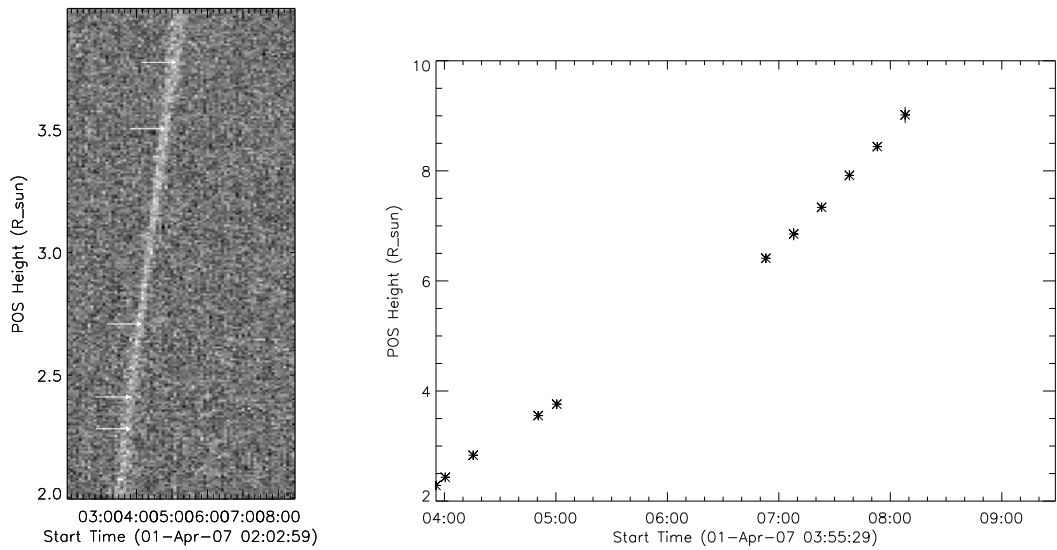
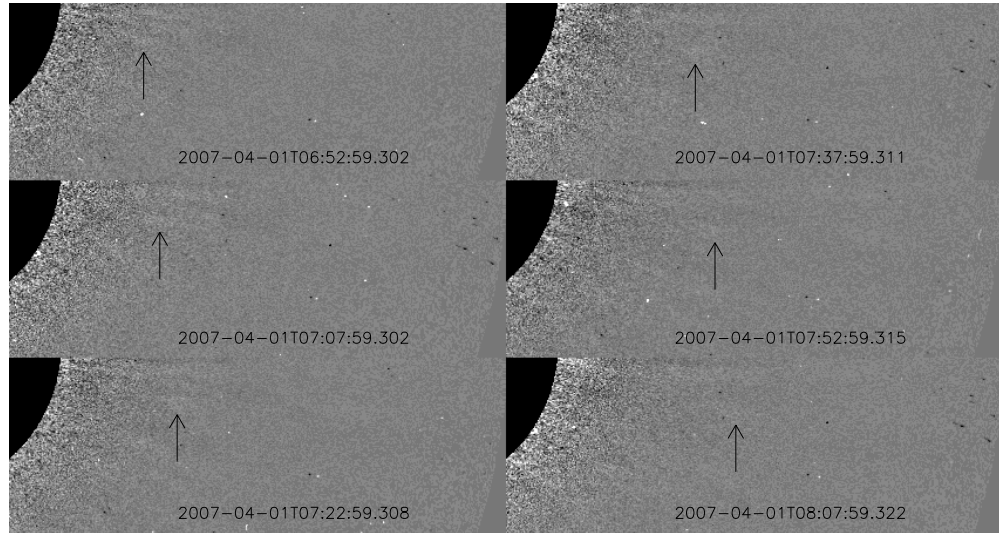


Figure 5.3: A blob seen in COR2 and its counterpart in COR1. The top image shows the feature in a COR2 image sequence (with some of the lower corona occluded). Bottom left shows a Radon-enhanced COR1 height-time image at 345° , and the bottom right a combined sequence of height measurements from both instruments. COR1 error bars represent an uncertainty of ± 6 radial pixels ($\sim 0.1 R_\odot$). COR2 error bars were estimated by repeated measurement. Both are comparable to or smaller than the symbol size. All images are from the Behind spacecraft.

measurement, and combined the measurements for those events into one. These combined events most likely represent features that either move non-radially from one angular bin to another, as some CMEs have been observed to do [82], or have angular widths greater than the five-degree bin size.

Occasionally a feature could be seen in the height-time image, but its height could not be reliably measured in more than two time steps. This typically happened because the trajectory was ambiguous due to noise or apparently overlapping features. These events were also excluded from the data set.

5.3 Results

After combining related events and excluding CMEs, a total of 434 upward-moving events were found in the 19 day period studied. Their height-time profiles were compared to both a line and a parabola using a least-squares fit, with an assumed uncertainty in every height measurement of seven pixels. Figure 5.4 shows the radial POS speed distribution of the events, as determined from the linear fits. The mean speed as measured in this fashion was 253 km s^{-1} .

The results of the parabolic fits divide the events into three groups: those with negative acceleration (89 features), those with positive acceleration (108 features), and those whose acceleration was smaller than the fit error (237 features). The top panel of figure 5.5 shows the radial POS acceleration distribution for the events with acceleration greater than the fit error. The mean acceleration for this set was 14 m s^{-2} . Of the events whose acceleration was measurably negative, all trajectories fit parabolas whose maximum height was within the COR1 FOV. This is most likely

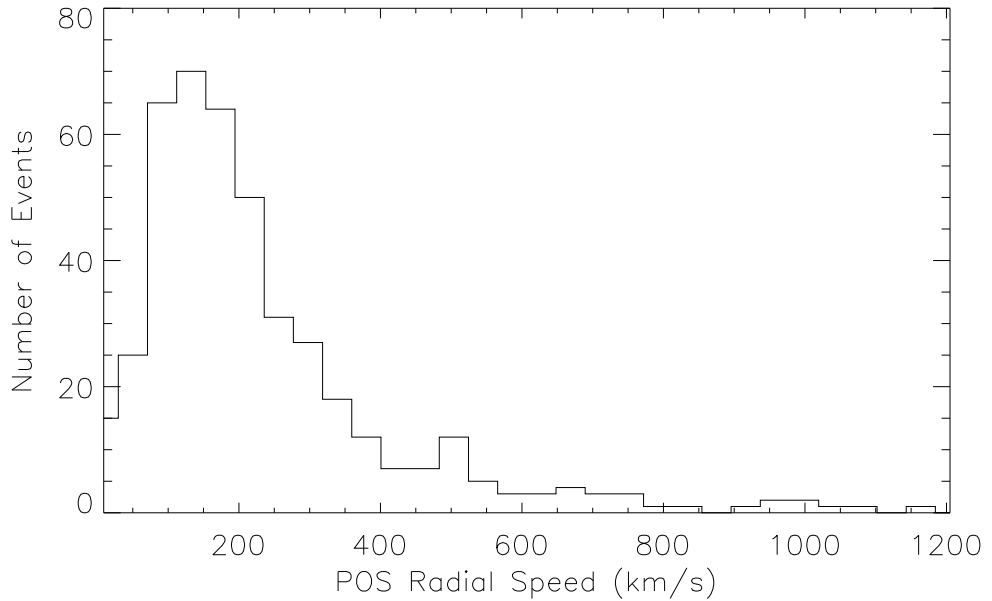


Figure 5.4: Distribution of event speeds from linear height-time fits.

because of the fairly large error bars, which limit the negative accelerations that can be measured to relatively large values.

Few events were visible all the way to the edge of the COR1 FOV and none were observed to reverse direction. I did not observe any downward-moving features during the days examined, consistent with previous observations that inflows are rarely seen during times of low solar activity [72, 71, 100].

Figure 5.6 shows the distribution of POS latitudes of the observed events. The measured distribution is consistent with the emergence of the events from near or within the streamer belt during the time periods studied.

To examine the relationship between the speed and height (POS altitude) of plasma blobs, Sheeley *et al.* [74] combined speed and height measurements of many observed blobs and fit the collection to two curves, one assuming constant

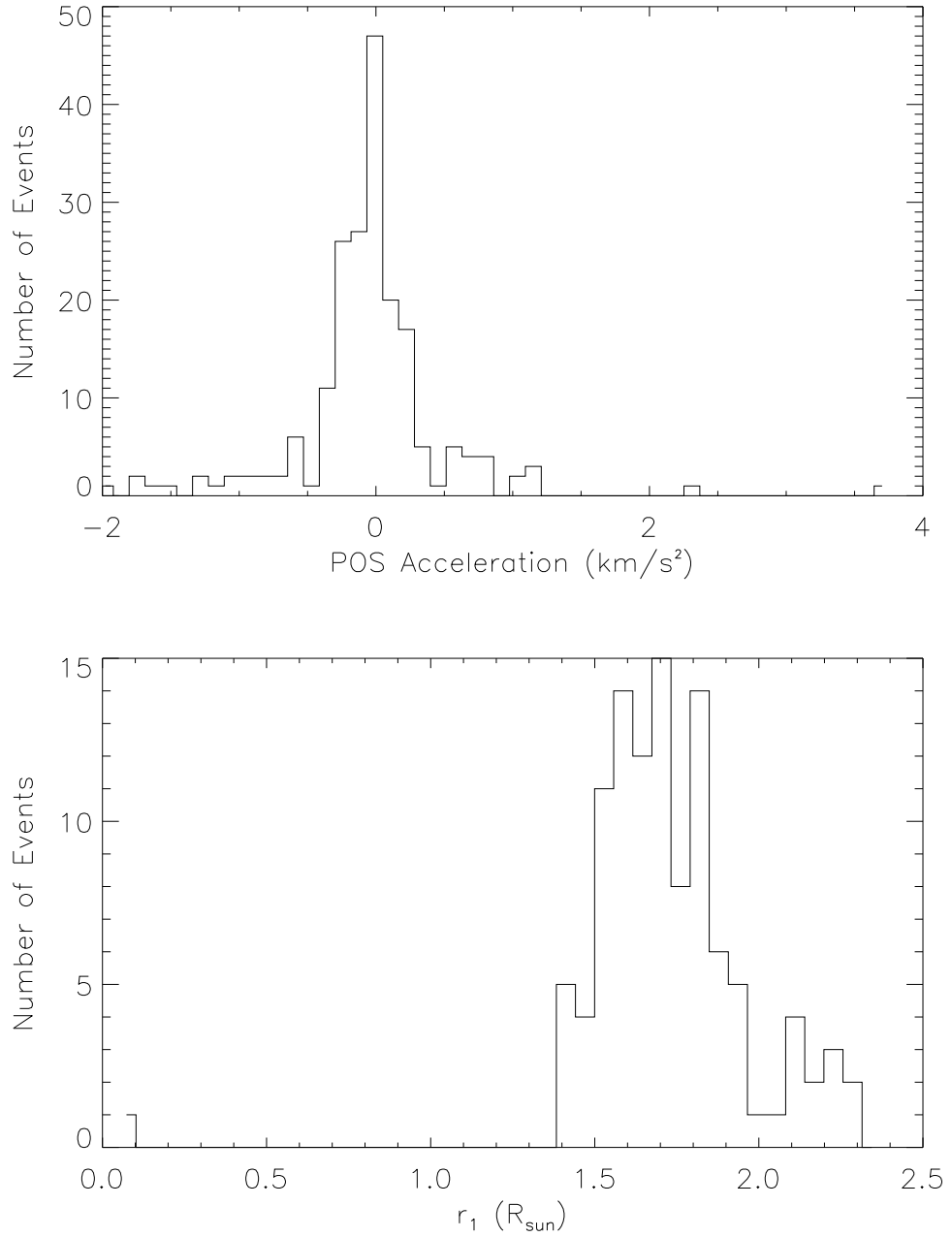


Figure 5.5: Top: Distribution of acceleration from parabolic fits with acceleration greater than the fit error. Bottom: Value of r_1 from equation 5.1 from events with positive acceleration greater than the fit error.

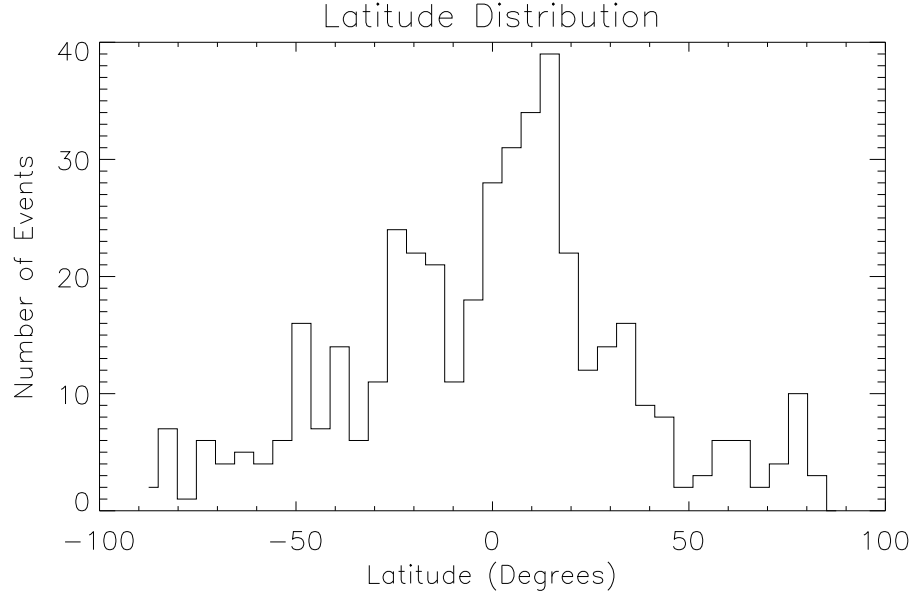


Figure 5.6: Latitudinal distribution of events.

acceleration and the other assuming an acceleration that decays exponentially with altitude. The dependence of the speed on the height in these two situations is given by:

$$v^2 = 2a(r - r_1) \quad (5.1)$$

and

$$v^2 = v_a^2(1 - e^{-\frac{r-r_1}{r_a}}) \quad (5.2)$$

respectively, where r_1 is the height at which the speed goes to zero and r_a is a length scale of the decay in the acceleration. Using equation 5.1 with all data points weighted equally, they obtain $r_1 = -0.4R_\odot$ and $a = 3.4 m s^{-2}$, and using equation 5.2 they obtain $v_a = 298.3 km s^{-1}$, $r_1 = 2.8R_\odot$, and $r_a = 8.1R_\odot$.

Because some of the observed COR1 features (particularly slow-moving ones) were detected in many more images than others, I fitted individual events to equa-

tion 5.1 rather than the entire collection; figure 5.5 shows the distribution of the parameters a , for events whose acceleration was greater than the fit error, and r_1 for events with positive acceleration greater than the fit error. (For events with negative acceleration r_1 represents the top of the trajectory, rather than the bottom.) It is interesting to note the small side-lobe on the right side of the distribution of r_1 . This may be an indication that the population of upward-moving features being studied here is in fact of two or more different origins (*e.g.* the population with r_1 above $2.0 R_\odot$ may be due to streamer pinch-off while that below may be due to footpoint exchanges) but with only 13 events above $2.0 R_\odot$ and no data below about $1.5 R_\odot$ it is also possible this is simply a statistical anomaly. The acceleration distribution does not seem to indicate two distinct populations of plasma blobs.

I also calculated the average speed as a function of height for the positive-acceleration events, shown in figure 5.7. Then I fit this data to equations 5.1 and 5.2. The fit to equation 5.1 gave the values $a = 12 \pm 5 \text{ m s}^{-2}$ and $r_1 = 1.3 \pm 1.0 R_\odot$, while the fit to equation 5.2 yielded $v_a = 160 \pm 50 \text{ km s}^{-1}$, $r_1 = 1.6 \pm 0.2 R_\odot$, and $r_a = 0.5 \pm 0.9 R_\odot$. The fits are shown in figure 5.7 along with the Sheeley *et al.* [74] fits for comparison. The fact that the fitted value of r_a is smaller than the uncertainty may be an indication that equation 5.2 is a bad model to describe the trajectories, or it may be the result of a bias in the data towards increased detection of low-speed events near the occulter edge; this second possibility might also explain the discrepancy between the fit to the COR1 data and that of Sheeley *et al.* (see section 5.4).

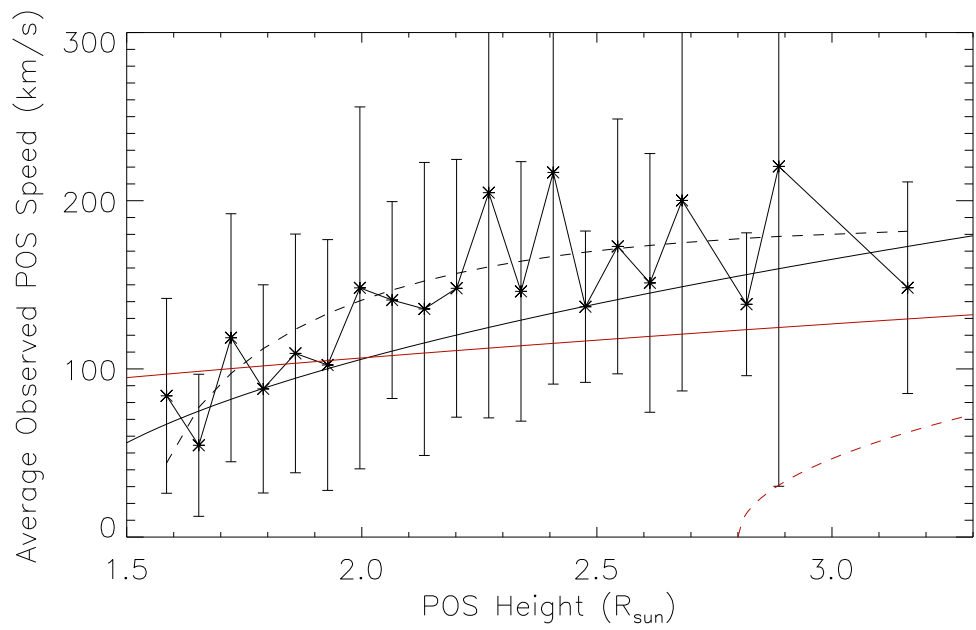


Figure 5.7: Average POS speed as a function of height for COR1 events with positive acceleration greater than the fit error, with error bars based on the standard deviation of events at that height. The solid black line shows a fit to equation 5.1 and the dashed black line shows a fit to equation 5.2. The red lines show fits to the same equations from Sheeley *et al.* [74].

5.4 Discussion and Conclusions

The observations above show that many events similar to the blobs seen by [74] are seen in the COR1 coronagraph at POS heights below those seen in the LASCO C2 coronagraph. I observe slight density enhancements with narrow angular extent moving away from the Sun, with trajectories consistent with those seen in the LASCO C2 coronagraph. A comprehensive search for plasma blobs was undertaken on 19 days' worth of COR1 data, resulting in 434 events.

The POS height-time profiles obtained from these measurements indicate speed and acceleration distributions which are reasonable for this region of the corona. The average speed measured here is slightly lower than those seen for CMEs in LASCO [30] even at solar minimum, but this is reasonable given that the events are measured at lower POS heights. The events are distributed in the POS in a manner consistent with an origin in or near the streamer belt.

These new observations provide further insight into the origin of the blobs. Based on fits to their data and the relative scarcity of observations below $3R_{\odot}$, Sheeley *et al.* [74] concluded that the blobs likely originate above the tops of streamers in the $3 - 4R_{\odot}$ range. Now, with the STEREO COR1 coronagraph, I have been able to make many additional observations between $1.5 - 3.5R_{\odot}$. The velocity profile of the events indicates a larger acceleration and a lower starting height for the density enhancements than measured by Sheeley *et al.* Also, the results are more consistent with a constant acceleration than those of [74], although this is probably due to the fact that COR1 samples a much smaller range of heights than C2 and

C3.

Sheeley *et al.* [74] observed a higher percentage of low-speed events in the $2 - 3R_{\odot}$ range than were seen in this study. Indeed, they detected a wide range of speeds in this altitude range (approximately $0 - 200 \text{ km s}^{-1}$), while in this study there were more low-speed events in the $1.5 - 2.0R_{\odot}$ POS height range.

It is possible that the cluster of low-speed events is detected at a lower altitude in the COR1 data because the COR1 FOV extends lower than the C2 FOV. The signal-to-noise ratio of any coronagraph is highest near the occulter, so one might expect more events from outside the POS to be visible there. Apparent speeds of blobs outside the POS are artificially low because their trajectories are seen in projection, which may explain why Sheeley *et al.* saw a cluster of low-speed events between $2 - 3.5 R_{\odot}$ (near the edge of the C2 occulter) while in this study we did not. The fact that the features are observed in difference images in both studies could also contribute to an increased prevalence of slow-moving features near the respective occulters, since low-speed features can be difficult to see in difference images and will show up best where the signal-to-noise ratio is highest. This difference between the two studies likely explains why the Sheeley *et al.* [74] fit to equation 5.2 does not match the COR1 data very well.

The observation of these blobs in the COR1 FOV provides a valuable insight into their origin, and hence to their suitability as a solar wind tracer. The shift of the low-speed events to lower altitudes with the use of a lower FOV telescope suggests that they may not originate primarily in the $3 - 4 R_{\odot}$ range as previously thought. This lends some support to the idea that at least some of these events may

be the result of footpoint exchanges between closed and open field lines, rather than magnetic reconnection at the tops of streamers.

To summarize, the main conclusions of this study are as follows:

1. I observe 434 upward-traveling density enhancements during the 19 days of COR1 data studied.
2. The latitudinal distribution of these events is consistent with an origin in or near the streamer belt, as was the case for the plasma blobs identified by Sheeley et al. [74].
3. The speeds and accelerations observed for the COR1 features are consistent with the observations by Sheeley and co-workers, except that using the COR1 coronagraph I see many more events at POS heights below $3 R_{\odot}$ and the cluster of low-speed events seen in the previous studies near $2.5 - 3.0 R_{\odot}$ is here seen near $1.5 - 2.0 R_{\odot}$.
4. The observation of a substantial number of plasma blobs below $2.5 R_{\odot}$ are not consistent with the idea that plasma blobs are the product of magnetic reconnection at the top of the streamer belt. While it is still possible that a number of blobs are generated above the streamer belt, a large portion of the events in this study originate below the streamer belt and are therefore more consistent with the footpoint exchange theory of blob origin.
5. The differences between this study and that of [74] suggest that there may be a bias towards the detection of low-speed events near the edge of the occulter, indicating that coronagraph measurements of plasma blobs may not be a

reliable tracer of solar wind speed near the bottom of the coronagraph FOV.

Chapter 6

Conclusions and Future Work

In the next section I briefly summarize the main questions addressed in the thesis, section 6.2 and 6.3 give the main results of the rotation and blobs studies, respectively.

6.1 Summary of Questions Addressed

Chapters three and four addressed the difficulty of reliably measuring the rotation rate of the solar corona. While the photospheric rotation rate has been found to be highly dependent on the latitude, previous studies have indicated that the corona rotates almost rigidly at a rate near the photospheric equatorial rate [64]. The contrast between the photospheric and coronal rotation rates is puzzling given that coronal magnetic features are apparently connected to those in the photosphere. In this study I have used the COR1 coronagraphs to confirm the rigid rotation seen in previous coronagraph studies for time series data from the most recent solar minimum. I have also used comparison of the apparent longitudinal structures rotating at the measured rates, with coronal electron density reconstructions from SRT at $1.8R_{\odot}$, to investigate the possibility that the observed rigidity is an observational effect due to the optical thinness of the corona as suggested by [50, 49].

The radial dependence of the rotation rate has been generally found to be very small, with one study finding a slight decrease in the rotation rate between $2R_{\odot}$ (LASCO C1) and $2.5R_{\odot}$ (LASCO C2) [50] and another finding a slight decrease

between $1.15R_{\odot}$ and $1.3 - 1.5R_{\odot}$ [75], both gaps in conjunction with a transition from emission-line measurements to white-light measurements. Using the COR1 coronagraphs, whose FOV is between $1.4 - 4.0R_{\odot}$, I have investigated the radial dependence of the rotation rate in this region with a single white-light instrument. Another study using LASCO C1 [87, 86] observed an apparent contrast between the rotation rates of closed and open magnetic field regions, using the LASCO C1 telescope between $1.1R_{\odot}$ and $2.2R_{\odot}$. However, because the corona was much less axisymmetric during the minimum of solar cycle 23 than during the minimum of solar cycle 22, a discussion of the radial dependence of the rotation rate in terms of closed and open magnetic field regions is not possible for this data set.

Stenborg and coworkers [87, 86] also observed indications of a second, latitudinally dependent component of the rotation signal in the form of small pseudo-peaks on the sides of their main rotation peak. These pseudo-peaks were observed using the PDM method and were identified in emission line data from the LASCO C1 telescope. The authors used harmonic filtering to study the significance and latitudinal dependence of the pseudopeaks. In this study I have presented results of PDM analyses of STEREO COR1 white-light data from the recent solar minimum. I applied an alternative filtering method, using the longitudinal structures identified in the data series rather than a sinusoidal structure, to search for a second latitudinally-dependent rotating component.

Another interesting question regarding the rotation of the solar corona is related to the observation that magnetic features on the solar surface exhibit both differential and rigid rotation, depending on the sizes and/or lifetimes of the features

being measured (see [80] and reference therein). In previous coronagraph studies it has only been possible to study the rotation of solar features with lifetimes greater than one-half solar rotation, a minimum of about 13.5 days. In this study I have made the first attempt to measure coronal white-light features with lifetimes less than 1 day, including measurements at multiple longitudinal scale sizes.

In this thesis I have also presented results of trajectory measurements of upward-moving density enhancements observed in COR1. Sheeley and co-workers [74, 68, 61, 73, 72, 71, 70, 102, 100, 59] measured similar phenomena they refer to as plasma blobs in height-time images made from LASCO C2 and C3 images. They consider two likely origins for plasma blobs: as by-products of footpoint exchanges or as the result of pinching off (via magnetic reconnection) of distended streamer tips.

Sheeley et al. [74] presented measurements of the trajectories of many of these plasma blobs, which appeared to largely originate above $3.0R_{\odot}$, near the top of the streamer belt. Here I have presented measurements of similar phenomena from the COR1 FOV, including many which first appear below $2.0R_{\odot}$.

6.2 Summary of Rotation Results

Figure 6.1 shows a comparison of my single-spacecraft rotation rate measurements with some seminal studies of both photospheric and coronal rotation. The X's and squares are show FeXIV coronal measurements from Sime *et al.* [75] at a height of $1.15R_{\odot}$ in the years 1985 and 1977, respectively. The triangles show average white-light coronal measurements from Fisher and Sime [20] at $1.3 - 1.5R_{\odot}$

between 1965 and 1983. The dash-dot and dash-dot-dot lines show photospheric rotation rates from [34] and [77], respectively.

The previous coronal studies shown were both conducted using ground-based telescopes, with attendant irregularities in observational cadence. In addition the latitudinal resolution of the previous studies was lower, about 15° and the latitudinal variation is not generally as smooth as that seen in the plot (*e.g.* the northern hemisphere results shown here are in all cases smoother than those of the southern hemisphere for the same time periods). A later ground-based emission-line study by Altrock [1] (not shown) achieved latitudinal resolution of 3° and a smoother latitudinal dependence of the rotation rate for yearly data sets only by averaging over 26 years of data.

The results of the rotation measurements presented in this thesis can be summarized as follows:

1. The coronal rotation during 2007 and 2008 was found to be almost independent of latitude for the range of latitudes in which a measurable rotation period was identified (approximately 45° N - 50° S at $1.8R_\odot$). The equatorial synodic rotation period was found to be 27.06 ± 0.08 days in 2007 and 26.97 ± 0.10 days in 2008.
2. For latitudes with measurable rotation periods using COR1 during 2008, the rotating longitudinal structure is similar to the average electron density reconstruction using SRT during that year, indicating that the measured rotational rigidity is not a result of projection effects.

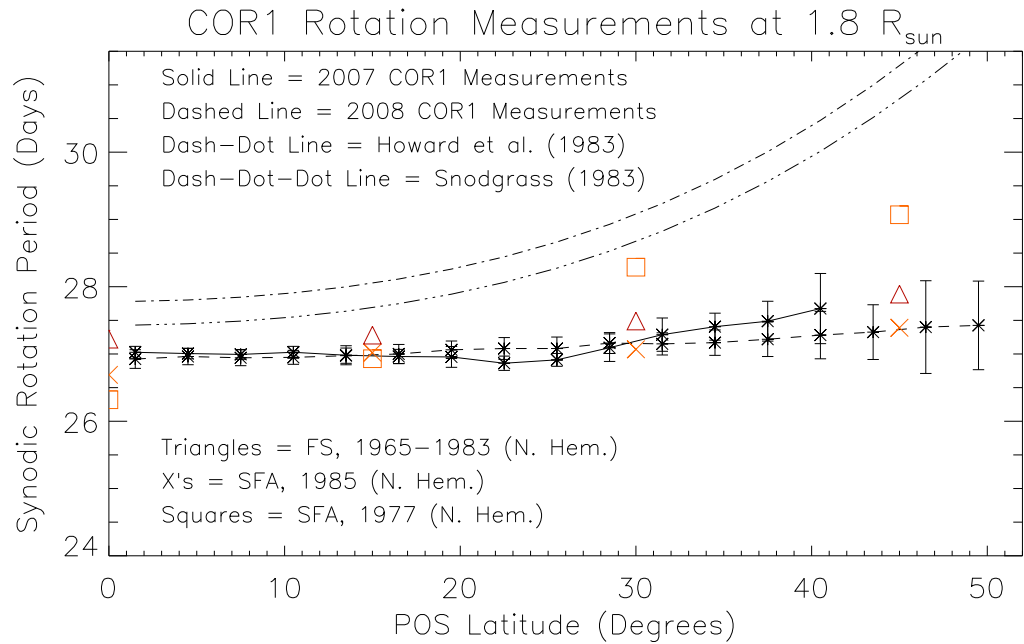


Figure 6.1: Comparison of coronal rotation measurements using COR1 coronagraphs in 2007 and 2008 with seminal studies of coronal and photospheric rotation. COR1 measurements from 2007 are shown as a solid line with asterisks, while the 2008 measurements are shown as a dashed line with triangles. The error bars shown represent the standard deviation of measurements from east and west limbs in the northern and southern hemispheres. The dash-dot line shows rotation rates from Doppler velocity measurements of photospheric plasma [34] and the dash-dot-dot line shows rates from cross-correlation of magnetograms [77]. The large X's (squares) show the results of northern hemisphere, FeXIV coronal measurements in 1985 (1977) [75]. The large triangles show ground based white-light coronal rotation measurements from Fisher and Sime [20].

3. The rotation period does not seem to show any dependence on radial (POS) distance during 2007 and 2008. The main difference between measurements at radii of 1.8, 2.2, 2.8, and $3.2R_{\odot}$ is that as the radial distance increases the range of latitudes over which the rotation signal is strong decreases from approximately 45° N - 50° S at $1.8R_{\odot}$ to approximately 30° N - 40° S at $3.2R_{\odot}$.
4. Secondary pseudo-peaks similar to those identified by Stenborg and co-workers [86, 87] were seen in some but not all PDM curves from the time periods studied. Upon subtracting the average longitudinal structure from the time series, the pseudo-peaks showed no consistent latitudinal dependence. This may be an indication that the emission-line signal shows more latitudinal dependence than the white-light signal, or it may reflect a difference in instrument sensitivity, filtering method, coronal configuration, or coronal behavior during the time periods examined.
5. Attempts to measure the short time lag rotation period resulted in unexpectedly low values at all latitudes, with an unexpected decrease in the rotation period with increasing latitude. These results are inconsistent with all prior measurements in either the corona or the photosphere and most likely reflect contamination of the cross-correlation signal by events that happen simultaneously or nearly simultaneously in the two STEREO spacecraft.
6. Attempts to cross-correlate features from the Ahead and Behind COR1 time series at various large longitudinal scales produced irregular results between

21 and 28 days, again with a tendency towards lower rotation period at higher latitudes, probably due to lower longitudinal resolution of pB measurements at higher latitudes.

7. The small longitudinal scale cross-correlation seemed to be dominated by noise, suggesting that the short time lag cross-correlation method is not appropriate for this data set.

6.3 Summary of Plasma Density Enhancement Results

The main results of the upward-moving plasma density enhancement study of chapter 5 are the following:

1. I observe 434 upward-traveling density enhancements during the 19 days of COR1 data studied.
2. The latitudinal distribution of these events is consistent with an origin in or near the streamer belt, as was the case for the plasma blobs identified by Sheeley et al. [74].
3. The speeds and accelerations observed for the COR1 features are consistent with the observations by Sheeley and co-workers, except that using the COR1 coronagraph I see many more events at POS heights below $3R_{\odot}$ and the cluster of low-speed events seen in the previous studies near $2.5 - 3.0R_{\odot}$ is here seen near $1.5 - 2.0R_{\odot}$.
4. The observation of a substantial number of plasma blobs below $2.5R_{\odot}$ are not consistent with the idea that plasma blobs are the product of magnetic reconnection at the top of the streamer belt. While it is still possible that a

number of blobs are generated above the streamer belt, a large portion of the events in this study originate below the streamer cusps and are therefore more consistent with the footpoint exchange theory of blob origin.

5. The differences between this study and that of [74] suggest that there may be a bias towards the detection of low-speed events near the edge of the occulter, indicating that coronagraph measurements of plasma blobs may not be a reliable tracer of solar wind speed near the bottom of the coronagraph FOV.

6.4 Future Work

The work presented in this thesis still leaves a great many questions unanswered. For example, the rotation rates measured in chapter 3 extend over a modest range of latitudes in comparison to some previous multi-decade studies, which found interesting results over higher-latitude regions. The most likely reason that the high-latitude regions in this study didn't show measurable rotation signal is that the weak COR1 signal in these regions is too heavily influenced by the background subtraction, as is common at solar minimum. It would be interesting to revisit those previous studies and attempt to measure the longitudinal structure of the underlying coronal features, in order to establish whether or not they are unduly influenced by projection of lower latitude features into high-latitude image bins.

It would also be interesting to conduct a comparative study of the STEREO Extreme Ultraviolet Imager (EUVI) data from these same time periods. As mentioned above, previous studies have shown slight but consistent differences between rotation rates measured using the FeXIV emission line and using white-light obser-

vations [75, 50]. Sime et al. suggested the slight difference they observed might be due to the differential rotation of local heating centers; coronal emission intensity is affected by temperature while white-light intensity is not. In the past, unocculted instruments that measure coronal emission have typically had insufficient sensitivity for off-limb rotation measurements (which would not be affected by the height ambiguity mentioned in chapter 4); however wavelet image processing techniques recently applied to the EUVI data set promise improved off-limb resolution. In addition, the EUVI data are available in multiple wavelengths and at higher spatial resolution than provided by COR1. Additionally, it may be possible to include spectroscopic data from Atmospheric Imaging Assembly (AIA), an instrument on the recently launched Solar Dynamics Observatory (SDO), to add a third vantage point beginning in 2010.

An investigation into the difference in the latitudinal dependence of pseudo-peaks investigated here and by Stenborg et al. [86, 87] would also be interesting. Unfortunately the LASCO C1 telescope used by Stenborg et al. was no longer functioning during the 2008/2009 solar minimum, so a comparison of results from this instrument and the COR1 coronagraphs during the same time period is not possible. However, there are ground-based FeXIV measurements available that span the two minima and could possibly be used to compare the emission-line and white-light rotation periods, with the hope of learning about the rotation of local heating centers.

The dual-spacecraft rotation measurements revealed a surprisingly high correlation between Ahead and Behind data at small time lags. It's not clear yet how

much of this correlation is due to impulsive events in the corona that occur simultaneously and how much of it may be due to longitudinal motion of coronal features, that we have neglected in this study. A more thorough investigation of the non-rotational correlation would be interesting and might make it possible to account for the correlation bias seen in the measurements of chapter 4.

Another question raised during this work concerns the extension of the density enhancement observations to greater numbers of events and to greater POS heights. During the initial study I focused on just a few short time periods when the corona was relatively quiet, in order to avoid false detections due to CMEs and related phenomena. With the increased data now available from the second half of 2008 and all of 2009, when the corona was exceptionally quiet, it should be possible to make many more additional observations. With these additional observations it would be possible to determine the significance of the interesting side-lobe in the distribution of figure 5.5.

Also, better inter-calibration and alignment of the COR1 and COR2 telescopes (along with increased numbers of observations) may now allow for the extension of more trajectories seen in COR1 into the COR2 FOV. This would help determine the precise relationship between the COR1 density enhancements and the C2/C3 plasma blobs - whether they are one and the same or whether they are perhaps related phenomena as was suggested by the anonymous referee of [40].

I look forward to exploring some of these still open questions as well as many others in the years to come.

Appendix A

An Overview of Solar Rotational Tomography

Solar rotational tomography (SRT) attempts to determine the three-dimensional electron distribution in the solar corona by taking advantage of solar rotation to acquire a series of images of the corona from different angles [46, 21, 22]. In chapter 3 I compare the average longitudinal structure determined from my rotation period measurements in 2008 to an average 2008 SRT electron density reconstruction. In this appendix I will give a basic description of how SRT works.

A.1 Electron Density from Coronagraph Images

As described in chapter 2, the pB signal scattered towards an observer from a point P in the corona is given by equation A.1:

$$pB = I_{tan} - I_{rad} = \frac{I_0 \pi \sigma}{2} N_e \sin^2 \chi [(1 - u)A + uB] \quad (\text{A.1})$$

where

$$A = \cos \Omega \sin^2 \Omega \quad (\text{A.2})$$

$$B = -\frac{1}{8} \left[1 - 3 \sin^2 \Omega - \frac{\cos^2 \Omega}{\sin \Omega} (1 + 3 \sin^2 \Omega) \ln \frac{1 + \sin \Omega}{\cos \Omega} \right] \quad (\text{A.3})$$

and where I_0 is the photospheric intensity at Sun center, σ is the Thomson cross section, N_e is the electron density at P, Ω is the angle shown in figure A.1, and u is an empirically measured constant that accounts for limb darkening [10].

The intensity measured by a particular pixel i in a coronagraph image is the

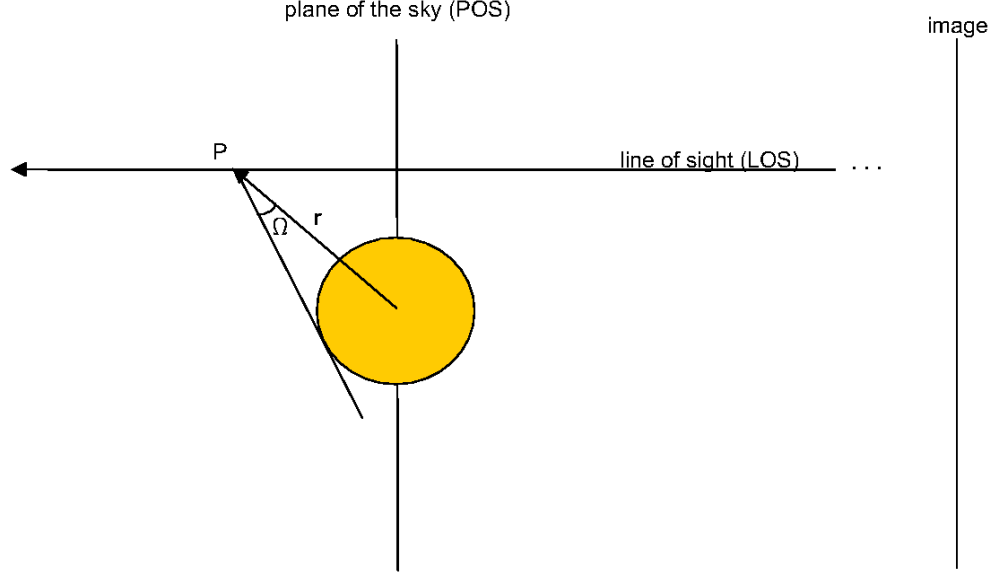


Figure A.1: Illustration showing the coronal white-light scattering geometry.

integrated pB signal scattered by electrons all along its LOS:

$$I_i = \int pB_{\mathbf{r}} d\mathbf{r} = \frac{I_0 \sigma \pi}{2} \int N_e(\mathbf{r}) \sin^2 \chi(\mathbf{r}) [(1 - u)A(\mathbf{r}) + uB(\mathbf{r})] d\mathbf{r} \quad (\text{A.4})$$

where A and B are as in equations A.2 and A.3 with Ω replaced by $\Omega(\mathbf{r})$.

Determining the three-dimensional coronal electron distribution from two-dimensional pB images requires inversion of equation A.4. Given the observed pB intensity, one must determine how the electrons that scattered the light to that pixel are distributed along the pixel's LOS. With only a single image this is an impossible problem, as there are infinitely many ways to distribute the scattering electrons that are consistent with the measured intensity. However, determination of the electron density can be made possible by combining multiple images from sufficiently different points of view, with intersecting LOSs. This is the basic idea of tomography (see [56] for a more general discussion of tomography).

Figure A.2 shows a 2-dimensional illustration of the coronal tomography problem. Three 1-dimensional sensor arrays measure the scattered coronal light from different angles. Their LOSs overlap in a circular region around the sun. (Note that in SRT, these three images are all taken by the same instrument over the course of several days, while the sun rotates past it.) If we subdivide the area of overlap of the images into smaller areas called voxels ¹ where the density is assumed to be approximately constant, then equation A.4 can be re-written:

$$I_i = \sum_{j=1}^N A_{ij} N_j + n_i \quad (\text{A.5})$$

where A_{ij} contains the approximate scattering coefficients for light scattered from voxel j towards pixel i , N_j is the electron density in voxel j , and n_i is an unknown noise contribution for each pixel i .

A.2 Solution By Functional Minimization

The system of equations formed by combining a set of intensity measurements I_i can be written in matrix form as:

$$\mathbf{I} = \mathbf{A}\mathbf{N} + \mathbf{n} \quad (\text{A.6})$$

and the problem is how to determine \mathbf{N} from \mathbf{I} . This equation seldom if ever has a unique solution in application. Typically in SRT many more voxels are used than pixels, for several reasons, among them the need for sufficient resolution that the density inside each voxel is approximately constant, the need to have scattering

¹Normally the word pixel is used for area elements and voxel is reserved for volume elements; however, lacking a good word for the linear elements of the sensor arrays in this example, I borrow the word voxel rather than use “pixel” to refer to both 2-dimensional reconstruction cells and 1-dimensional sensors.

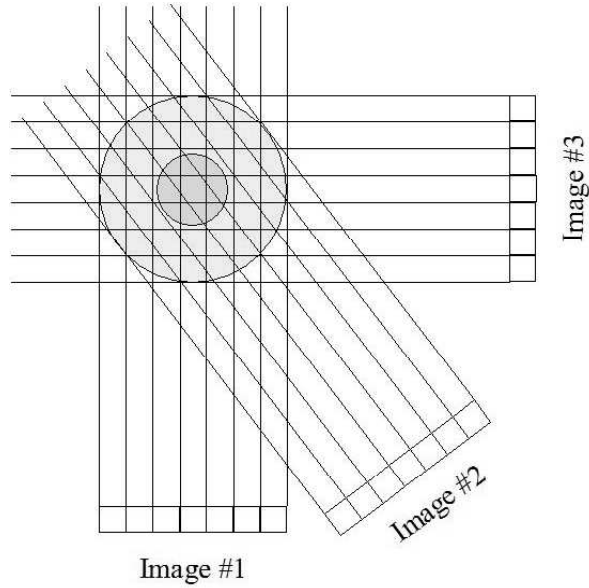


Figure A.2: A two-dimensional analog of SRT. Three one-dimensional pixel arrays view a two dimensional sun and corona from different perspectives. The combined information from the three images can be used to estimate the electron density within the area of overlap.

coefficients relatively consistent over the scale of one voxel, and the need for the reconstruction result to have sufficient resolution to be of scientific interest. For this reason, solving the system of equations A.6 requires the use of *a priori* constraints on the reconstruction result. In coronal applications the standard constraint is that the coronal density is expected to vary smoothly between neighboring voxels; the solution resulting from such a constraint is said to be regularized.

Since the best that can be hoped for is an *optimal* agreement between the theoretical and observed intensities, the coronal electron density is usually taken to be the \mathbf{N} that minimizes a functional of the form:

$$\Phi(\mathbf{N}) = \Psi(\mathbf{A}\mathbf{N} - \mathbf{I}) + \mu\Upsilon(\mathbf{R}\mathbf{N}) \quad (\text{A.7})$$

where \mathbf{R} measures in some way the “roughness” of the density vector \mathbf{N} and Ψ and

Υ can be simple functions like magnitude or magnitude squared, or special functions like the Huber function which minimize the impact of extreme data values. The first term in equation A.7 penalizes the reconstructed vector \mathbf{N} for being inconsistent with the observational data, while the second penalizes it for violating the *a priori* assumption that the density varies smoothly. The parameter μ determines the balance between the two competing goals of data fidelity and regularization.

Kramar et al. [46] have described in detail the specific method used to create the electron density distributions used in section 3.6. Here is a brief list of items to keep in mind when using SRT data:

1. Because coronal reconstructions are based on a set of images taken over the course of ~ 14 days, changes in the corona that happen on timescales shorter than this are neglected and introduce some error, but it is still possible to obtain reasonably good reconstructions of the global structure of the corona, as shown by [46, 21, 22, 23]. As the SRT results used in this study are averaged over the course of an entire year, only the most stable coronal features are well represented; however, this is also the case for the longitudinal structure to which the SRT results are being compared in chapter 3.
2. SRT also assumes that the rotation of the corona is rigid. According to the measurements in section 3.5 the 2008 corona rotated very rigidly, making this an optimal time for tomographic reconstruction.
3. The latitude of the observing spacecraft in the SRT reconstructions of Kramar et al. are assumed to be zero for computational efficiency. This introduces some

error in the determination of A . However, as long as the actual spacecraft latitudes are small relative to the vertical size of the voxels, this error should not be large, and over the course of a year it should approximately average out.

4. The pixel LOSs theoretically extend to infinity; in SRT they are assumed to terminate at the edge of the reconstruction volume. This is generally a reasonable assumption given that the coronal density falls off with distance from the sun approximately as $r^{-2.5}$ (see [10] and references therein), and that the pB signal for a given density decreases with distance from the plane of the sky as can be seen in equation A.1. However, from inspection of figure A.2 one can see that this assumption is most accurate for pixels near the center of the images, where a larger portion of the LOS is in the reconstruction region. The results of Kramar et al. [46] do show an unexpected increase in the electron density near the edge of the reconstruction region due to contributions to the image intensity from material outside the reconstruction region, however this is unlikely to have much effect on the reconstruction near $1.8R_{\odot}$ where I compare it to my results.

None of these important limitations of SRT appear to effect its suitability for use in this study.

Appendix B

Cross-Correlation of STEREO Ahead and Behind Time Series

In this appendix I describe the two methods I use to approximate the cross-correlation of STEREO Ahead and Behind time series in chapter 4. In an ideal experiment, the observing spacecraft would rotate around the sun at a constant speed, so that the solar meridian defined by the east (or west) limb in each coronagraph's POS would be a constant function of time. Then if one picked out a pixel in the Ahead spacecraft images and the corresponding pixel in the Behind spacecraft images, the two should see roughly the same coronal material, separated by a constant lag in time. The cross-correlation, given by:

$$P_{AB}(L) = \frac{\sum_{i=1}^{N-L} (B_{i+L} - \bar{B})(A_i - \bar{A})}{\sqrt{\sum_{i=1}^N (A_i - \bar{A})^2 \sum_{i=1}^N (B_i - \bar{B})^2}} \quad (\text{B.1})$$

could be used to determine the sidereal rotation period:

$$\tau_{sidereal} = \frac{2\pi L_{max} \Delta t}{\Delta\Theta} \quad (\text{B.2})$$

where Δt is the time between observations, $\Delta\Theta$ is the angular separation between the two spacecraft, and L_{max} is the value of L at which $P_{AB}(L)$ assumes a maximum. Unfortunately, the STEREO spacecraft trajectories have irregular orbital speeds, so that the POS meridian is not a constant function of time.

I use two methods to get over this obstacle. In the first method I interpolate both time series at even values of the quantity $\delta_\tau(t) = \omega_0 t \pm \Lambda_{COR1}(t)$ introduced in chapter 3, where $\omega_0 = \frac{2\pi}{\tau}$ is the assumed rotation frequency and

$\Lambda_{COR1}(t)$ is the angular separation between the spacecraft and Earth. The quantity δ_τ can be thought of as representing the longitude of the POS meridian (for one limb), assuming a coronal rotation period of τ ; it differs only in that it is reversed in time and offset by a constant.

Once I have interpolated both time series for a particular value of τ , I calculate the sample correlation coefficient for the interpolated series, $r(\tau)$. By repeating this process for a number of τ values I can construct $C(\tau)$, the approximate cross-correlation as a function of the rotation period.

The second method is slightly more complex, but the goal is the same: a function $C(\tau)$ showing the correlation as a function of the rotation period. This method does not require interpolation of the time series.

Consider the individual data points in each time series. Each value of A_i has an associated value of t_i , the time at which the observation was made, and Θ_i , the longitude of the spacecraft at that observation time. The same is true for each value B_j . This means that for each pair (i, j) of data points (A_i, B_j) I can define a separation in longitude $\Delta\Theta_{ij} = \Theta_{A,i} - \Theta_{B,j}$ and in time $\Delta t_{ij} = t_{A,i} - t_{B,j}$. From this I can calculate the coronal rotation period necessary for the same coronal feature to be observed in the two data points, $\tau_{ij} = \frac{2\pi\Delta t_{ij}}{\Delta\Theta_{ij}}$.

I define a set of nominal values for the rotation period, $T_n = T_{min} + n \Delta T$ where $0 \leq n \leq M$. Then for each T_n I identify the set of data indices $\{i, j\}$ such that $T_n - \frac{\Delta T}{2} < \tau_{ij} < T_n + \frac{\Delta T}{2}$ and construct from this set two coupled vectors $(\mathbf{A}_n, \mathbf{B}_n)$. Then I calculate the correlation coefficient $P_{A_n B_n}$. Repeating this for each value of T_n , I can construct $C(T)$, an approximation for $C(\tau)$.

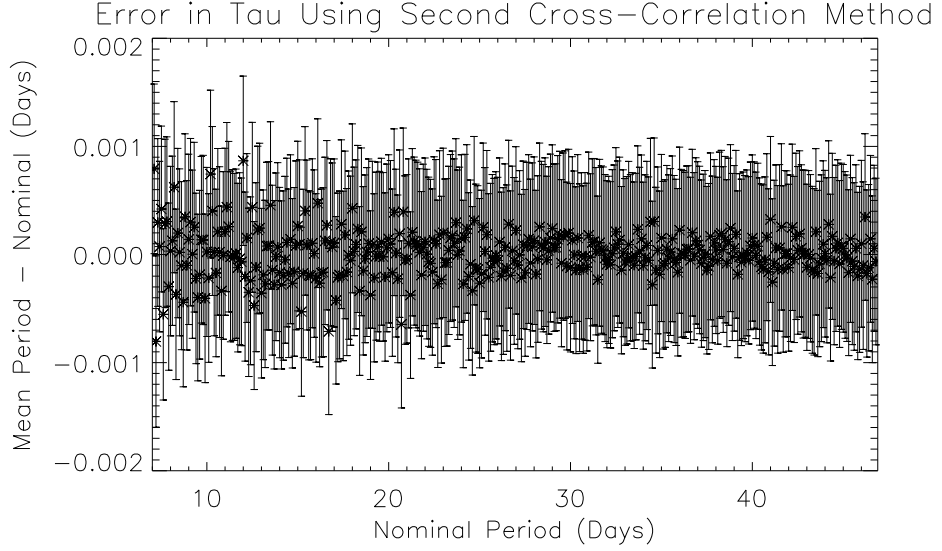


Figure B.1: The difference between $\bar{\tau}_n$ and the nominal period values T_n (see text). The first and last points fall outside plot range, but are between -0.003 and 0.003 , less than 0.043% error.

The first method introduces some accuracy due to the interpolation, while the second introduces some inaccuracy due to the fact that all the $\{i, j\}$ associated with a particular T_n represent slightly different *true* rotation periods τ_{ij} . In order to check the inaccuracy of the second method, I calculated $\bar{\tau}_n$ and σ_{τ_n} , the mean and standard deviation of the τ_{ij} values associated with each value of T_n . Figure B.1 shows the difference between the nominal T_n and $\bar{\tau}_n$ for all n for the time period chosen. The values chosen for T_{min} , M and ΔT were 7., 400, and 0.1, respectively. The difference between the nominal and mean values is less than 0.043% for all of values of n .

Appendix C

Contamination of Cross-Correlation Periodogram by Simultaneous Events

In chapter 4 and appendix B, I assert that if the two STEREO spacecraft had constant orbital speeds the rotation period could be determined by calculating:

$$\tau_{sidereal} = \frac{2\pi L_{max} \Delta t}{\Delta\Theta} \quad (\text{C.1})$$

where Δt is the time between observations, $\Delta\Theta$ is the longitudinal separation between the two spacecraft, and L_{max} is the value of L at which

$$P_{AB}(L) = \frac{\sum_{i=1}^{N-L} (B_{i+L} - \bar{B})(A_i - \bar{A})}{\sqrt{\sum_{i=1}^N (A_i - \bar{A})^2 \sum_{i=1}^N (B_i - \bar{B})^2}} \quad (\text{C.2})$$

assumes a maximum. This assertion is based on the assumption that coronal features seen in a particular pixel in COR1 Behind images will later rotate into the corresponding pixel in the Ahead images. In a sense, I am assuming the model

$$A_j = \alpha B_{j-L_p} + \epsilon_j \quad (\text{C.3})$$

$$B_j = \gamma B_{j-\tau_{sidereal}} + \eta_j \quad (\text{C.4})$$

for my time series, where L_p is the time lag between the features' appearance in the Behind POS and its appearance in the Ahead POS, α and γ are constants and ϵ_j and η_j are normally distributed, random variables.

As discussed in chapter 4, this model is inadequate in the sense that it does not account for the presence of simultaneous events in the data series. A somewhat

better model might be:

$$A'_j = \alpha B_{j-L_p} + \beta B_j + \epsilon_j \quad (\text{C.5})$$

$$B_j = \gamma B_{j-\tau_{sidereal}} + \eta_j \quad (\text{C.6})$$

where β is a constant.

With this new model, the cross-correlation function $P_{A'B}(L)$ becomes:

$$\begin{aligned} P_{A'B}(-L) &= \frac{1}{N\sigma_{A'}\sigma_B} \sum_{i=1}^{N-L} (A'_i - \bar{A}')(B_{i-L} - \bar{B}) \\ &= \frac{1}{N\sigma_{A'}\sigma_B} \sum_{i=1}^{N-L} (\alpha B_{i-L} + \beta B_i + \epsilon_i - (\alpha + \beta)\bar{B})(B_{i-L} - \bar{B}) \\ &= \frac{1}{N\sigma_{A'}\sigma_B} \left(\sum_{i=1}^{N-L} (A_i - \bar{A})(B_{i-L} - \bar{B}) + \sum_{i=1}^{N-L} \beta (B_i - \bar{B})(B_{i-L} - \bar{B}) \right) \\ &= \frac{\sigma_A}{\sigma_{A'}} (P_{AB}(-L) + \beta P_B(-L)) \end{aligned} \quad (\text{C.7})$$

where $P_B(L)$ is the lag- L autocorrelation (see equation 3.2) of the Behind time series. Assuming the model for B_j given in equation C.5, $P_B(-L)$ is approximately 1 for $L = m\tau_{sidereal}$ (where m is an integer), and has a magnitude less than 1 everywhere else.

The model relationship between the Ahead and Behind time series in equation C.5 is still deficient in two ways. First, the real Behind time series exhibits a small-lag autocorrelation that the model does not include (i.e. the model for B_j should probably include terms proportional to B_{j-1} , B_{j-2} , etc.) These neglected terms do not affect the results of the calculations in equation C.7, but do affect the shape of $P_B(-L)$, widening the autocorrelation peaks at $L = m\tau_{sidereal}$. The $m = 0$ peak may well be the source of the bias towards low rotation periods seen in the results

of chapter 4. Second, the parameter β of equation C.5 is not constant for the real time series, due to the increasing longitudinal separation of the two spacecraft and the impulsive, variable nature of coronal phenomena.

Bibliography

- [1] R. C. Altrock. A study of the rotation of the solar corona. *Solar Physics*, 213:23–37, 2003.
- [2] H. M. Antia and S. Basu. Temporal Variations of the Solar Rotation Rate at High Latitudes. *The Astrophysical Journal Letters*, 559:L67–L70, 2001.
- [3] E. Antonucci and M. A. Dodero. Rotation and lifetime of coronal features. *Solar Physics*, 62:107–112, 1979.
- [4] E. Antonucci and L. Svalgaard. Rigid and differential rotation of the solar corona. *Solar Physics*, 34:3–10, 1974.
- [5] M. J. Aschwanden. *Physics of the Solar Corona: An Introduction*. Praxis Publishing, Chichester, UK, 2004.
- [6] H. W. Babcock. The Topology of the Sun’s Magnetic Field and the 22-YEAR Cycle. *The Astrophysical Journal*, 133:572–587, 1961.
- [7] O. G. Badalyan. Two modes of the differential rotation of the solar corona. *Astronomy Reports*, 53(3):262–274, 2009.
- [8] O. G. Badalyan, V. N. Obridko, and J. Sykora. Cyclic variations in the differential rotation of the solar corona. *Astronomy Reports*, 50(4):312–324, 2006.
- [9] John G. Beck. A comparison of differential rotation measurements. *Solar Physics*, 191:47–70, 1999.
- [10] D. E. Billings. *A Guide to the Solar Corona*. Academic Press, New York, 1966.
- [11] J. Birn, J. F. Drake, M. A. Shay, B. N. Rogers, R. E. Denton, M. Hesse, M. Kuznetsova, Z. W. Ma, A. Bhattacharjee, A. Otto, and P. L. Pritchett. Geospace Environmental Modeling (GEM) magnetic reconnection challenge. *J. Geophys. Res.*, 106:3715–3720, March 2001.
- [12] R. Brajša, H. Wöhl, B. Vršnak, V. Ruždjak, F. Clette, J.-F. Hochedez, and D. Roša. Height correction in the measurement of solar differential rotation determined by coronal bright points. *Astronomy and Astrophysics*, 414:707–715, 2004.
- [13] G. E. Brueckner, R. A. Howard, M. J. Koomen, C. M. Korendyke, D. J. Michels, J. D. Moses, D. G. Socker, K. P. Dere, P. L. Lamy, A. Llebaria, M. V. Bout, R. Schwenn, G. M. Simnett, D. K. Bedford, and C. J. Eyles. The Large Angle Spectroscopic Coronagraph (LASCO). *Solar Physics*, 162:357–402, 1995.

- [14] L. F. Burlaga. MHD processes in the outer heliosphere. *Space Science Reviews*, 39:255–316, 1984.
- [15] A. dal Lago, R. Schwerin, G. Stenborg, and W. D. Gonzalez. Coronal mass ejection speeds measured in the solar corona using LASCO C2 and C3 images. *Advances in Space Research*, 32:2619–2624, 2003.
- [16] S. R. Davies. An improved test for periodicity. *Monthly Notices of the Royal Astronomical Society*, 244:93–95, 1990.
- [17] J. M. Davila. Solar Tomography. *Astrophysical Journal*, 423:871, 1994.
- [18] H. Q. Feng, D. J. Wu, and J. K. Chao. Size and energy distributions of interplanetary magnetic flux ropes. *Journal of Geophysical Research (Space Physics)*, 112(A11):2102, 2007.
- [19] J. A. Fessler. Penalized weighted least-squares image reconstruction for positron emission tomography. *IEEE Trans. Medical Imaging*, 13(2):290–300, 1997.
- [20] R. Fisher and D. G. Sime. Rotational characteristics of the white-light solar corona 1965-1983. *The Astrophysical Journal*, 287:959–968, 1984.
- [21] R. A. Frazin. Tomography of the solar corona i. a robust, regularized, positive estimation method. *The Astrophysical Journal*, 530:1026–1035, 2000.
- [22] R. A. Frazin and P. Janzen. Tomography of the solar corona. ii. robust, regularized, positive estimation of the three-dimensional electron density distribution from lasco-c2 polarized white-light images. *The Astrophysical Journal*, 570:408–422, 2002.
- [23] R. A. Frazin, P. Lamy, A. Llebaria, and A. M. Vásquez. Three-Dimensional Electron Density from Tomographic Analysis of LASCO-C2 Images of the K-Corona Total Brightness. *Solar Physics*, page 79, 2010.
- [24] S. L. Freeland and B. N. Handy. Data Analysis with the SolarSoft System. *Solar Physics*, 182:497–500, 1998.
- [25] A. H. Gabriel. A magnetic model of the solar transition region. *Royal Society of London Philosophical Transactions Series A*, 281:339–352, May 1976.
- [26] S. Giordano and S. Mancuso. Coronal Rotation at Solar Minimum from UV Observations. *The Astrophysical Journal*, 688:656–668, 2008.
- [27] S. Giordano, S. Mancuso, and M. Romoli. Latitudinal and Radial Variation of Solar Corona Rotation at Solar Minimum. In C. Dumitrache and N. A. Popescu, editor, *Flows, Boundaries, and Interactions*, volume 934 of *American Institute of Physics Conference Series*, pages 119–128, 2007.

- [28] L. Golub and J. M. Pasachoff. *The Solar Corona*. Cambridge University Press, Cambridge, U. K., 1997.
- [29] N. Gopalswamy. *A Global Picture of CMEs in the Inner Heliosphere*, volume 317 of *Astrophysics and Space Science Library*, page 201. Kluwer Academic Publishers, Dordrecht, The Netherlands, 2004.
- [30] N. Gopalswamy, S. Yashiro, G. Michalek, G. Stenborg, A. Vourlidas, S. Freeland, and R. Howard. The SOHO/LASCO CME Catalog. *Earth Moon and Planets*, 104:295–313, 2009.
- [31] R. T. Hansen, S. F. Hansen, and H. G. Loomis. Differential Rotation of the Solar Electron Corona. *Solar Physics*, 10:135–149, 1969.
- [32] H. Hara. Differential Rotation Rate of X-ray Bright Points and Source Region of their Magnetic Fields. *The Astrophysical Journal*, 697:980–984, 2009.
- [33] R. A. Harrison. The nature of solar flares associated with coronal mass ejection. *Astronomy and Astrophysics*, 304:585–594, 1995.
- [34] R. Howard, J. M. Adkins, J. E. Boyden, T. A. Cragg, T. S. Gregory, B. J. Labonte, S. P. Padilla, and L. Webster. Solar rotation results at Mount Wilson. *Solar Physics*, 83:321–338, 1983.
- [35] R. Howard, P. I. Gilman, and P. A. Gilman. Rotation of the sun measured from Mount Wilson white-light images. *The Astrophysical Journal*, 283:373–384, 1984.
- [36] R. Howard and J. Harvey. Spectroscopic Determinations of Solar Rotation. *Solar Physics*, 12:23–51, 1970.
- [37] R. A. Howard, D. J. Michels, N. R. Sheeley, Jr., and M. J. Koomen. The observation of a coronal transient directed at earth. *The Astrophysical Journal Letters*, 263:L101–L104, 1982.
- [38] B. Inhester, G. Stenborg, R. Schwenn, N. Srivastava, and B. Podlipnik. LASCO FeXIV and FeX observations of the solar coronal rotation during the recent solar activity minimum. In S. R. Habbal, R. Esser, J. V. Hollweg, & P. A. Isenberg, editor, *American Institute of Physics Conference Series*, volume 471 of *American Institute of Physics Conference Series*, pages 297–300, 1999.
- [39] J. Javaraiah and M. H. Gokhale. *The Sun's Rotation*. Nova Science Publishers, Inc., New York, 2002.
- [40] S. I. Jones and J. M. Davila. Localized Plasma Density Enhancements Observed in STEREO COR1. *The Astrophysical Journal*, 701:1906–1910, 2009.

- [41] M. L. Kaiser, T. A. Kucera, J. M. Davila, O. C. St. Cyr, M. Guhathakurta, and E. Christian. The STEREO Mission: An Introduction. *Space Science Reviews*, 136:5–16, 2008.
- [42] M.-B. Kallenrode. *Space physics : an introduction to plasmas and particles in the heliosphere and magnetospheres*. Springer-Verlag, 2004.
- [43] N. Karachik, A. A. Pevtsov, and I. Sattarov. Rotation of Solar Corona from Tracking of Coronal Bright Points. *The Astrophysical Journal*, 642:562–567, 2006.
- [44] H. Kimura and I. Mann. Brightness of the solar F-corona. *Earth, Planets, and Space*, 50:493–499, 1998.
- [45] R. W. Komm, R. F. Howard, and J. W. Harvey. Rotation rates of small magnetic features from two- and one-dimensional cross-correlation analyses. *Solar Physics*, 145:1–10, 1993.
- [46] M. Kramar, S. Jones, J. Davila, B. Inhester, and M. Mierla. On the Tomographic Reconstruction of the 3D Electron Density for the Solar Corona from STEREO COR1 Data. *Solar Physics*, 259:109–121, 2009.
- [47] B. J. Labonte and R. Howard. Solar rotation measurements at mount wilson. iii - meridional flow and limbshift. *Solar Physics*, 80:373–378, 1982.
- [48] R. B. Leighton. Transport of Magnetic Fields on the Sun. *Astrophysical Journal*, 140:1547–1562, 1964.
- [49] D. J. Lewis and G. M. Simnett. Lasco observations of the coronal rotation and morphology of tracers seen at solar maximum and comparison with solar minimum. *Solar Physics*, 200:75–89, 2001.
- [50] Lewis, D. J. and Simnett, G. M. and Brueckner, G. E. and Howard, R. A. and Lamy, P. L. and Schwenn, R. Lasco observations of the coronal rotation. *Solar Physics*, 184:297–315, 1999.
- [51] A. F. Linnell Nemeč and J. M. Nemeč. A test of significance for periods derived using phase-dispersion-minimization techniques. *Astronomical Journal*, 90(11):2317–2320, 1985.
- [52] B. Lyot. The study of the solar corona and prominences without eclipses (George Darwin Lecture, 1939). *Monthly Notices of the Royal Astronomical Society*, 99:580, 1939.
- [53] C. H. Mandrini, S. Pohjolainen, S. Dasso, L. M. Green, P. Demoulin, L. van Driel-Gesztelyi, C. Copperwheat, and C. Foley. Interplanetary flux rope ejected from an X-ray bright point: The smallest magnetic cloud source-region ever observed. *Astronomy and Astrophysics*, 434:725–740, 2005.

- [54] M. B. Moldwin, S. Ford, R. Lepping, J. Slavin, and A. Szabo. Small-scale magnetic flux ropes in the solar wind. *Geophysical Research Letters*, 27(1):57–60, 2000.
- [55] A. G. Nash. Rotation of the sun’s outer white-light corona determined from SOLWIND data. *The Astrophysical Journal*, 366:592–598, 1991.
- [56] F. Natterer. *The Mathematics of Computerized Tomography*. John Wiley & Sons Ltd., 1986.
- [57] H. W. Newton and M. L. Nunn. The Sun’s rotation derived from sunspots 1934-1944 and additional results. *Monthly Notices of the Royal Astronomical Society*, 111:413, 1951.
- [58] A. K. Pierce and J. C. Lopresto. Solar rotation from a number of Fraunhofer lines. *Solar Physics*, 93:155–170, 1984.
- [59] E. Robbrecht. *New techniques for the characterisation of dynamical phenomena in solar coronal images*. PhD thesis, Royal Observatory of Belgium, 2007.
- [60] E. Robbrecht and D. Berghmans. Automated recognition of coronal mass ejections (cmes) in near-real-time data. *Astronomy and Astrophysics*, 425:1097–1106, 2004.
- [61] E. Robbrecht, D. Berghmans, and R. A. M. Van der Linden. Automated LASCO CME Catalog for Solar Cycle 23: Are CMEs Scale Invariant? *The Astrophysical Journal*, 691:1222–1234, 2009.
- [62] D. Rosa, B. Vrsnak, H. Bozic, R. Brajsa, V. Ruzdjak, A. Schroll, and H. Wohl. A Method to Determine the Solar Synodic Rotation Rate and the Height of Tracers. *Solar Physics*, 179:237–252, 1998.
- [63] J. D. Scargle. Studies in astronomical time series analysis. III - Fourier transforms, autocorrelation functions, and cross-correlation functions of unevenly spaced data. *Astrophysical Journal*, 343:874–887, 1989.
- [64] E. H. Schroter. The solar differential rotation: Present status of observations. *Solar Physics*, 100:141–169, 1985.
- [65] A. Schwarzenberg-Czerny. On the advantage of using analysis of variance for period search. *Monthly Notices of the Royal Astronomical Society*, 241:153–165, 1989.
- [66] A. Schwarzenberg-Czerny. The distribution of empirical periodograms: Lomb-Scargle and PDM spectra. *Monthly Notices of the Royal Astronomical Society*, 301:831–840, 1998.
- [67] R. Schwenn. Solar wind sources and their variations over the solar cycle. *Space Science Reviews*, 124:51–76, 2006.

- [68] N. R. Sheeley, Jr., D. D.-H. Lee, K. P. Casto, Y.-M. Wang, and N. B. Rich. The structure of streamer blobs. *The Astrophysical Journal*, 694:1471–1480, 2009.
- [69] N. R. Sheeley, Jr., A. G. Nash, and Y.-M. Wang. The origin of rigidly rotating magnetic field patterns on the sun. *The Astrophysical Journal*, 319:481–502, 1987.
- [70] N. R. Sheeley, Jr., J. H. Walters, Y.-M. Wang, and R. A. Howard. Continuous tracking of coronal outflows: Two kinds of coronal mass ejections. *Journal of Geophysical Research*, 104(A11):24739–24767, 1999.
- [71] N. R. Sheeley, Jr. and Y.-M. Wang. Coronal inflows and sector magnetism. *The Astrophysical Journal*, 562:L107–L110, 2001.
- [72] N. R. Sheeley, Jr. and Y.-M. Wang. Characteristics of coronal inflows. *The Astrophysical Journal*, 579:874–887, 2002.
- [73] N. R. Sheeley, Jr. and Y.-M. Wang. In/out pairs and the detachment of coronal streamers. *The Astrophysical Journal*, 655:1142–1156, 2007.
- [74] N. R. Sheeley, Jr., Y.-M. Wang, S. H. Hawley, G. E. Brueckner, K. P. Dere, R. A. Howard, M. J. Koomen, C. M. Korendyke, D. J. Michels, S. E. Paswaters, D. G. Socker, O. C. St. Cyr, D. Wang, P. L. Lamy, A. Liebaria, R. Schwenn, G. M. Simnett, S. Plunkett, and D. A. Biesecker. Measurements of flow speeds in the corona between 2 and 30 R_{\odot} . *The Astrophysical Journal*, 484:472–478, 1997.
- [75] D. G. Sime, R. R. Fisher, and R. C. Altrock. Rotation characteristics of the Fe XIV (5303 Å) solar corona. *The Astrophysical Journal*, 336:454–467, 1989.
- [76] K. R. Sivaraman and M. H. Gokhale. Anchor depths of flux elements and depths of flux sources in relation to the two rotation profiles of the sun’s surface magnetic fields. *Solar Physics*, 221:209–223, 2004.
- [77] H. B. Snodgrass. Magnetic rotation of the solar photosphere. *Ap.J.*, 270:288–299, July 1983.
- [78] H. B. Snodgrass. Smokestacks and Balloonmen: A Magnetic Rotation Controversy. In K. L. Harvey, editor, *The Solar Cycle*, volume 27 of *Astronomical Society of the Pacific Conference Series*, pages 71–82, 1992.
- [79] H. B. Snodgrass, R. Howard, and L. Webster. Recalibration of Mount Wilson Doppler measurements (Research note). *Solar Physics*, 90:199–202, 1984.
- [80] H. B. Snodgrass and A. A. Smith. On the Use of Correlations to Determine the Motions and Properties of Mesoscale Magnetic Features in the Solar Photosphere. *The Astrophysical Journal*, 546:528–541, 2001.

- [81] H. B. Snodgrass and R. K. Ulrich. Rotation of Doppler features in the solar photosphere. *The Astrophysical Journal*, 351:309–316, 1990.
- [82] O. C. St. Cyr, J. T. Burkepile, A. J. Hundhausen, and A. R. Lecinski. A comparison of ground-based and spacecraft observations of coronal mass ejections from 1980-1989. *J. Geophys. Res.*, 104:12493–12506, June 1999.
- [83] O. C. St. Cyr, S. P. Plunkett, D. J. Michels, S. E. Paswaters, M. J. Koomen, G. M. Simnett, B. J. Thompson, J. B. Gurman, R. Schwenn, D. F. Webb, E. Hildner, and P. L. Lamy. Properties of coronal mass ejections: SOHO LASCO observations from January 1996 to June 1998. *Journal of Geophysical Research*, 105:18169–18186, 2000.
- [84] O. C. St Cyr, H. Xie, M. L. Mays, J. M. Davila, H. R. Gilbert, S. I. Jones, W. D. Pesnell, N. Gopalswamy, J. B. Gurman, S. Yashiro, J. Wuelser, R. A. Howard, B. J. Thompson, and W. T. Thompson. Recent STEREO Observations of Coronal Mass Ejections. *AGU Fall Meeting Abstracts*, page A1491, 2009.
- [85] R. F. Stellingwerf. Period determination using phase dispersion minimization. *The Astrophysical Journal*, 224:953–960, 1978.
- [86] G. Stenborg. *Interpretation and Analysis on Various Time Scales of Narrow-Band Coronal Observations Obtained with a New Coronagraph System*. PhD dissertation, Gottingen, 2000.
- [87] G. Stenborg, R. Schwenn, B. Inhester, and N. Srivastava. On the Rotation Rate of the Emission Solar Corona. In A. Wilson & et al., editor, *Magnetic Fields and Solar Processes*, volume 448 of *ESA Special Publication*, pages 1107–1113, 1999.
- [88] E. C. Stone. Voyager 1 explores the termination shock region and the heliosheath beyond. *Science*, 309(5743):2017–2020, 2005.
- [89] J. Sykora. The large-scale behaviour of the green emission corona FeXIV 530.3 NM over the last 4.5 solar activity cycles. *Advances in Space Research*, 14:73, 1994.
- [90] S. J. Tappin, G. M. Simnett, and M. A. Lyons. A determination of outflow speeds in the lower solar wind. *Astronomy and Astrophysics*, 350:302–309, 1999.
- [91] W. T. Thompson. Coordinate systems for solar image data. *Astronomy and Astrophysics*, 449:791–803, 2006.
- [92] W. T. Thompson, J. M. Davila, R. R. Fisher, L. E. Orwig, J. E. Mentzell, S. E. Hetherington, R. J. Derro, R. E. Federline, D. C. Clark, P. T. C. Chen, J. L. Tveekrem, A. J. Martino, J. Novello, R. P. Wesenberg, O. C. St. Cyr,

- N. L. Reginald, R. A. Howard, K. I. Mehalick, M. J. Hersh, M. D. Newman, D. L. Thomas, G. L. Card, and D. F. Elmore. COR1 inner coronagraph for STEREO-SECCHI. In S. L. Keil and S. V. Avakyan, editors, *Innovative Telescopes and Instrumentation for Solar Astrophysics. Edited by Stephen L. Keil, Sergey V. Avakyan . Proceedings of the SPIE, Volume 4853, pp. 1-11 (2003).*, volume 4853 of *Presented at the Society of Photo-Optical Instrumentation Engineers (SPIE) Conference*, pages 1–11, 2003.
- [93] W. T. Thompson and N. L. Reginald. The Radiometric and Pointing Calibration of SECCHI COR1 on STEREO. *Solar Physics*, 250:443–454, 2008.
- [94] W. T. Thompson, K. Wei, J. T. Burkepile, J. M. Davila, and O. C. St. Cyr. Background Subtraction for the SECCHI/COR1 Telescope Aboard STEREO. *Solar Physics*, 262:213–231, 2010.
- [95] C. Torrence and G. P. Compo. A Practical Guide to Wavelet Analysis. *Bulletin of the American Meteorological Society*, 79:61–78, 1998.
- [96] R. K. Ulrich, J. E. Boyden, L. Webster, S. P. Padilla, and H. B. Snodgrass. Solar rotation measurements at Mount Wilson. V - Reanalysis of 21 years of data. *Solar Physics*, 117:291–328, 1988.
- [97] J. E. Vernazza, E. H. Avrett, and R. Loeser. Structure of the solar chromosphere. III - Models of the EUV brightness components of the quiet-sun. *Astrophys. J. Suppl. Ser.*, 45:635–725, April 1981.
- [98] Y.-M. Wang and N. R. Sheeley, Jr. The rotation of photospheric magnetic fields: A random walk transport model. *The Astrophysical Journal*, 430:399–412, 1994.
- [99] Y.-M. Wang and N. R. Sheeley, Jr. Sources of the solar wind at ulysses during 1990-2006. *The Astrophysical Journal*, 653:708–718, 2006.
- [100] Y.-M. Wang, N. R. Sheeley, Jr., R. A. Howard, and O. C. St. Cyr. Coronagraph observations of inflows during high solar activity. *Geophysical Research Letters*, 26(9):1203–1206, 1999.
- [101] Y.-M. Wang, N. R. Sheeley, Jr., A. G. Nash, and L. R. Shampine. The quasi-rigid rotation of coronal magnetic fields. *Astrophysical Journal*, 327:427–450, 1988.
- [102] Y.-M. Wang, N. R. Sheeley, Jr., D. G. Socker, R. A. Howard, and N. B. Rich. The dynamical nature of coronal streamers. *Journal of Geophysical Research*, 2000.
- [103] Y.-M. Wang, N. R. Sheeley, Jr., J. H. Walters, G. E. Brueckner, R. A. Howard, D. J. Michels, P. L. Lamy, R. Schwenn, and G. M. Simnett. Origin of streamer material in the outer corona. *The Astrophysical Journal*, 498:L165–L168, 1998.

- [104] F. Ward. Determination of the Solar-Rotation Rate from the Motion of Identifiable Features. *The Astrophysical Journal*, 145:416, 1966.
- [105] M. A. Weber, L. W. Acton, D. Alexander, S. Kubo, and H. Hara. A Method for Characterizing Rotation Rates in the Soft X-Ray Corona. *Solar Physics*, 189:271–288, 1999.
- [106] S. T. Wu, A. H. Wang, S. P. Plukett, and D. J. Michels. Evolution of global-scale coronal magnetic field due to magnetic reconnection: The formation of the observed blob motion in the coronal streamer belt. *The Astrophysical Journal*, 545:1101–1115, 2000.